SINGLE π^+ ELECTROPRODUCTION IN THE FIRST AND SECOND RESONANCE REGIONS USING CLAS

A Dissertation

Presented to

The Faculty of the Department of Physics

The College of William and Mary in Virginia

In Partial Fulfillment

Of the Requirements for the Degree of

Doctor of Philosophy

by

Hovanes Egiyan

2001

APPROVAL SHEET

This dissertation is submitted in partial fulfillment of
the requirements for the degree of

Doctor of Philosophy

Hovanes Egiyan

Approved, September 2001

Keith A. Griffioen, Advisor

Volker D. Burkert, Co-advisor
Jefferson Lab

J. Dirk Walecka

David S. Armstrong

Stepan Stepanyan
Old Dominion University

This work is dedicated to my parents, my relatives and my friends.

CONTENTS

ACKNOWLEDGMENTS

I thank my advisor Keith Griffioen for his constant leadership, encouragement and support throughout my graduate school years. I also would like to extend my gratitude to my co-advisor Volker Burkert for his guidance during my research at Jefferson Lab. Stepan Stepanyan, my colleague and friend, provided invaluable help in nearly every project I worked on. And I am very thankful to the other members of my thesis committee, Dirk Walecka and David Armstrong, for attending my annual reviews every fall, making important comments and suggestions, and for patiently reading my manuscript. Also I would like to thank Cole Smith, Will Brooks, Inna Aznaurian and Latifa Elouadrhiri for very helpful discussions which greatly facilitated my analysis work. Thanks to the Hall-B postdocs and graduate students - Burin, David, Costy, John, Kyungseon, Richard, Rob, Sasha, Si, Simon, Steve and many others - for their hard work during the commissioning and calibration period of the CLAS detector. And this work would have been impossible without the dedicated efforts by the Hall-B leadership and staff in building, maintaining and running such a sophisticated detector as CLAS.

Thanks to the entire Armenian community of Newport News for making me feel more like home during my graduate studies in Virginia. And these long years would have been very boring without my friends from W&M and Jefferson Lab - Agus, Carlos, Fefo, Gagik, Jordi, Marat, Paolo, Pibero and others - who's friendship is invaluable to me.

LIST OF TABLES

LIST OF FIGURES

ABSTRACT

The study of single pion electroproduction can provide valuable information on the structure of the nucleon and its excited states. Although these reactions have been studied for decades, never has the $n\pi^+$ channel been measured over the complete phase space of the reaction. The CEBAF Large Acceptance Spectrometer (CLAS) located in Hall B of Jefferson Lab is well-suited for conducting these measurements. The CLAS data were taken using a 1.515 GeV electron beam incident on a liquid H_2 target. The cross sections have been extracted, and their ϕ-dependence has been fit to obtain the σ_{TT}, σ_{TL} and the $\sigma_T + \epsilon\sigma_L$ linear combination of the structure functions. An analysis program based on the Mainz unitary isobar model was used to analyze the experimental data from the π^+ channel only. The resonant amplitudes for $P_{33}(1232)$, $S_{11}(1535)$ and $D_{13}(1520)$ were obtained from the fit.

SINGLE π^+ ELECTROPRODUCTION IN THE FIRST AND SECOND RESONANCE REGIONS USING CLAS

CHAPTER 1

Introduction

The structure of the nucleon and its excited states has been one of the most extensively investigated subjects in nuclear and particle physics for many years, because it allows us to understand important aspects of the underlying theory of the strong interactions. Many different reactions can be used to study the properties of the nucleon and its excited states. One can study the ground state nucleon using elastic scattering of electrons off protons and neutrons in order to obtain the electric and magnetic charge distributions. However, one can study the excited states only via the transitions from the ground states into the nucleon resonances, because lifetimes of the excited states are too short to make a target of excited nucleons technically feasible. The inclusive electron scattering spectrum clearly indicates four resonance regions above the elastic peak, but it does not allow us to separate different resonances which make up the second and higher resonance peaks. Even in the first resonant region there is a considerable non-resonant background under the dominant $\Delta(1232)$ peak. Therefore, exclusive measurements with a large angular coverage in the hadronic center of mass are necessary to separate the background from contributions from different overlapping resonances. A fit of the angular distributions will allow us to determine relative strengths for different resonances.

The excited states of the nucleon are unstable, rapidly decaying into meson-nucleon states. Due to the small mass of the pion, the single pion-nucleon decay is the favorite channel for many resonances, and not surprisingly, single pion electroproduction is being extensively exploited to understand the structure of nucleon.

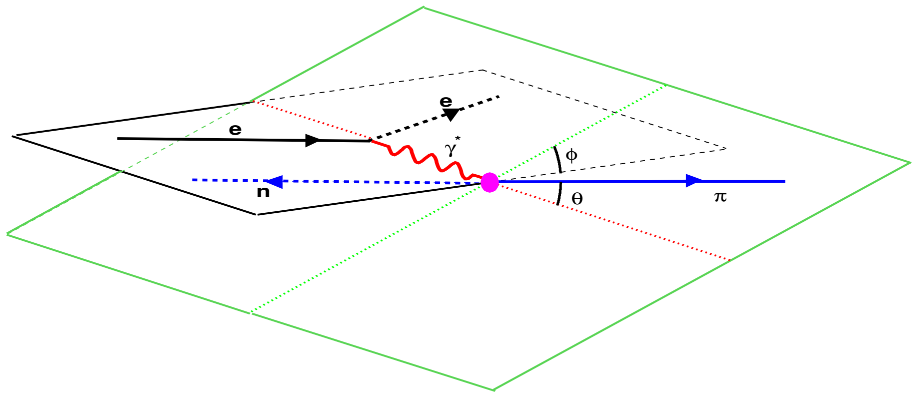

Figure 1.1: Kinematics of single π^+ electroproduction. Both θ and ϕ angles are defined in the rest frame of the final hadronic system with the z-axis pointing in the direction of the virtual photon 3-momentum.

In this experiment we study the transition amplitudes from protons into the higher mass resonances by observing the $n\pi^+$ final state. This experiment was performed at the Thomas Jefferson National Accelerator Facility in the spring of 1999. These data will provide us with valuable information to better understand the structure of the $\Delta(1232)$ resonance, usually studied in $p\pi^0$ channel, and more importantly for the three dominant isospin $I = 1/2$ resonances in the second resonance region, for which the $n\pi^+$ decay is preferred over the $p\pi^0$ channel.

In this chapter, the physics motivation for the experiment is presented, along with a review of the existing experimental data. Chapter 2 describes the CEBAF Large Acceptance Spectrometer (CLAS) used to make these measurements. Chapter 3 contains the details of the charged particle identification calibrations for CLAS, while Chapter 4 presents the analysis procedure of the experiment. The results of the measurements are discussed in Chapter 5.

1.1 Formalism

A process of electron scattering from a nucleon target which produces an outgoing nucleon and one pion is called a single pion electroproduction. The kinematic diagram of the single π^+ electroproduction is shown in Fig. 1.1. The virtual photon from the electron scattering can be characterized by two Lorentz invariants: Q^2, the four-momentum transfer squared, and ν:

$$\begin{aligned} Q^2 &\equiv -(k_i - k_f)^2 = 4E_iE_f \sin^2\frac{\theta_e}{2} \\ \nu &\equiv \frac{p_i \cdot p_\gamma}{M} = E_i - E_f, \end{aligned} \tag{1.1}$$

where k_i and k_f are the initial and final four momenta of the scattered electron, p_γ and p_i are the virtual photon and the target four momenta. E_i and E_f are the initial and final electron energies in the laboratory frame, θ_e is the electron scattering angle, and M is the proton mass. Very often the quantity ν is replaced by the invariant mass W of the virtual photon plus target:

$$W^2 \equiv (p_\gamma + p_i)^2 = M^2 + 2M\nu - Q^2. \tag{1.2}$$

In this thesis the set (Q^2, W) will be used to describe the virtual photon. The $ep \rightarrow e\pi^+X$ missing mass M_X is defined as:

$$M_X^2 \equiv ((k_i + p_i) - (k_f + q_\pi))^2, \tag{1.3}$$

where q_π is the four momentum of the detected π^+. For single π^+ production there is a constraint on the missing mass $M_X = M_n$. The two angles of the pion in the center of mass frame of the hadronic system are defined in Fig. 1.1 . The angle between the virtual photon three-momentum direction and the direction of the pion is denoted as θ. The ϕ angle is defined so that the electron scattering plane lies in the $\phi = 0$ half-plane with the z-axis pointing along the virtual photon momentum. The set of five variables (ϕ_e, Q^2, W, θ, ϕ) completely determines the kinematics of single pion electroproduction. In fact, the knowledge of only four of these quantities in our case is already adequate, because the cross section does not depend on the ϕ_e azimuthal angle of the electron in the laboratory frame in the absence of any transverse polarization of the target or the beam.

The unpolarized cross sections of the single π^+ electroproduction in one photon exchange approximation can be written [1] as:

$$\begin{aligned}
\frac{\partial^5\sigma}{\partial E_f \partial\Omega_e \partial\Omega^*_\pi} &= \Gamma \cdot \frac{d\sigma}{d\Omega^*_\pi}, \\
\Gamma &= \frac{\alpha}{2\pi^2 Q^2} \frac{(W^2 - M^2)E_f}{ME_i} \frac{1}{1-\epsilon}, \\
\epsilon &= \left[1 + 2\left(1 + \frac{\nu^2}{Q^2}\right)\tan^2\frac{\theta_e}{2}\right]^{-1}, \\
\frac{d\sigma}{d\Omega^*_\pi} &= \sigma_T + \epsilon\sigma_L + \epsilon\sigma_{TT}\cos 2\phi + \sqrt{2\epsilon(1+\epsilon)}\sigma_{TL}\cos\phi, \qquad (1.4)
\end{aligned}$$

where ϵ is the virtual photon polarization parameter, Γ is the virtual photon flux, and $\frac{d\sigma}{d\Omega^*_\pi}$ is the photoabsorption cross section. The σ_T, σ_L, σ_{TT} and σ_{TL} are the structure functions[1], that depend on Q^2, W and θ. σ_T is the photoabsorption cross section of the unpolarized transverse virtual photons, while σ_L is the cross section for unpolarized longitudinal photons. The σ_{TT} term arises due to the interference between the two transverse linear photon polarizations, while σ_{TL} is due to the interference between transverse and longitudinal polarizations of the virtual photons. These structure functions can be written in terms of six helicity amplitudes [2] as:

$$\begin{aligned}
\sigma_T &= \frac{1}{2}F(|H_1|^2 + |H_2|^2 + |H_3|^2 + |H_4|^2) \\
\sigma_L &= F(|H_5|^2 + |H_6|^2) \\
\sigma_{TT} &= F Re(H_3 H_2^* - H_4 H_1^*) \\
\sigma_{TL} &= \frac{1}{\sqrt{2}} F Re[H_5^*(H_4 - H_1) - H_6^*(H_3 + H_2)] \\
F &= \frac{2W|\vec{q}^{\,*}_\pi|}{W^2 - M^2}, \qquad (1.5)
\end{aligned}$$

where $\vec{q}^{\,*}_\pi$ is the pion momentum in the hadronic center of mass frame, and the H_i are the six helicity amplitudes describing the transitions between eigenstates of the

[1] In some literature instead of σ_T, σ_L, σ_{TT} and σ_{TL} more proper notation is used for the structure functions, like $\frac{d\sigma_T}{d\Omega_\pi}$, $\frac{d\sigma_L}{d\Omega_\pi}$, $\frac{d\sigma_{TT}}{d\Omega_\pi}$ and $\frac{d\sigma_{TL}}{d\Omega_\pi}$. This notation is more accurate since it emphasizes that there is no integration over angles implied, as in the case with structure functions for inclusive electron scattering or the GDH sum rules.

helicities of the nucleon and photon [3]. The helicity amplitudes can be decomposed in terms of partial wave helicity amplitudes [4]:

$$
\begin{aligned}
H_1 &= \frac{1}{2}\sqrt{2}\sin\theta\cos\frac{\theta}{2}\sum_{l=1}^{\infty}(B_{l+}-B_{l+1,-})(P_l''-P_{l+1}'') \\
H_2 &= \sqrt{2}\cos\frac{\theta}{2}\sum_{l=0}^{\infty}(A_{l+}-A_{l+1,-})(P_l'-P_{l+1}') \\
H_3 &= \frac{1}{2}\sqrt{2}\sin\theta\sin\frac{\theta}{2}\sum_{l=1}^{\infty}(B_{l+}+B_{l+1,-})(P_l''+P_{l+1}'') \\
H_4 &= \sqrt{2}\sin\frac{\theta}{2}\sum_{l=0}^{\infty}(A_{l+}+A_{l+1,-})(P_l'+P_{l+1}') \\
H_5 &= \sqrt{2}\cos\frac{\theta}{2}\sum_{l=0}^{\infty}(C_{l+}-C_{l+1,-})(P_l'-P_{l+1}') \\
H_6 &= \sqrt{2}\sin\frac{\theta}{2}\sum_{l=0}^{\infty}(C_{l+}+C_{l+1,-})(P_l'+P_{l+1}'),
\end{aligned}
\tag{1.6}
$$

where θ is the center of mass angle and P_l are Legendre polynomials, which are functions of $\cos\theta$. $A_{l\pm}$ describe the transitions with transverse photons with total helicity of the γN system $h=\pm\frac{1}{2}$, $B_{l\pm}$ describe transitions with total helicity $h=\pm\frac{3}{2}$, while the Coulomb-type transitions with $h=\pm\frac{1}{2}$ are described by $C_{l\pm}$ helicity elements[2]. The partial wave helicity amplitudes can be related to the helicity photocoupling amplitudes for individual resonances with total angular momentum j and mass W_R by [4]:

$$
\begin{aligned}
A_{l\pm} &= \mp C^I_{\pi N} f A_{1/2} \\
B_{l\pm} &= \pm C^I_{\pi N} f\sqrt{\frac{16}{(2j-1)(2j+3)}}A_{3/2} \\
C_{l\pm} &= \mp C^I_{\pi N} f\sqrt{\frac{Q^2}{\vec{Q}^{*2}}}S_{1/2} \\
f &= \sqrt{\frac{K_W M\Gamma_\pi}{(2j+1)\pi\mid\vec{q}_\pi\mid W_R\Gamma^2}} \\
K_W &= \frac{W^2-M^2}{2W},
\end{aligned}
\tag{1.7}
$$

[2]The signs of the helicities and the signs in the $A_{l\pm}$, $B_{l\pm}$, $C_{l\pm}$ are not correlated.

where $C^I_{\pi N}$ are the isospin coefficients [1], $\vec{Q}^*$ and $\vec{q}_\pi$ are the photon and pion momenta in the center of mass frame.

In the literature a different set of amplitudes is also used, according to the following decomposition of the current operator for the transition between the initial and the final states [5] :

$$\begin{aligned} \mathbf{J} &= \frac{4\pi W}{M}\Big(i\tilde{\boldsymbol{\sigma}}F_1 + (\boldsymbol{\sigma}\cdot\hat{\boldsymbol{k}})[\boldsymbol{\sigma}\times\hat{\boldsymbol{q}}]F_2 + i\tilde{\boldsymbol{k}}(\boldsymbol{\sigma}\cdot\hat{\boldsymbol{q}})F_3 \\ &+ i\tilde{\boldsymbol{k}}(\boldsymbol{\sigma}\cdot\hat{\boldsymbol{k}})F_4 + i\hat{\boldsymbol{q}}(\boldsymbol{\sigma}\cdot\hat{\boldsymbol{q}})F_5 + i\hat{\boldsymbol{q}}(\boldsymbol{\sigma}\cdot\hat{\boldsymbol{k}})F_6\Big) \qquad (1.8) \\ \rho &= \frac{4\pi W}{M}\Big(i(\boldsymbol{\sigma}\cdot\hat{\boldsymbol{k}})F_7 + i(\boldsymbol{\sigma}\cdot\hat{\boldsymbol{q}})F_8\Big), \qquad (1.9) \end{aligned}$$

where $\hat{\mathbf{k}}$ and $\hat{\mathbf{q}}$ are the unit vectors in the direction of the pion and photon momenta in the center-of-mass frame, respectively, σ is the spin operator, and $\tilde{\mathbf{v}} \equiv \mathbf{v} - (\mathbf{v}\cdot\hat{\mathbf{q}})\hat{\mathbf{q}}$ is defined for any vector $\mathbf{v}$. The F_1, F_2, F_3 and F_4 amplitudes describe the transverse current, while the longitudinal component is given by F_5 and F_6. The other two amplitudes can be expressed in terms of the first six due to the current conservation. The F_i amplitudes can be decomposed in terms of the multipole amplitudes [5] :

$$\begin{aligned} F_1 &= \sum_{l=0}^{\infty}\{(lM_{l+} + E_{l+})P'_{l+1} + [(l+1)M_{l-} + E_{l-}]P'_{l-1}\} \\ F_2 &= \sum_{l=1}^{\infty}[(l+1)M_{l+} + lM_{l-}]P'_l \\ F_3 &= \sum_{l=1}^{\infty}[(E_{l+} - M_{l+})P''_{l+1} + (E_{l-} + M_{l-})P''_{l-1}] \\ F_4 &= \sum_{l=2}^{\infty}(M_{l+} - E_{l+} - M_{l-} - E_{l-})P''_l \\ F_5 &= \sum_{l=0}^{\infty}[(l+1)S_{l+}P'_{l+1} - lS_{l-}P'_{l-1}] \\ F_6 &= \sum_{l=1}^{\infty}[lS_{l-} - (l+1)S_{l+}]P'_l. \qquad (1.10) \end{aligned}$$

The Legendre polynomials are functions of $\cos\theta$ and the $E_{l\pm}$, $M_{l\pm}$ and $S_{l\pm}$ multipole amplitudes depend on Q^2 and W only. The connection between the helicity amplitudes and the F_i amplitudes is given by [2] :

$$\begin{aligned}
H_1 &= -\cos\frac{\theta}{2}\sin\theta(F_3+F_4)/\sqrt{2} \\
H_2 &= -\sqrt{2}\cos\frac{\theta}{2}\left[F_1-F_2-\sin^2\frac{\theta}{2}(F_3-F_4)\right] \\
H_3 &= \sin\frac{\theta}{2}\sin\theta(F_3-F_4)/\sqrt{2} \\
H_4 &= \sqrt{2}\sin\frac{\theta}{2}\left[F_1+F_2+\cos^2\frac{\theta}{2}(F_3+F_4)\right] \\
H_5 &= -\sqrt{\frac{Q^2}{\vec{Q}^{*2}}}\cos\frac{\theta}{2}(F_5+F_6) \\
H_6 &= \sqrt{\frac{Q^2}{\vec{Q}^{*2}}}\sin\frac{\theta}{2}(F_5-F_6),
\end{aligned} \tag{1.11}$$

where $\vec{Q}^*$ is the photon 3-momentum in the hadronic center of mass frame, and θ is the pion angle in that frame. Then the partial wave helicity amplitudes in Eqs. (1.6) and the multipoles from Eqs. (1.10) are related through the following expressions [4]:

$$\begin{aligned}
M_{l+} &= \frac{1}{2(l+1)}(2A_{l+}-(l+2)B_{l+}) \\
E_{l+} &= \frac{1}{2(l+1)}(2A_{l+}+lB_{l+}) \\
M_{l+1,-} &= \frac{1}{2(l+1)}(2A_{l+1,-}+lB_{l+1,-}) \\
E_{l+1,-} &= \frac{1}{2(l+1)}(-2A_{l+1,-}+(l+2)B_{l+1,-}) \\
S_{l+} &= \frac{\sqrt{2}}{l+1}\sqrt{\frac{\vec{Q}^{*2}}{Q^2}}C_{l+} \\
S_{l+1,-} &= -\frac{\sqrt{2}}{l+1}\sqrt{\frac{\vec{Q}^{*2}}{Q^2}}C_{l+1,-}.
\end{aligned} \tag{1.12}$$

For photo- and electroproduction processes the photon is assigned either isospin $I_\gamma=0$ or $I_\gamma=1$. Then the total isospin of the photon-nucleon system is either $I=1/2$ for an isoscalar photon or $I=1/2$ or $I=3/2$ for an isovector photon. However, the experimentally observed state of a nucleon and a pion is not an eigenstate of the isospin operator, and the amplitudes for a πN final state should be expressed in terms of definite isospin amplitudes [5]:

$$\begin{aligned}
A(\gamma^* + p \to p + \pi^0) &= A_p^{(1/2)} + \frac{2}{3}A^{(3/2)} \\
A(\gamma^* + n \to n + \pi^0) &= -A_n^{(1/2)} + \frac{2}{3}A^{(3/2)} \\
A(\gamma^* + p \to n + \pi^+) &= \sqrt{2}[A_p^{(1/2)} - \frac{1}{3}A^{(3/2)}] \\
A(\gamma^* + n \to p + \pi^-) &= \sqrt{2}[A_n^{(1/2)} + \frac{1}{3}A^{(3/2)}] \\
A_p^{(1/2)} &= A^{(0)} + \frac{1}{3}A^{(1/2)} \\
A_n^{(1/2)} &= A^{(0)} - \frac{1}{3}A^{(1/2)}, \qquad (1.13)
\end{aligned}$$

where $A^{(3/2)}$ is the amplitude for the total isospin $I = 3/2$, while $A_p^{(1/2)}$ and $A_n^{(1/2)}$ are the proton and neutron isospin amplitudes. The last two are linear combinations of two different $I = 1/2$ isospin amplitudes arising due to the fact that the photon has isoscalar and isovector components. In order to isolate the $I = 1/2$ isospin amplitude for the proton one needs to measure both $p\pi^0$ and $n\pi^+$ production channels.

1.2 Motivation

The underlying theory of the strong interaction is believed to be Quantum Chromodynamics (QCD). But unlike the theory of the electroweak interactions, it does not allow for perturbative solutions at the distances comparable with the size of the nucleon. The theoretical tools for calculating the properties of the nucleon and its excited states are limited to numerical calculations using Lattice QCD and effective theories which use degrees of freedom different from the current quarks and gluons, but which still have the fundamental symmetries of QCD. Although effective theories can not be considered as fundamental, they are extremely useful in explaining the properties of the bound states, which are expected from QCD. An obvious way to test these theories is to compare their predictions of the properties of the baryons with experimentally observable quantities. These include the masses and the widths of the excited states, the nucleon form factors, and the transition amplitudes from the ground state into nucleon resonances. Although elastic scattering experiments allow us to determine the electric and magnetic charge distributions of the ground state, the study of transitions from the nucleon to higher mass resonances can provide more detailed information on the structure of the nucleon and its excited states.

The main advantage of studying nucleon structure in electroproduction is that the electromagnetic vertex is well described by Quantum Electrodynamics (QED). Therefore, the contribution of the strong interaction is the only unknown in these processes. For pion electroproduction at low Q^2, perturbative QCD (pQCD) is not applicable; therefore, models have to be used to understand pion electroproduction processes and to extract the transition form-factors. There are many different models for describing the electroexcitation of resonances via pion production which can be classified as:

- Quark models
- Models based on the Effective-Lagrangian approach
- Isobar models
- Dynamical models
- Models based on dispersion relations.

The basic feature of QCD-inspired quark models [6, 73, 77, 34, 76] is that baryons are made up of three constituent quarks, each having approximately one third of the total baryon mass. The motion of these quarks is described by introducing an effective Hamiltonian, which has main QCD features such as confinement and single gluon exchange terms. Different levels of excitation in this system correspond to different resonances. The first such model, the Constituent Quark Model (CQM) [6], was already very successful in describing the masses of the low lying baryon states with the radial excitation numbers $N = 0$ and $N = 1$. Quark models describe the excitation of nucleon resonances as a transition from the ground state to an excited state. However, the amplitudes for these processes correspond only to the "undressed" excitation vertex. Resonances can also be excited in the meson-nucleon system as a result of the final-state interactions. One would like to have a model to describe the Q^2 dependence of the "bare" transition form-factor, combined with a model describing the interactions in the pion-nucleon system. The full resonant amplitudes, including the direct photoexcitation process and the meson-nucleon resonant rescattering, should be compared with other models and with the experimental data.

One of the widely used methods for analysis of resonance electroproduction data is the Effective-Lagrangian approach [17]. One builds the total interaction Lagrangian as a sum of a set of Lagrangians describing different types of interactions:

$$L_{tot} = L_{\gamma NN^*} + L_{\pi NN^*} + L_{\gamma NN} + L_{\gamma\pi\pi} + L_{VNN} + L_{V\gamma\pi}, \tag{1.14}$$

where $L_{\gamma NN^*}$ and $L_{\pi NN^*}$ terms describe the s-channel resonance production vertex, plus the u-channel N^* exchange. The other terms describe t-channel pion and vector meson exchanges, as well as the nucleon-pole Feynman diagrams. Only trivial tree-level diagrams are used in the calculations of the transition amplitudes. However, some of these models use unitarization procedures [16] to account for higher order Feynman diagrams.

The isobar models describe pion electroproduction in the resonance region by calculating the total amplitude as a coherent sum of many nucleon resonance production diagrams and a non-resonant background. One of the first such models was developed by R.L. Walker [11] to analyze pion photoproduction data. This model assumed a Breit-Wigner form for the resonant amplitudes and included nucleon pole and pion exchange diagrams as a background. Later a similar model was used to analyze electroproduction data [12]. In addition to the Born terms, this model used a background parameterization with a correct $|\vec{q}_\pi|^l$ threshold behavior and with a dipole-like form factor falloff with pion momentum squared $\vec{q}_\pi^{\,2}$. One of the best isobar models, successfully describing charged and neutral pion electroproduction data, is the Unitary Isobar Model (UIM)[3] , developed at University of Mainz [71]. It uses effective Lagrangian methods to calculate the Born background, including ω and ρ meson exchange process. The background amplitudes are unitarized with a $(1 + i f_{l\pm}^{\pi N})$ factor, where $f_{l\pm}^{\pi N}$ are the pion-nucleon scattering amplitudes. Another possibility of including the πN final-state interactions is to use a dynamical model in combination with Breit-Wigner parameterization of resonant amplitudes [10].

The common feature of the dynamical models is that they are trying to account for pion-nucleon scattering effects explicitly. In one of the first dynamical models [13] the authors, using the optical theorem, modeled the electroproduction amplitudes using the form:

$$\begin{aligned} a(W,Q^2) &\cong \frac{-\frac{1}{2}(\Gamma_{\gamma^*}\Gamma_\pi)^{1/2}}{W - W_R + \frac{1}{2}i\Gamma} \\ \frac{1}{2}\Gamma_{\gamma^*} &= \frac{[a^{BA}(W_R,Q^2)]^2}{q_R N(W_R)[-Re' D(W_R)]} \\ \frac{1}{2}\Gamma_\pi &= \frac{N(W_R)}{-Re' D(W_R)} q_R \\ \frac{1}{2}\Gamma &= \frac{N(W_R)}{-Re' D(W_R)} q_R \frac{\sigma_{tot}(W_R)}{\sigma_{el}(W_R)}, \end{aligned} \tag{1.15}$$

where q_R is the pion momentum at the resonance position in the center of mass frame; $\sigma_{tot}(W_R)$ is the total pion-nucleon scattering cross cross section at the resonance position; $\sigma_{el}(W_R)$ is the elastic pion-nucleon cross section; Γ, Γ_{γ^*} and Γ_π

[3] In this thesis we also will refer to the Mainz model as MAID.

are the full, electromagnetic and pion decay widths, respectively; $a^{BA}(W_R, Q^2)$ is the amplitude corresponding to a gauge invariant set of exchange graphs that are believed to play an important role in the excitation mechanism. This set includes nucleon pole diagrams as well as pion and ω vector meson exchange terms. Later models have more elaborate schemes to describe the background processes. A recent model by Sato and Lee [72] obtains an effective Hamiltonian from the interaction Lagrangian using the method of unitary transformations. The original interaction Lagrangian L_I includes:

$$\begin{aligned} L_I = L_{\gamma NN} + L_{\gamma\pi\pi} + L_{\gamma\pi NN} + L\gamma\rho\pi + L_{\gamma\omega\pi} + L_{\gamma N\Delta} \\ +L_{\pi NN} + L_{\pi N\Delta} + L_{\rho NN} + L_{\rho\pi\pi}. \end{aligned} \tag{1.16}$$

This particular model includes only the $P_{33}(1232)$ resonance, and therefore, does not describe the experimental cross section above the first resonance region.

Based on the very general principle of causality one can write dispersion relations for the electroproduction amplitudes, relating the real and imaginary parts of the amplitude [1]:

$$\begin{aligned} ReH_i &= R_i\left(\frac{1}{M^2-s}+\frac{\eta_i}{M^2-u}\right) \\ &+ \frac{P}{\pi}\int\limits_{s_0}^{\infty} ImH_i(s')\left(\frac{1}{s'-s}+\frac{\eta_i}{s'-u}\right)ds', \end{aligned} \tag{1.17}$$

where s and u are the Mandelstam invariants, η_i are the crossing symmetry factors. The imaginary parts of the amplitudes are saturated with the resonance contributions, while the R_i terms are the residues from the Born terms. This method has been successfully used in many analyses of pion electroproduction [14].

Despite these large theoretical efforts, resulting in numerous models for pion electroproduction, currently there is not a framework allowing for an extraction of the resonant parameters at the γNN^* vertex in a model-independent way. In this

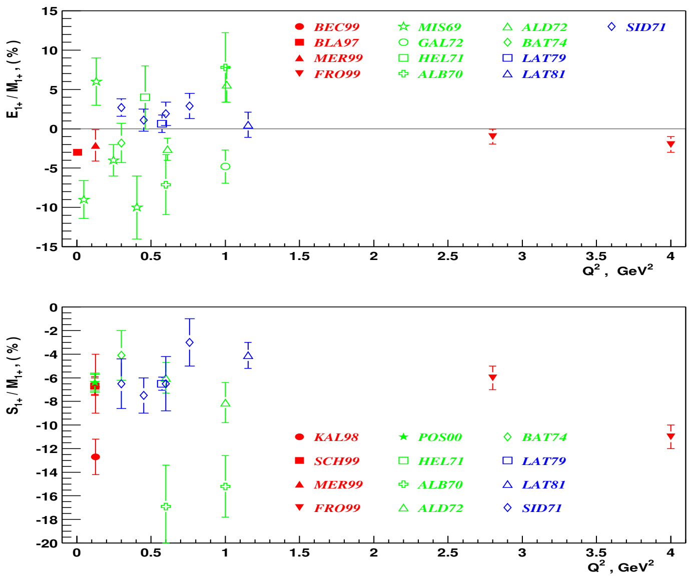

Figure 1.2: Existing experimental data on $\frac{E_{1+}}{M_{1+}}$ (top) and $\frac{S_{1+}}{M_{1+}}$ (bottom) ratios for $\Delta(1232)$. Almost all the data come from single π^0 production analyses: BEC99 [18], BLA97 [19], MER99 [20], FRO99 [21], POS00 [22], KAL98 [23], SCH99 [24], MIS69 [25], GAL72 [26], HEL71 [27], ALB70 [28], ALD71 [29], BAT74 [30], LAT79 [31], LAT81 [32], SID71 [33].

thesis the MAID unitary isobar model [71] is utilized as a physics analysis framework to obtain the physical quantities of interest.

The main purpose of this study is to improve significantly the data from which the structure and the properties of the nucleon resonances in the first and the second resonance regions are extracted. It is well known that the first resonant region is dominated by the $\Delta(1232)$ resonance. In this thesis an alternate notation for resonant states will also be used. Each resonance can be characterized by its isospin I, total angular momentum J, parity P, and mass M_R. Since most of the nucleon resonances have been observed in pion-nucleon scattering, the orbital angular momentum of the pion-nucleon system often is used instead of the parity. A resonance state with isospin I and angular momentum J, producing a pion-nucleon system with the orbital angular momentum L is denoted as $L_{(2I)(2J)}(M_R)$. In this notation $\Delta(1232)$ is $P_{33}(1232)$. The second resonance region is dominated by $P_{11}(1440)$,

$S_{11}(1535)$ and $D_{13}(1520)$ resonances.

For the $P_{33}(1232)$ resonance the quantities of greatest interest are the ratios of the electric and scalar quadrupole amplitudes to that of the magnetic dipole: $R_{EM} \equiv \frac{E_{1+}}{M_{1+}}$, $R_{SM} \equiv \frac{S_{1+}}{M_{1+}}$. The Constituent Quark Model (CQM), which is considered valid for large distances, predicts very small values for these ratios. In the static case, when no orbital excitations are allowed, the transition from nucleon to $\Delta(1232)$ state occurs when the virtual photon interacts with one of the constituent quarks and "flips" the spin of that quark. The resulting three quark state has a total spin of $S = \frac{3}{2}$ with no orbital excitation. From the momentum and parity conservation it follows that such a transition can be induced only by the M1 multipole. If the effects of single gluon exchange, such as color hyperfine interaction, are included in the model as perturbations, then the ground states obtain some admixture of $L = 2$ excited states of the unperturbed Hamiltonian. This leads to small contributions from electric and scalar quadrupoles to the $N\Delta$ transition amplitude.

On the other hand, at very small distances corresponding to large momentum transfers, using helicity conservation arguments, perturbative QCD predicts that the ratio R_{EM} should be equal to 1 [8]. Hence, a transition from $R_{EM} \approx 0$ to $R_{EM} = 1$ is expected at some intermediate values of the momentum transfer. The corresponding transition in terms of the transverse photon asymmetry $A_1 \equiv \frac{|A_{1/2}|^2 - |A_{3/2}|^2}{|A_{1/2}|^2 + |A_{3/2}|^2}$ is from $A_1 = -1/2$ at $Q^2 = 0$ to $A_1 = +1$ as $Q^2 \to \infty$. The value of Q^2 at which this transition occurs will help determine at which distances perturbative QCD begins to work. At this time this ratio has been measured up to $Q^2 = 4$ GeV^2 and it is still very close to zero [21]. The R_{SM} ratio is predicted by pQCD to be constant at very high Q^2 [8].

The existing data for R_{EM} and R_{SM} are shown in Fig. 1.2. Almost all experimental data on this plot are from the $p\pi^0$ channel; measurements of positively charged pion electroproduction will allow us to separate the $I = 3/2$ isospin com-

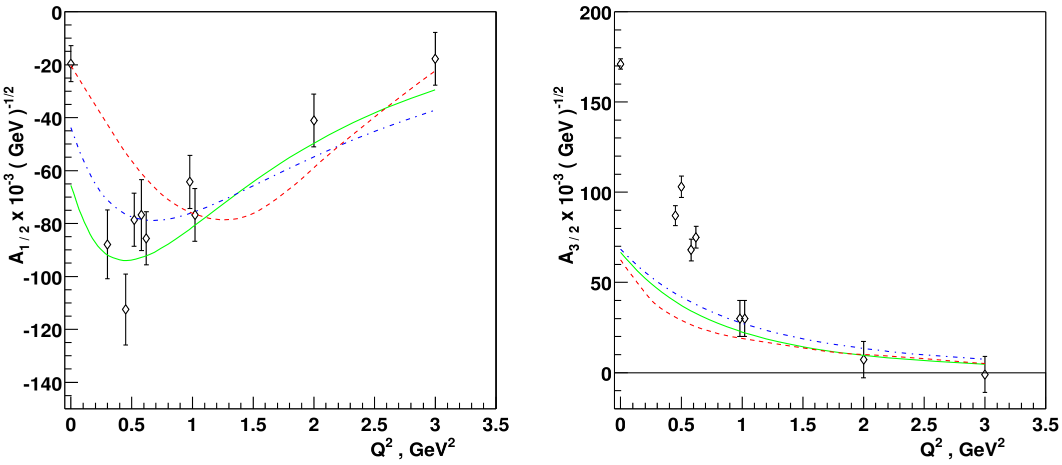

Figure 1.3: Existing data [4] on transverse photocoupling amplitudes of the proton for the $D_{13}(1520)$ resonance. Red dashed curves from [74], green solid curves from [80], dashed blue curves from [81].

ponent of the amplitude. The top plot in Fig. 1.2 shows that R_{EM} has not reached the asymptotic value of 1 at $Q^2 = 4$ GeV^2.

Similar to the $P_{33}(1232)$ resonance, the $D_{13}(1520)$ transverse photon asymmetry is expected to go through a transition from $A_1 = -1$ at $Q^2 = 0$ to $A_1 = +1$ at very high values of Q^2. It is well known that at $Q^2 = 0$ the photoproduction of $D_{13}(1520)$ is predominantly $A_{3/2}$ [1]. At higher values of Q^2 $A_{1/2}$ is predicted to become dominant by both quark models and pQCD [4]. The existing experimental data, unlike for the $\Delta(1232)$ resonance, support these predictions already at $Q^2 \approx 0.5$ GeV^2. A compilation of existing data [4] for the $A_{1/2}$ and $A_{3/2}$ amplitudes is shown in Fig. 1.3. The present experiment will allow us to investigate the behavior of these amplitudes near the Q^2 point where the photon transverse asymmetry A_1 crosses zero.

Another subject of debate is the structure of the $P_{11}(1440)$ “Roper” resonance. In the constituent quark model [6] it is identified as a radially-excited three quark state with the radial excitation number $N = 2$. But in order to get the mass consistent with the experimental value, a large perturbation is introduced, which

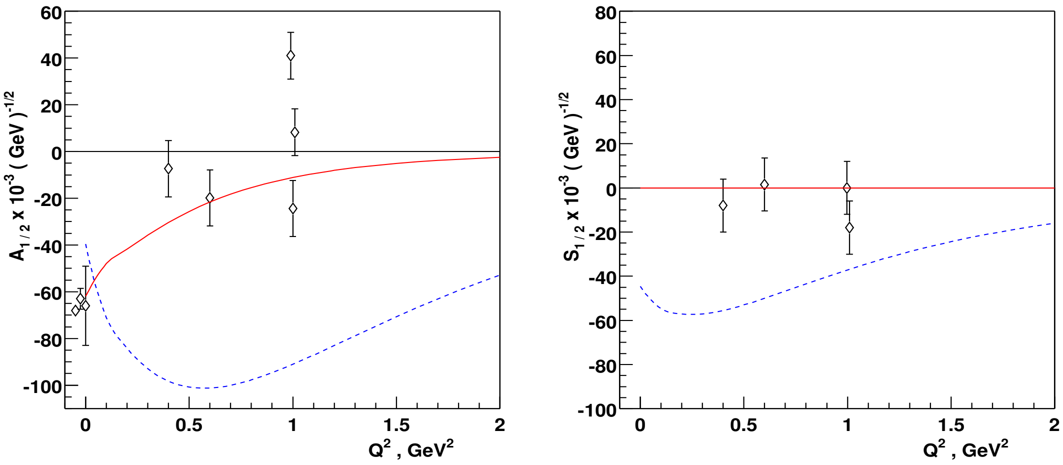

Figure 1.4: Existing data on the photocoupling amplitudes of the proton for the $P_{11}(1440)$ resonance. Data are from [37, 4, 38][5]. Red solid curve - hybrid model [9], blue dashed curve - three quark state [34].

makes the application of perturbation theory unjustified. On the other hand, QCD-inspired models predict the existence of so-called hybrid states, where in addition to the constituent quarks there is at least one constituent gluon. For instance, in the flux tube model [7] this kind of state can be created by exciting the flux tube between two quarks in a nucleon. One of the possible explanations of the Roper resonance is that it is actually a hybrid state. It would have the same quantum numbers, but the internal structure would be entirely different from the corresponding three quark state. It was shown [9] that the Q^2 dependence of the photocoupling amplitudes $A_{1/2}$ and $S_{1/2}$ is quite different depending on what kind of state $P_{11}(1440)$ is (see Fig. 1.4). The current experimental data do not allow us to distinguish between the two models for the Roper resonance. Because of the isospin ($I = \frac{1}{2}$, $I_z = \frac{1}{2}$) nature of the $P_{11}^{+}(1440)$ resonance, the $n\pi^+$ channel adds much sensitivity to the photocoupling amplitude. Nevertheless, the presence of the $\Delta(1232)$ resonance and the large width of the $P_{11}(1440)$ state may cause difficulty in extracting the amplitudes for Roper resonance excitation.

[5]The error bars for the electroproduction points were not estimated in the original analysis

The $S_{11}(1535)$ resonance is usually studied through η meson production. This is due to the large branching ratio to the ηN channel and to very little non-resonant background. The absence of any significant physical background is because of the proximity of the resonance mass to the η production threshold. On the other hand, the threshold effects complicate the amplitude extraction procedure. The $S_{11}(1535)$ resonance is known to decay via pion channels about 40% of the time [83]. The study of the electroexcitation of $S_{11}(1535)$ can provide an independent measurement of the $A_{1/2}$ and $S_{1/2}$ helicity amplitudes. It can also help to understand the threshold effects in the η electroproduction channel.

The main Feynman diagrams, representing the single π^+ production, are shown in Fig. 1.5. The process of our interest is one shown in Fig. 1.5 a, where the virtual photon excites a resonance state which then decays into a neutron and a π^+. The other diagrams, also called Born terms, are considered as background in this experiment, with the strongest contribution coming from the t-channel pion exchange process, Fig. 1.5 c. Note that this diagram is absent in the $p\pi^0$ channel due to charge-parity conservation at the $\gamma^*\pi\pi$ vertex. One of the main challenges of the physics analysis of this reaction is to calculate the background terms correctly and to obtain the resonant part of the amplitudes by fitting the angular distributions. Therefore, it is essential to have a large angular coverage in the center-of-mass frame. In order to cover 4π solid angle in the center-of-mass frame, it is necessary to have a nearly 4π coverage in the laboratory frame for the π^+ due to the fact that pions are much lighter than neutrons. Therefore, the main advantage of doing this experiment with CLAS is that it allows us to detect both the electron and the π^+ simultaneously, covering nearly the full phase space of the reaction.

---

paper by Gerhardt [38].

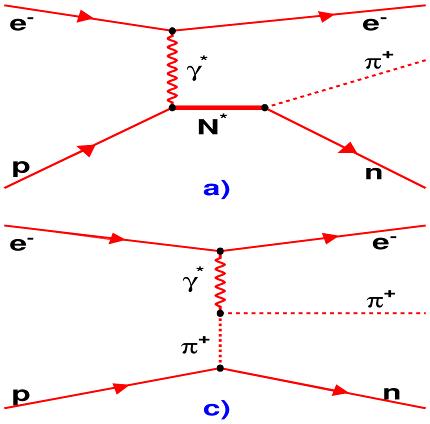

Figure 1.5: Some of the diagrams contributing into single π^+ electroproduction. a) s-channel resonance production; b) s-channel nucleon exchange; c) and d) t-channel pion and ρ-meson exchange diagrams.

1.3 Existing Experimental Data on Single π^+ Electroproduction

Most of the existing single pion electroproduction data on proton targets are from the neutral pion channel. All of the existing single π^+ electroproduction data have very limited coverage, while all of the analysis techniques require nearly full angular coverage in the center-of-mass frame.

One of the first experiments to study charged pion electroproduction in the resonance region was conducted at the Daresbury Nuclear Physics Laboratory in the early 1970s [46]. The detector consisted of two spectrometers with approximately 2 msr angular acceptance each. The Q^2 range was from 0.36 GeV^2 to 0.46 GeV^2, while the W range was 1.40 GeV $\leq W \leq$ 1.86 GeV and was correlated with Q^2. The angular coverage in the center-of-mass frame in θ was up to 75^o.

Another cross section measurement with forward angular coverage was conducted at Bonn University [47] at $Q^2 = 0.15$ GeV^2 and 0.3 GeV^2 in the first resonance region. This experiment used a two-arm detector as well, and the Q^2 values were correlated with W. The angular range in the center of mass of the hadronic system was up to $\theta = 40^0$, with 1.14 GeV $\leq W \leq$ 1.28 GeV. Note that the P-wave decay for the $\Delta(1232)$ resonance is largest at $\theta = 90^0$, and therefore, this experiment had little sensitivity to $\Delta(1232)$ resonance amplitudes due to the large background contributions in the charged pion production channel. A few years later the Bonn group conducted another experiment [48] to study the charged pion electroproduction in the second and third resonance regions using essentially the same detectors. Measurements were done in the forward $1 \geq \cos\theta \geq 0.97$ and backward $-1 \leq \cos\theta \leq -0.97$ regions at $Q^2 = 0.3$ GeV^2. The advantage of measuring in the backward direction is that the t-channel background is much smaller at large angles. Nevertheless, these data still had very little sensitivity to the resonance parameters due to the lack of angular coverage.

The main problem of the previously conducted experiments for the $n\pi^+$ channel is that two-arm detectors cannot provide an adequate angular coverage, if one wants to detect both the electron and the pion.[6] The CLAS detector provides us with a unique opportunity to measure single π^+ electroproduction cross sections for the first time, covering nearly the full angular range in the center-of-mass frame.

[6] It is possible to study $n\pi^+$ electroproduction using a two arm detector with the hadron arm detecting the neutron. Then one has to deal with the systematic uncertainties due to difficulties of detecting neutrons.

CHAPTER 2

Experimental Apparatus

2.1 Continuous Electron Beam Accelerator Facility

The experiment has been carried out using the electron beam provided by the Continuous Electron Beam Accelerator Facility (CEBAF) at the Jefferson Lab. This accelerator produces a continuous polarized electron beam which is delivered to the three end stations (Hall A, B, C) where the experimental detectors are housed. Figure 2.1 shows a schematic diagram of the machine. The two linear accelerators, based on superconducting RF cavities, provide approximately 1 GeV energy for each pass. The beam is recirculated up to five times into the linacs through five bending arcs connecting these linacs, so the maximum energy that can be achieved at these gradients is ≈ 5 GeV with a resolution of $< 0.01\%$ and a beam spot size at the target of < 0.5 mm. The 1.4971 GHz RF structure of the accelerator allows simultaneous delivery of polarized beams into each experimental hall with the electrons grouped into bunches separated by 2.0039 ns.

2.2 General Description of the CLAS Detector

The main experimental setup of the Hall B in Jefferson Laboratory is the CEBAF Large Acceptance Spectrometer (CLAS), shown in Fig. 2.2. CLAS is a nearly 4π acceptance detector which is capable of detecting charged particles from 8° to 140° and neutral particles from 8° to 75°. The continuous beam provided by CEBAF is well suited for carrying out experiments which require two and more particles in coincidence in the final state with a very small accidental background to signal ratio

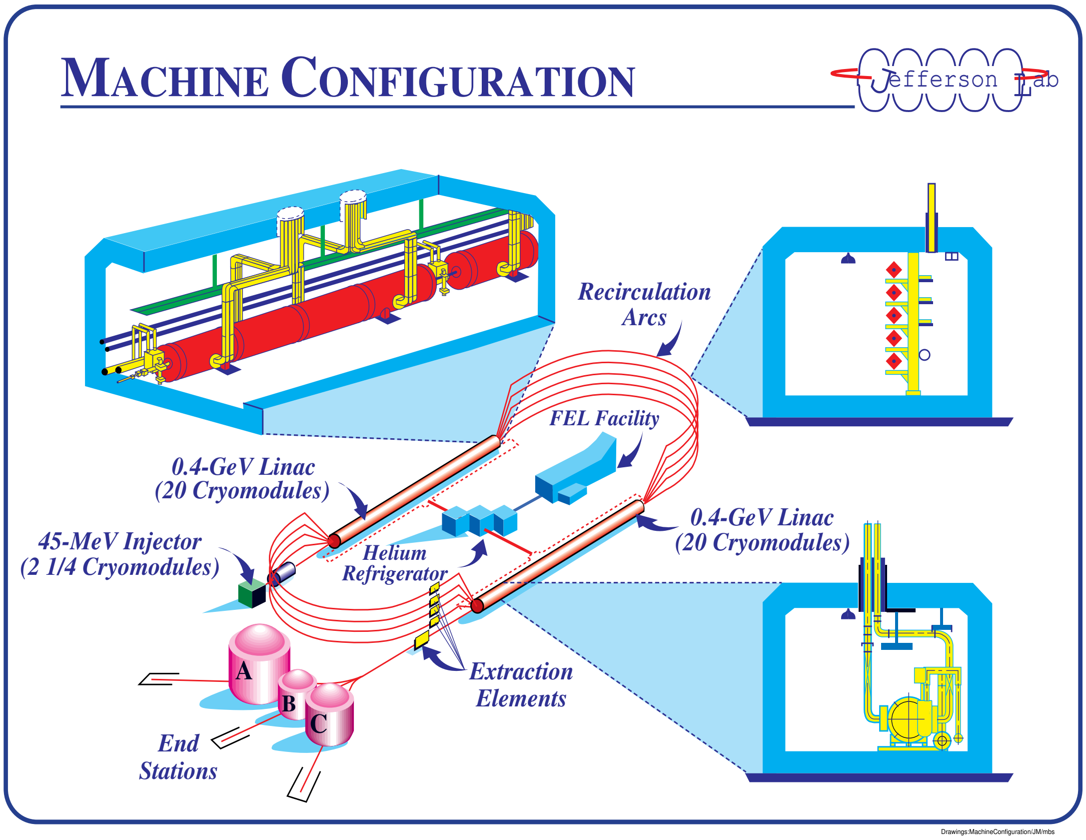

Figure 2.1: CEBAF configuration. In the upper left corner one can see a blowup of the north linac showing one of the cryomodules. A vertical cross section of a cryomodule is shown in the lower right corner of the diagram. In the upper right corner a cross section of the five recirculating arcs is shown. The two linear accelerators and the bending arcs are shown in the center of the picture. The electron beam starts at the injector and terminates at the experimental halls (Hall A, B, C).

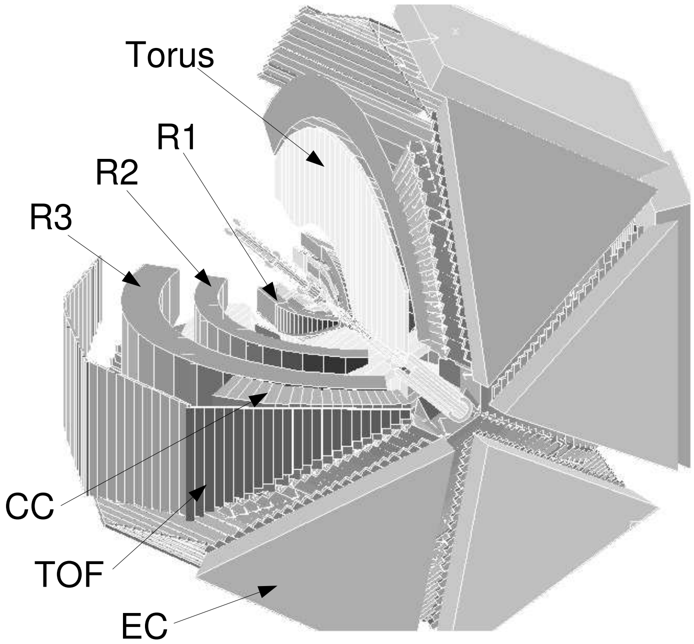

Figure 2.2: Three dimensional view of CLAS with a portion of the system cut away.

of $< 10^{-3}$ over a large angular range in the laboratory frame at luminosities up to 10^{34} cm^{-2}sec^{-1}.

The main magnetic field of the spectrometer is provided by six superconducting coils which produce a toroidal field primarily in the azimuthal direction, with the maximum intensity of 2 Tesla in the forward region. The advantage of the toroidal magnetic field is that it is nearly constant with the azimuthal angle ϕ and it only bends the trajectories of charged particles in the θ direction. The cryostats with the coils, shown in Fig. 2.3, are located symmetrically around the beam axis at 60° intervals[1] . The six gaps between the cryostats are filled with six detector packages which can function as six independent spectrometers or work together as one large multiparticle spectrometer. As shown in Fig. 2.2, each sector of the detector is instrumented with 3 regions of Drift Chambers (DC) to determine the trajectories

[1]In addition to the CLAS main torus, a smaller toroidal magnet (minitorus) was used during the e1c run period. The magnetic field of the minitorus near the target prevents the electrons from Moller scattering from flying into the detectors, thus reducing the occupancy in the drift chambers.

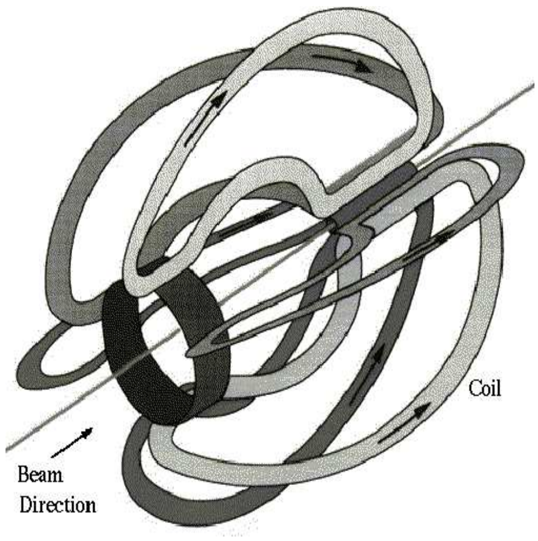

Figure 2.3: The six coils of the CLAS superconducting toroidal magnet.

of charged particles, Čerenkov Counters (CC) for electron identification, Scintillator Counters (SC) for charged particle identification using the Time-Of-Flight (TOF) method, and an Electromagnetic Calorimeter (EC) used for electron identification and detection of neutral particles. The target is located inside the detector on the beam axis. A Faraday cup, located at the very end of the Hall-B beam line, is used to determine the integrated charge passing through the target.

2.3 Multiwire Drift Chambers

Determination of the trajectories of the charged particles in CLAS is done using the multiwire drift chambers [49], which are designed to track particles with momentum greater than 200 MeV, covering from 8° to 140° in polar angle with 80% coverage of the azimuth. Each of the six sectors of the drift chambers consist of three separate regions R1, R2, R3, as shown in Fig. 2.2. The first region is the innermost and the smallest section of the drift chambers and is located in a nearly field-free volume around the target. The second region is located inside the magnetic field and is actually mounted onto the cryostats containing the coils of the magnet.

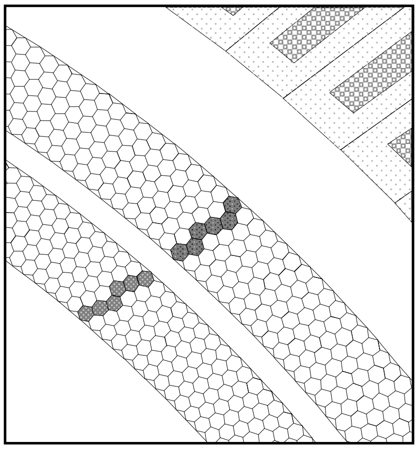

Figure 2.4: Layout of superlayers in Region 3. The sense wires are located in the center of each cell, while the field wires are located in the vertices of the hexagons. The shadowed hexagons represent the cells containing the sense wires which produced a signal for a representative track.

The third region is the biggest section and is located outside of the volume with magnetic field.

Each region of the drift chambers consists of two superlayers of wires: one axial superlayer, where all the wires are strung parallel to the directions of the magnetic field, and one stereo superlayer, in which the wires are strung at a 6° angle with respect to the axial wires. These two different directions of wires allow us to determine the azimuthal angle ϕ of the particle. Each superlayer is made up of 6 layers of sense wires, with the exceptions of the stereo superlayer in R1, which has only 4 layers. Each sense wire is surrounded by six field wires making up a cell of hexagonal shape, as illustrated in Fig 2.4. In addition, there is a layer of guard wires surrounding the perimeter of each superlayer to reproduce the electric-field configuration of an infinite grid of hexagonal cells. All three regions of the drift chambers are filled with a 90% argon, 10% CO_2 non-flammable gas mixture. This provides a drift velocity of at least 4 cm/μsec and an operating voltage plateau of several hundreds volts before breakdown. The average layer efficiency is $> 98\%$ [49].

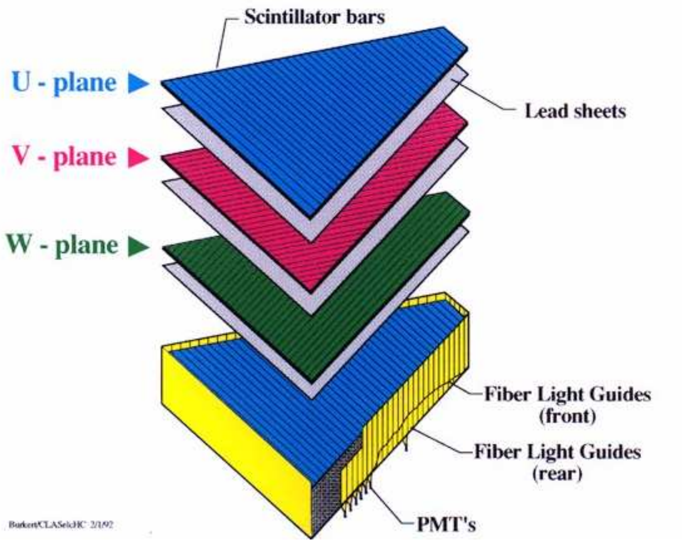

Figure 2.5: Exploded view of one of the six CLAS electromagnetic calorimeter modules.

Most of the inefficiency comes from tracks passing very close to the sense wire which give rise to signals with low pulse height and long durations.

The tracking, that is the reconstruction of the momentum and angles of the tracks, is done in two stages. First, the hits in a superlayer are combined to form a "track segment". Then the found "track segments" from different superlayers are linked to form a track. At this point the reconstructed momentum is within 3% to 5% of the true value of the momentum of the particle. In the second stage the start time information from the scintillator counters is used to obtain the drift time and then to convert it into distance from the center of the cell. In overall average the tracking efficiency remains $> 95\%$ for chamber hit occupancy up to 4% with a momentum resolution better than 0.4% [49].

2.4 Forward Electromagnetic Shower Calorimeter

2.4.1 Design

The forward regions ($8^\circ < \theta < 45^\circ$) of all six sectors of the CLAS are equipped with a 16 radiation length thick electromagnetic calorimeter (EC) [51]. The main

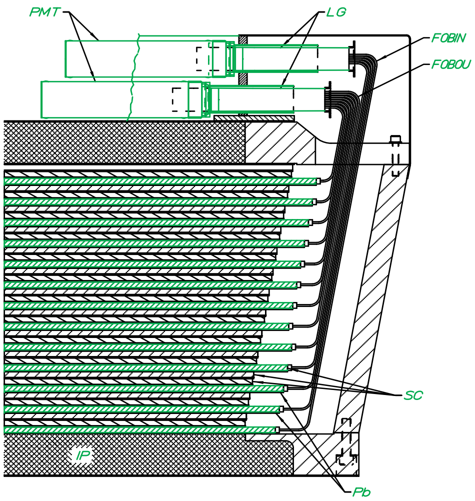

Figure 2.6: Schematic vertical cut of the EC light readout system. PMT - Photomultiplier, LG - Light Guide, FOBIN - Fiber Optic Bundle Inner, FOBOU - Fiber Optic Bundle Outer, SC - Scintillators, Pb - 2.2 mm Lead Sheets, IP - Inner Plate (Composite: two 1.905 mm Stainless Steel Face Sheets and 72.2 mm Foam Core Plate)

functions of the EC are:

- detection of electrons at energies above 0.5 GeV,
- detection of photons at energies above 0.2 GeV to allow for π^0 and η reconstruction,
- detection of neutrons and their separation from photons using the time-of-flight measurements.

The calorimeter is made of alternating layers of scintillator strips and lead sheets with the lead:scintillator thickness ratio 0.21, resulting in 39 cm of scintillator and 8.4 cm of lead per module. With this ratio, approximately 1/3 of the energy in an electromagnetic shower is deposited in the scintillator. For a good position resolution the transverse granularity has to be smaller than the transverse size of the shower. In order to achieve a compromise between the cost of PMTs and the position resolution a scintillator width of 10 cm was chosen.

In order to match the hexagonal geometry of the CLAS, the lead-scintillator sandwich is contained within a volume having the shape of an approximately equilateral triangle. There are 39 layers in the sandwich, each consisting of a 10 mm thick BC412 scintillator followed by a 2.2 mm thick lead sheet. The calorimeter utilizes a projective geometry, in which the area of each successive layer increases. This minimizes shower leakage at the edges of the active volume and simplifies the reconstruction of multiple neutral showers, such as from $\pi^0 \to \gamma\gamma$ decays.

For the purposes of readout, each scintillator layer is made of 36 strips parallel to one side of the triangle, with the orientation of the strips rotated by approximately 120° in each successive layer, as shown in Fig. 2.5. Thus there are three orientations or views (labeled U, V and W), each containing 13 layers, which provide stereo information on the location of energy deposition. Each view is further subdivided into an inner (5 layers) and outer (8 layers) stack, to provide longitudinal sampling of the shower for improved hadron identification. Each module thus requires 36(strips)×3(views)×2(stacks) = 216 photomultipliers. Altogether there are 1296 PMTs and 8424 scintillator strips in the six EC modules used in CLAS.

A fiber-optic light readout system was used to transmit the scintillator light to the PMTs. Fig. 2.6 displays a schematic side view and vertical cut of the fiber-optic readout unit for a single inner and outer stack of the calorimeter module. These fibers were bent in a controlled way to form semi-rigid bundles originating at the ends of the scintillator strips and terminating at a plastic mixing light-guide adapter coupled to a phototube. Because of the compound angles involved, each fiber bundle in a given detector module has unique dimensions.

The PMT and the light guide adapter are optically coupled using optical grease, while the light guide adapter is glued to the fiber readout bundle with a UV curing epoxy. The contact between the end of the scintillator and the fiber bundle, however, is made mechanically without optical coupling material at the joint. A special

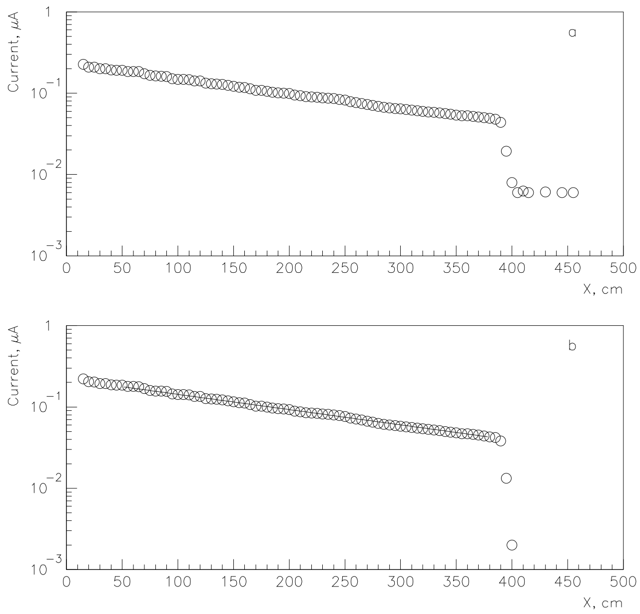

Figure 2.7: PMT anode current dependence versus ^{60}Co source position along a 4 m long BC412 scintillator strip. (a) - Measured response. For $x > 400$ cm only PMT dark current contributes. (b) - Same as (a) with dark current subtracted. Fitted parameters from (2.1) are L_1=40 cm; L_2=250 cm and $\frac{A_2}{A_1}$=0.22.

spring loaded expansion assembly is used to push the end locator, in which the fibers are glued, against the end of the scintillator. This coupling allows flexibility in positioning the scintillators in the containment box during assembly, and also prevents possible damage of the scintillator strips from thermal expansion.

2.4.2 Attenuation Lengths of the Scintillators

Each scintillator strip of the EC is 10 mm thick, approximately 100 mm wide and is 0.15-4.2 m long. One end of the strip was cut at an angle to match the edge of the triangle and coated with a non-reflecting black material to minimize the effect of reflections on the timing resolution. The read-out end was diamond milled at 90° to the axis of the strip. Before installation, each scintillator strip was measured to insure that the scintillation and optical properties as well as dimensional accuracy were within specifications. The results of the measurements were put in a database and subsequently were used to improve the simulation and reconstruction software.

In order to simulate the correct response of the calorimeter one has to know the attenuation lengths of the scintillators. The measurements were done by exciting scintillations at various points along the length of each strip, while a PMT measured the response at the scintillator read-out end [50]. To test the large number ($\approx$ 8,500) of scintillator strips in a reasonable time, several test setups were developed and operated in parallel. Scintillator strips shorter than 3.0 m were measured at University of Virginia using a 250 kW UV (λ=337.1 nm) pulsed nitrogen laser in an arrangement that permitted six strips to be tested simultaneously. Scintillator strips longer than 3.0 m were measured at the JLab using a ^{60}Co radioactive source, attached to a cart that moved along a track parallel to the scintillator strip. Although this method was slower, the use of a single, local source provided an absolute measurement.

Typical dependence of the readout PMT anode current on the source position for a 4 m long scintillator strip is shown in Fig. 2.7. A collimated 0.5 mR ^{60}Co γ source was used to excite the scintillator. The PMT was in optical contact with a lightguide placed at the readout end of the scintillator strip. There was a few millimeter wide air gap between the scintillator and the lightguide, similar to the design of the actual calorimeter readout system. The current is seen to abruptly drop to PMT dark current levels when the source reaches the far end of scintillator. This background, which is almost 13 % of the scintillation signal at this point, was subtracted from all measurements prior to fitting. The overall RMS uncertainty in the current measurement was 1.5 %.

A sum of two exponentials was sufficient to describe the scintillator attenuation response:

$$A = A_1 \cdot e^{-x/L_1} + A_2 \cdot e^{-x/L_2} \tag{2.1}$$

where L_1 and L_2 are the attenuation lengths of the two observed components. After measurements of about 100 strips it was found [51] that $\langle L_1 \rangle \leq 50$ cm, $\langle L_2 \rangle \geq 250$ cm

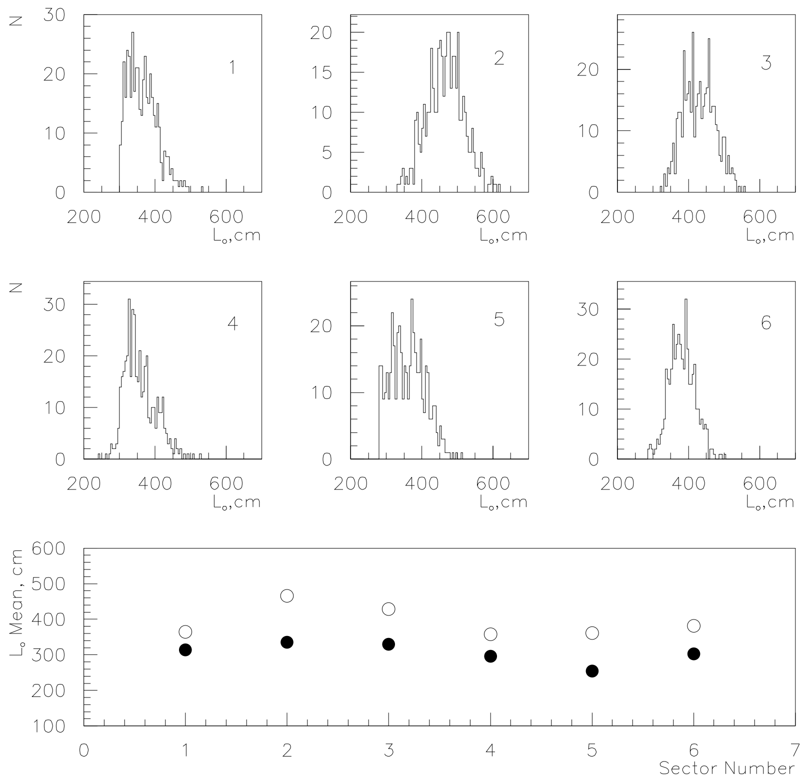

Figure 2.8: Top: Attenuation length of strips for all six sectors for scintillators having length x$\geq$300 cm. Bottom: $< L_o >$ for each sector. Open and dark circles for strips with x$\geq$300 cm and x$=$150-300 cm, respectively.

and the ratio $\frac{A_1}{A_2} \leq 0.5$. Thus, the influence of the first component at the distance of $x \approx 50$ cm was no more than 20% and for $x \geq 50$ cm the response could be fitted with a single exponential:

$$A = A_o \cdot e^{-x/L_o} \tag{2.2}$$

The fits of data for 100 strips using both Eq. (2.1) and Eq. (2.2) showed that $\frac{L_0}{L_2} = 0.98 \pm 0.03$. The results for all the calorimeter scintillators are shown in Fig. 2.8.

The preliminary calibrations and the analysis of the subsequent production runs showed that the calorimeter performed well, having an energy resolution $\frac{\sigma}{E} \leq \frac{0.1}{\sqrt{E(GeV)}}$, a position resolution $\delta r \approx 2$ cm at 1 GeV, a mass resolution for 2-photon decays $\frac{\delta m}{m} \leq 0.15$, neutron detection efficiency $> 50\%$ for $E_n > 0.5$ GeV and a timing resolution ≈ 400 ps [51].

2.5 Čerenkov Counters

In order to be able to separate electrons from hadrons at the trigger level, the CLAS detector was instrumented with threshold Čerenkov detectors [58] in the forward region of every sector out to an angle $\theta_e = 45°$. The Čerenkov counters of each sector consist of 36 optical modules, as illustrated in Fig. 2.9, divided into 18 pairs with the mid-plane of the sector as a symmetry plane between them. Each module has three mirrors - elliptical, hyperbolic and cylindrical - to direct the light into the light collection cone with a PMT attached at the end (see Fig. 2.10). All 316 PMTs are located in the region obscured by the torus so that they do not increase the material in the path of the particles passing through the CLAS. The mirrors and the other components of the Čerenkov counter are mounted on a triangular shaped aluminum frame and covered with two 0.08 mm sheets of Tedlar PVF film sandwiched around a sheet of mylar. The whole detector is filled with C_4F_{10} radiator gas which was chosen for its high index of refraction ($n = 1.00153$) and excellent light transmission properties. The efficiency of the Čerenkov counters as determined from the measured photoelectron yield is $> 98\%$ in the fiducial region [58]. Outside the fiducial regions the efficiency has very strong variation, and therefore events with the electrons in these regions are usually excluded from the analyzed data sample.

2.6 Time-of-Flight System

In order to determine masses of the charged particles passing through the detector, in addition to the momentum from the tracking one also needs to know the velocity of the particle. In CLAS this is done using the scintillator counters of the time-of-flight (TOF) system [54] located behind the Region 3 of the drift chambers. Besides, the start time from the TOF system is also used for the time-based-tracking. The resolution of the drift time determination in the DC is $\sigma_{DT} > 1$ ns, while the particle identification requires a time resolution better than 300 ps to be able to

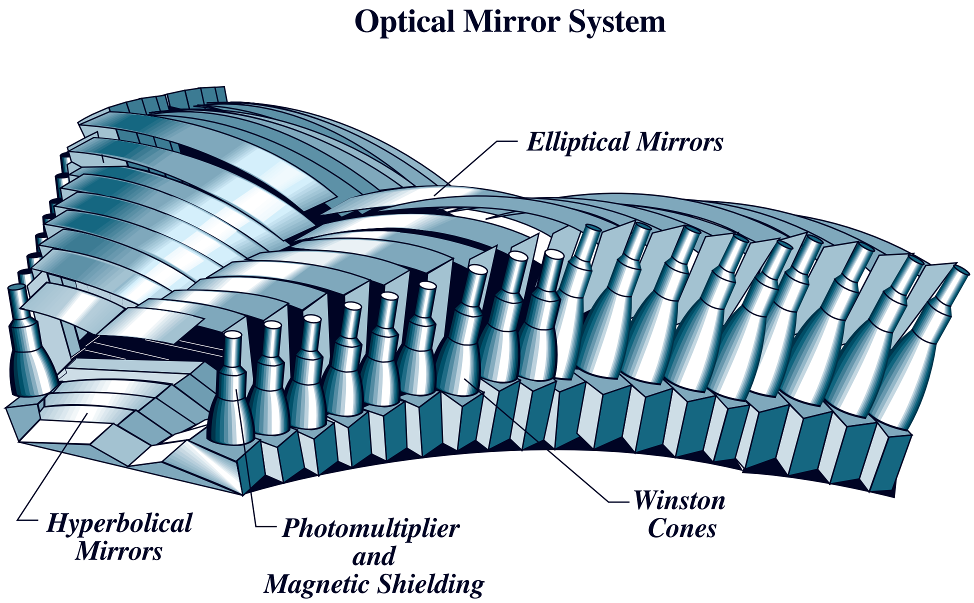

Figure 2.9: Arrangement of the CC optical modules of one sector.

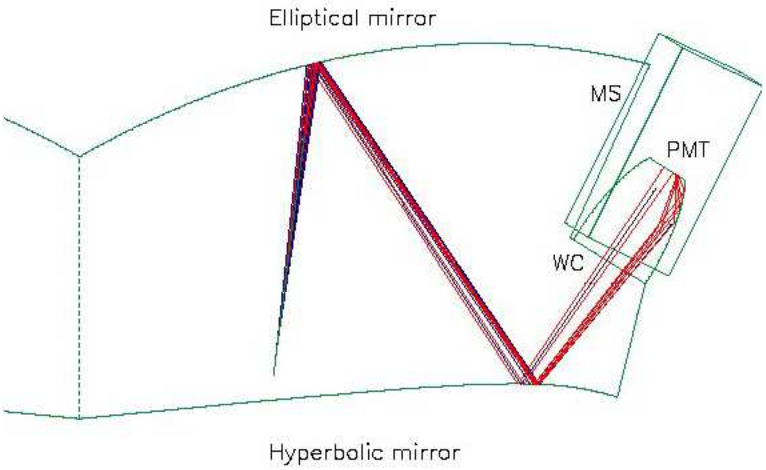

Figure 2.10: One optical module of CLAS Čerenkov counter, showing the detector components and the hypothetical light paths from electrons. Čerenkov light from electrons reflected twice from the mirrors into the Winston Cone (WC), surrounded by the magnetic shield (MS). The Winston cones are used to collect the light onto the surface of the Photomultipliers (PMT).

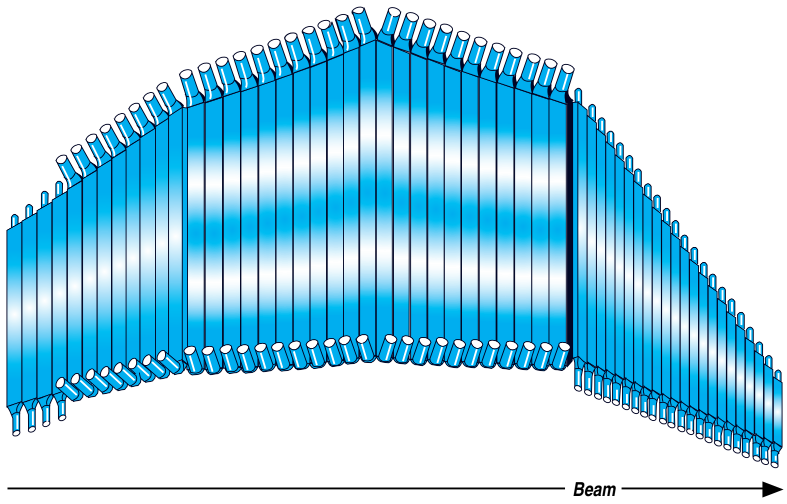

Figure 2.11: The four panels of TOF scintillators for a single sector. The length, the width and the readout configuration are different for different scintillators.

separate positive pions from protons up to 2.5 GeV momentum.

Each sector of the time-of-flight system consists of 57 Bicron BC-408 scintillator strips arranged into four panels, as shown in Fig. 2.11. The length of the scintillator paddles varies from 30 cm to 450 cm. The widths of the first 23 and the last four strips is 15 cm, while the remaining strips are 22 cm wide. The widths of the scintillators were chosen to optimize the timing resolution of a single counter and to have sufficient granularity for triggering purposes. The signal readout is done using light guides attached to both ends of each paddle. The photomultiplier is glued to the light guides. The last 18 scintillators in each sector are grouped in pairs, thus resulting in only 9 logical counters connected to a single time-digital converters (TDC) or amplitude-digital converter (ADC) channels. The timing resolution for a single counter varies with the length and the width of the strip, with a better resolution of 130 ps for the forward counters, and 300 ps for angles above 90° [54]. These timing characteristics allow for a reliable pion-proton separation up to momentum of 2.5 GeV.

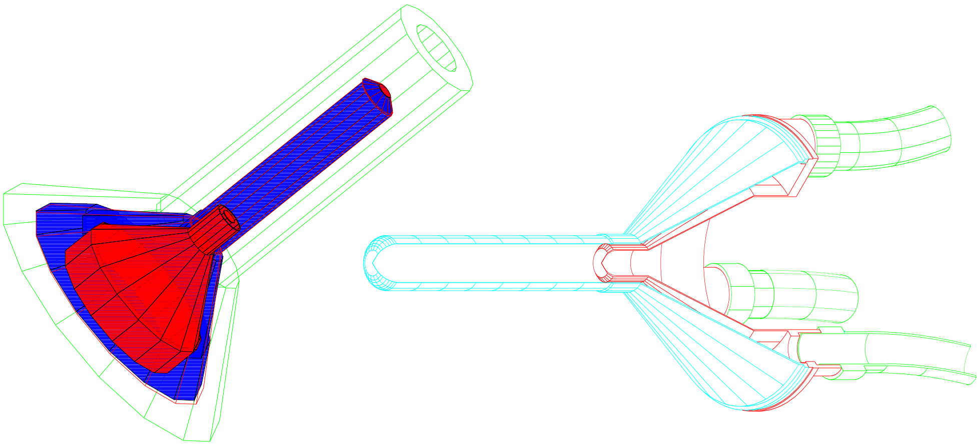

Figure 2.12: GSIM and engineering drawings of the CLAS cryogenic target cell for the e1c run period. On the left plot (GSIM image of the target) the aluminum walls are drawn in red, while polystyrene insulation is drawn in green. Hydrogen filled areas within the aluminum walls are drawn in blue. The beam line is the symmetry axis of the blue cylinder. The engineering drawing of the target (right) has aluminum walls in red (inner) and blue (outer). The pipes for hydrogen circulation are drawn in green.

2.7 Hydrogen Target

For the experiments with electrons scattering on unpolarized protons the obvious choice for the target is liquid hydrogen. In this experiment a cryogenic hydrogen target was used at an average temperature of 20.5 K. The specifications of the target are shown in Table 2.1. The target cell, shown in Fig. 2.12, was made of aluminum with 5 mm wide and 15 μm thick input and output windows [52]. The total contribution of the target cells for single π^+ rate was estimated to be $\approx 2\%$ using runs with empty target cells, as described in the next chapter. The target parameters, such as temperature and pressure, were continuously monitored during the data taking and written to a data base. Due to problems in the cryogenic system the density of the liquid hydrogen occasionally dropped down rapidly and then recovered within a few seconds. This behavior potentially can cause normalization problems and thus necessitates a careful selection of the events within the time intervals with stable target density.

Item	Value
Length	5.0 cm
Radius	0.486 cm
Temperature	20.5 K°
Density	0.0695 g/cm^3

Table 2.1: Specifications of the cryogenic hydrogen target.

EC$_{total}$	EC$_{inner}$	CC
80 mV	48 mV	20 mV
220 MeV	130 MeV	0.2 pe

Table 2.2: Trigger thresholds in the pretrigger discriminators and the corresponding approximate momentum of electrons [59] and the approximate number of photoelectrons in CC [62].

2.8 Event Trigger and Data Acquisition

During this experiment the CLAS detector had two trigger levels. The first level (Level-1) is designed to form a fast signal to enable the read-out of the information. It uses information from the pretrigger boards of the EC, CC and TOF scintillators (during this experiment the TOF was not used in the trigger) to form a coincidence signal to be sent to the Read-Out-Controller (ROCs). The Level-2 trigger uses information from the drift chambers to decide whether or not there were enough track segments to initiate an event read-out. During this experiment the Level-2 trigger was used in the Late-Fail mode when it actually does not affect the decision made by the Trigger Supervisor (TS) board, but it is recorded on the tape. This provided the information to understand the efficiency and effectiveness of the Level-2 trigger without causing any loss of events due to problems in the new Level-2 hardware.

Since the e1 running group includes many experiments, the only requirement imposed on the recorded events is that they contain an electron. In order to achieve

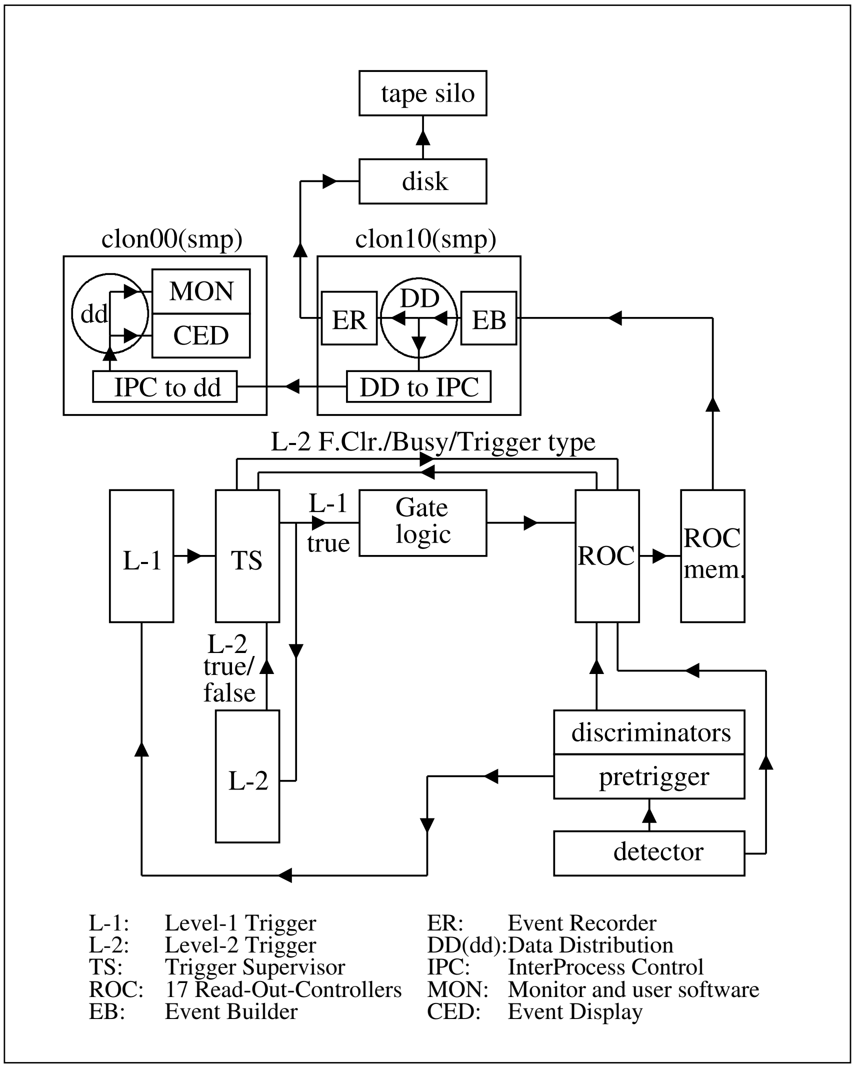

Figure 2.13: Schematic diagram for the CLAS data acquisition system. The signals from the detector go to the ROCs and the pretriggers. The pretriggers initiate the readout from the particular detector system as well as provide an input for the Level-1 trigger. In case there is a trigger the data signals are read out, digitized and transferred to a process called Event Builder (EB) running on the main computer clon10 and are temporarily stored in the Data Distribution (DD) ring in a shared memory. A process called Event Recorder (ER) writes the data onto disks from where they are transferred to the tape silo. Some of the events from the DD ring on clon10 are transferred to a different computer clon00 to be used as an input stream in the monitoring programs. (This diagram is provided by Konstantin Lukashin.)

this goal it was decided to use a coincidence between EC and CC signals in the same sector as a trigger. The thresholds for EC_{inner}, EC_{total} and CC are presented in Table 2.2. The threshold on the total deposited energy EC_{total} was chosen to reduce the background due to low energy electrons and photons. The EC_{inner} threshold was set above the minimum ionizing peak, which is at $E_{inner}^{(MIP)} \approx 31$ MeV in deposited energy, corresponding to a threshold voltage of $V^{(MIP)} \approx 38$ mV in the discriminators. Electrons, due to their showering properties, contribute significantly more energy in the forward part of the calorimeter than the minimum ionizing particles. Therefore, this additional trigger requirement only reduces the background rate due to minimum ionizing particles and does not affect the energy threshold for electrons determined by EC_{total} threshold (see Table 2.2). The CC threshold was selected to be well below the single photoelectron peak. With the above mentioned thresholds about 40% of recorded triggers contained an electron. The rest were due to the accidental background: they either did not have any reconstructible tracks, or none of the tracks passed the software electron identification cuts.

The CLAS Data Acquisition (DAQ) system consists of 17 Read-Out-Controllers (ROCs) communicating with the Trigger Supervisor board which makes the decision whether the event should be read or not. Fig. 2.13 shows the data acquisition logic. In case there is a trigger the data signals are read out, digitized and transferred to a process called Event Builder (EB) running on the main computer clon10 and are temporarily stored in the Data Distribution (DD) ring in a shared memory. From there the Event Recorder (ER) process writes the data to RAIDs (Redundant Array of Inexpensive Disks). Later the files are transferred from RAIDs to the tape silo in the computer center for permanent storage.

In order to monitor the quality of the data and to spot problems quickly a small subsets of events in the DD ring are continuously transferred to another computer, where online monitoring processes run. The status of the detector components and their functionality are continuously monitored during the runs. The most important run information are saved in the data base to facilitate the off-line analysis process.

CHAPTER 3

Charged Particle Identification

One of the essential features of the CLAS is its ability to distinguish between different types of charged particles using information from tracking and the scintillator counters. This is crucial for studying multi-particle final states involving protons, pions, kaons and deuterons. The quality of the particle identification (PID) is determined primarily by the accuracy of the time-of-flight (TOF) system, therefore considerable efforts were devoted to the development of TOF calibration procedures. In this chapter the main calibration procedures of the CLAS time-of-flight system are described. More details on this subject can be found in [54, 55, 56] and references therein.

3.1 Calibration of Individual Channels

As discussed in Chapter 2, the time-of-flight system of CLAS consists of $6\times48 = 288$ scintillator counters. Each of them has to be properly calibrated to provide the off-line analysis program with correct timing and energy information with the highest achievable resolutions. This involves calibrations of the amplitude-to-digital converters (ADCs) and the time-to-digital converters (TDCs). In addition, the dependence of the time delay on the signal amplitude, arising from the leading-edge discriminators generating the logical signals, must be taken into account. This is referred to as a "time walk correction". Only after these calibrations for individual channels are completed one can proceed with the adjustment of the time delays for different scintillator counters with respect to each other.

3.1.1 ADC Pedestals and TDC Calibrations

In order to determine the ADC pedestal values, special runs with a random trigger were taken [56]. The data were analyzed online and the results were loaded into a calibration database. An additional sparsification threshold of 40 ADC channels was added to the pedestals and loaded into the 1881M FASTBUS ADC. This helped to avoid reading low voltage noise in the ADC.

A special DAQ configuration was used to take the TDC calibration data [56]. All TDC channels in all crates were pulsed and the response of the TDC for different delays between the **start** and **stop** signals were analyzed. A quadratic equation was used to convert the TDC channel number T to time units (ns) :

$$t = c_0 + c_1 T + c_2 T^2. \tag{3.1}$$

The constant terms c_0 were constrained so that the average of the 64 channels of each FASTBUS card was zero. The value of the c_0 parameters are not significant, because more calibrations are performed afterwards to equalize the left-right timing offsets for every single counter and then to determine the relative offsets between different time-of-flight counters.

3.1.2 Energy Calibrations

For a high quality timing calibration of the CLAS time-of-flight system, it is important to be able to separate pions from protons without using any timing information from the scintillator counters. One of the ways of doing this is to use the dependence of the energy deposited by hadrons on the momentum. In order to find the deposited energy, ADC pulse heights first are corrected for the pedestal value P. Then the energy is found by calculating the geometrical mean of the signals from the left and right ADCs [57]:

$$\bar{A}_g \equiv \sqrt{A_L \cdot A_R} = \frac{\alpha}{2} E_d \exp\left(-\frac{L}{4}\frac{\lambda_r + \lambda_l}{\lambda_r \lambda_l}\right) \exp\left(\frac{y}{2}\frac{\lambda_r - \lambda_l}{\lambda_r \lambda_l}\right), \tag{3.2}$$

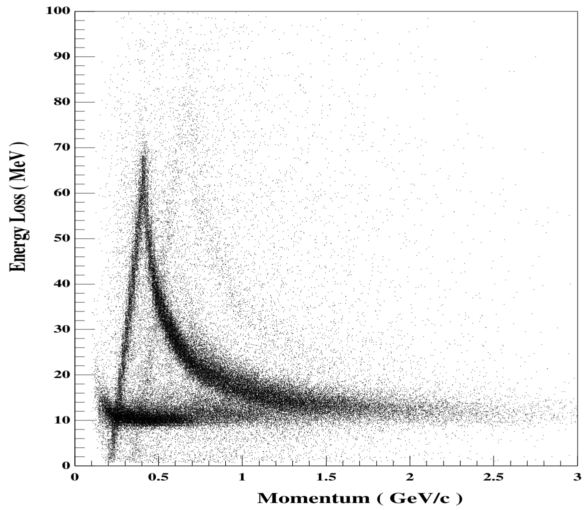

Figure 3.1: Energy deposited by hadrons in the TOF scintillators versus momentum from tracking after the MIP calibration is done. Proton and pion bands are clearly distinguishable. A faint band corresponding to deuterons is visible as well.

where A_L and A_R are the pulse heights from the left and right ADCs, E_d is the deposited energy, L is the scintillator length, y is the hit position along the scintillator, λ_l and λ_r are the attenuation lengths in two directions, and α is a conversion constant from MeV units to ADC channels. The product $\frac{\alpha}{2}\exp\left(-\frac{L}{4}\frac{\lambda_r+\lambda_l}{\lambda_r\lambda_l}\right)$ can be found using normally-incident minimum ionizing particles (MIPs) [54]. A plot of the deposited energy in the counters versus the particle momentum after the energy calibrations is shown on Fig. 3.1. At low momentum, pions and protons can easily be separated, while at momentum above 800 MeV protons become minimum ionizing, and the bands in Fig. 3.1 corresponding to pions and protons start to merge. Note, that this method of pion identification is not suitable for data analysis and it is only used to provide a reasonably clean sample of pions for further calibrations.

3.1.3 Time Walk Corrections

The time walk corrections were obtained using a laser system which delivered a light pulse to the center of each scintillator counter [56]. The intensity of the light was varied using a neutral density filter, and the pulse heights and the times were measured at the both ends of the counter. The time, corrected for amplitude dependent delays, is determined using the formula:

$$\begin{aligned} t_w &= t - f_w\left(\frac{A-P}{Th}\right) + f_w\left(\frac{600}{Th}\right), \\ f_w &= \frac{w_2}{x^{w_3}}, \quad \text{if } x < w_0, \\ f_w &= \frac{w_2}{w_0^{w_3}}(1+w_3) - \frac{w_2 w_3}{w_0^{w_3+1}}x, \quad \text{if } x > w_0, \end{aligned} \tag{3.3}$$

where t is the measured uncorrected time, A is the pedestal unsubtracted ADC channel number, P is the position of the pedestal, Th is the channel corresponding to the leading-edge discriminator threshold of 20 mV, $f_w(x)$ is the time-walk correction function, obtained from fitting laser calibration data. The three variables in Eq. (3.3) w_0, w_2, w_3 are the calibrations parameters obtained from the fit.

3.2 Paddle-to-paddle Calibrations

After all individual scintillator counters have been calibrated, one has to ensure that their signals are delayed in software by the same amount with respect to a single reference time. This delay for each counter is represented by a single number, because the time of a TOF hit is calculated as the average of the times from the two ends of the fired scintillator [57]:

$$T_{hit} = \frac{T_{left} + T_{right}}{2} - y\frac{v_r - v_l}{2v_r v_l}, \tag{3.4}$$

where T_{left} and T_{right} are the times measured by the two TDCs, and v_r (v_l) is the the speed of light propagation toward the right (left) tube.

The RF-signal from the accelerator was used as the reference timing signal for the CLAS particle identification [55]. This signal is generated for every electron bunch with frequency of $\nu_{acc} = 1.4971$ GHz at the CEBAF injector and is sent to the three experimental halls with a prescale factor of 40. Each real event in the CLAS

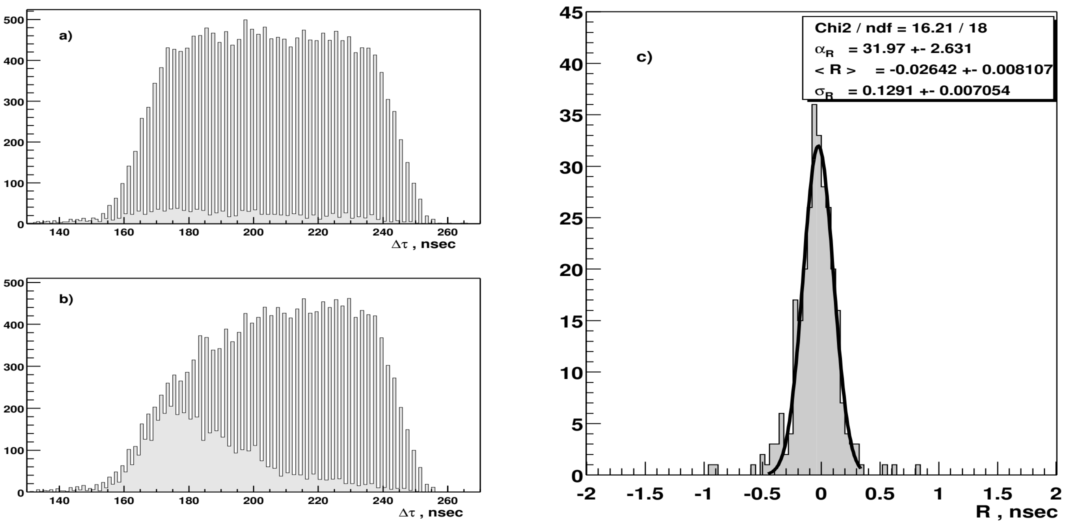

Figure 3.2: Illustration of the beam RF-structure: a) $\Delta\tau$ distribution with properly calibrated TDCs, b) $\Delta\tau$ distribution when the c_1 parameter of the TDC of the RF-signal is miscalibrated by less than 1%, c) R-distribution for a single scintillator channel, fit to a Gaussian.

detector is caused by an electron from one of these bunches. Ideally, one would like to be able to identify the bunch containing the electron which caused a particular event. But this is impossible to do, because only one out of forty RF-signals is sent to the experimental halls. Nevertheless, for the TOF calibration purposes, it is adequate to be able to align the timing of all scintillator counters to the same RF bunch, because all electron bunches delivered into Hall B are separated by a constant time interval. The sections below describe this procedure in detail.

3.2.1 Fine Tuning

As mentioned above, the CEBAF beam is delivered to Hall-B in bunches, separated by time intervals:

$$\Delta T = \frac{3}{\nu_{acc}} = \frac{3}{1.4971 \text{ GHz}} \approx 2.0039 \text{ ns}, \tag{3.5}$$

where ν_{acc} is the RF frequency of the accelerator, and the factor of 3 is present because the beam from the injector is shared among the three experimental halls.

For every Hall-B beam bunch an RF-signal is generated and is sent to the experimental hall with a prescale factor of 40. In the first step of the counter-to-counter calibration all scintillator strips are aligned to one of the RF-signals coming to the experimental hall. One can calculate the difference between the event start time, using the signal from the hit scintillator counter, and the RF time as:

$$\Delta\tau = T_{sc} - T_{flight} - T_{rf}, \tag{3.6}$$

where T_{sc} is the time in nanoseconds measured by the scintillator, T_{flight} is the flight time of the particle from the vertex to the scintillator, T_{rf} is the time when RF-signals arrives to the TDC in Hall B. All these times are measured with respect to the CLAS trigger signal. The distribution of the number of events versus $\Delta\tau$ for a single channel is shown in Fig. 3.2 a . The multiple peaks on this plot arise because only one out of forty RF-signals is sent to Hall-B, while the observed event can be caused by an electron from any of the forty electron bunches. The peaks must be separated by exactly 2.0039 ns if the TOF TDCs and the TDC of the RF-signal are calibrated correctly. In fact, this plot is a sensitive test with respect to the TDC calibrations [55], since in case of miscalibrated TDCs one can see a pattern similar to one shown in Fig. 3.2 b . Extra corrections may be needed to the c_1 TDC calibration parameter, defined in Eq. (3.1), if this kind of pattern appears in the plot in Fig. 3.2.

For each scintillator counter the time offset, defined as [55]:

$$R = mod\left(\frac{T_{sc} - T_{flight} - T_{rf} + 100 \cdot \Delta T}{\Delta T}\right) - \frac{\Delta T}{2}, \tag{3.7}$$

determines how much the time measured by the scintillator counter T_{sc} should be delayed to be aligned with the RF-signal. In Eq. (3.7) ΔT is the RF time interval defined in Eq. (3.5). The distribution of events versus R for a single time-of-flight channel is shown in Fig. 3.2 c. The position of the peak defines the time offset

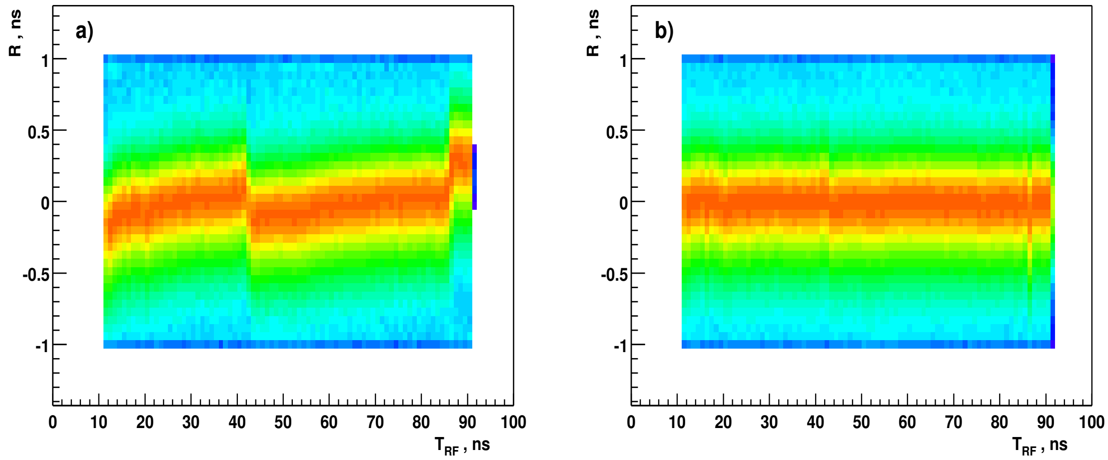

Figure 3.3: Two dimensional plot showing dependence of R versus T_{rf} for a) uncalibrated RF-signal, b) calibrated RF-signal.

to be subtracted from the T_{sc}, when calculating the mass of the particle using the time-of-flight information. The width of the distribution depends on the timing characteristics of the scintillator, the quality of the calibration for that particular channel, and the TDC calibration of the RF-signal. If the RF-signal TDC is mis-calibrated, then the dependence of R on T_{rf} will have a slope. In addition, the hardware in Hall B causes additional distortion of that plot, as shown in Fig. 3.3 a. A procedure, described in [56], was developed to address the calibration of the RF-signal. After a proper calibration the R versus T_{rf} distribution must look like a horizontal band, as illustrated in Fig. 3.3 b. Then one can vary the slope parameter of the scintillator TDC calibration to find the value which produces the most narrow width for the R-distribution, shown in Fig. 3.2.

Once the RF and the time-of-flight TDCs are calibrated to produce satisfactory plots, shown in Figs. 3.2 a, c and Fig. 3.3 b, one can start fitting the R-distributions for every counter with a Gaussian to determine the peak positions. The obtained values are called “fine tuning constants”. Since the electrons are predominantly produced in the forward direction, pions must be used to determine the fine tuning constants for the backward strips. The disadvantage of using pions is that, unlike for electrons, their speed can be significantly slower than the speed of light, and therefore one has to use the pion momentum from tracking to determine their velocity. The use of protons is even less desirable, because they have significant energy losses on their way to the scintillators. Because of the reasons mentioned above, the fine tuning of the forward scintillators from #1 to #20 is done using electrons, while the remaining channels are calibrated using pions, identified by analyzing the energy deposition dependence on the track momentum, shown in Fig. 3.1.

Most of the channels give R-distributions consistent with a Gaussian, while the channels from #40 and up may produce double peaks, caused by the fact that two actual scintillator strips are connected to a single electronic channel [54]. For the low energies, the timing resolution of $\sigma_t \approx 2$ ns is enough to reliably separate pions and protons at such large angles, because these tracks typically have momentum less than 1 GeV.

3.2.2 Crude Tuning

After the fine tuning has been done, all scintillator counters are aligned with the RF-signals. But there still can be an offset between different paddles, because their timing might be aligned with RF-signals corresponding to different electron bunches. Therefore, any time offset between any two channels must be a multiple of 2.0039 ns. A procedure was developed [55] to resolve this ambiguity in selection of the reference timing signal using the events containing an electron and at least one pion. The following subsections describe the three stages of the procedure, also known as “crude tuning”.

Alignment of the Forward Channels in Each Sector.

In the first step of crude tuning, the time delays for the first ten channels in each sector are equalized. Events containing an electron with a signal in the first ten channels of a sector, and a pion, hitting a reference scintillator counter in one of the other sectors, are selected. The reference channel usually used is counter #28 in the sector next to the opposite to the sector, containing the electron. The reason why the opposite sector itself is not chosen, is that there are many hits coming from the elastic protons, which create a significant background for the pion events. The reference channel can be changed in cases when channel #28 in one of the sectors is malfunctioning. The difference between the vertex times calculated from the electron and the pion, defined as:

$$\delta t_{vtx} \equiv (T^e_{sc} - T^e_{flight} - T^e_{ft} - R^e) - (T^\pi_{sc} - T^\pi_{flight} - T^\pi_{ft} - R^\pi), \qquad (3.8)$$

is a multiple of 2.0039 ns, and therefore, a few events for a pair of channels are enough to determine the number of bunches separating the two channels. In Eq. (3.8) the T^e_{sc}, T^π_{sc} and T^e_{flight}, T^π_{flight} are the TDC times and the flight times for the electron and the pion, respectively. T^e_{ft} and T^π_{ft} are the fine tuning offsets for the counters hit by the electron and the pion, respectively. R^e and R^π are the moduli for the electron and pion channels, defined in Eq. (3.7). Sample distributions of the number of events versus δt_{vtx} are shown in Fig. 3.4. Only bins with δt_{vtx} values multiple of 2.0039 ns are occupied. The tallest occupied bin determines the required time offset. For instance, the counter represented in Fig. 3.4 a needs an extra 2.0039 ns offset, while the counter in Fig. 3.4 b does not need any additional timing adjustment. From the definition in Eq. (3.8) it follows that the δt_{vtx} delay should also be subtracted from the time measured by the scintillator containing the signal from the electron.

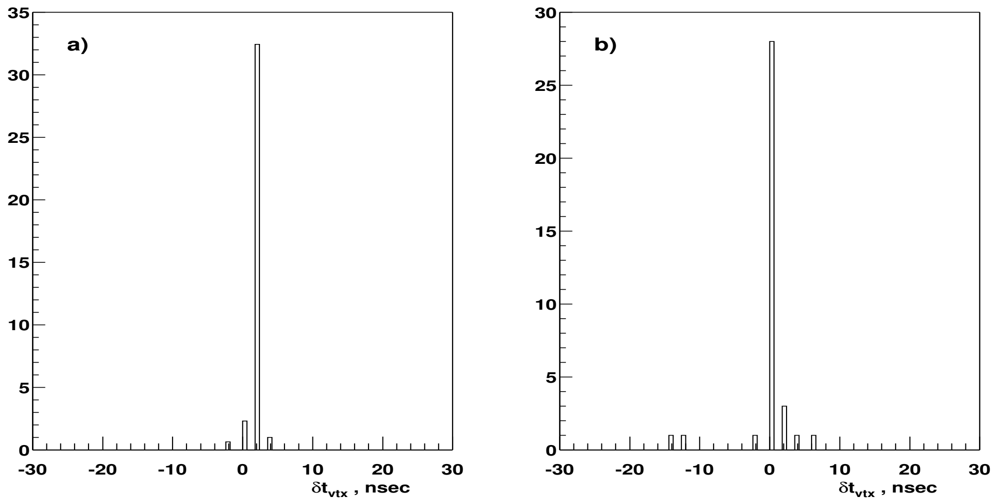

Figure 3.4: Distribution of number of events versus δt_{vtx}, defined in Eq. (3.8), for two different counters. a) the maximum number of events is detected with $\delta t_{vtx} = 2.0039$ ns; b) the maximum number of events is detected with $\delta t_{vtx} = 0$ ns.

Alignment of All Sectors.

Once the timing for the first ten channels of all sectors are aligned, one has to find the relative delays between different sectors, which again can only be multiple of 2.0039 ns. To find these timing offsets, we use events with an electron in one of the ten forward scintillator counters of the sector being calibrated, while the pion is required to be detected in the first ten counters of Sector 1. Thus Sector 1 is used as a reference. The difference between vertex times calculated with the electron and with the pion, defined as:

$$\begin{aligned} \delta t_{vtx} \;\; \equiv \;\; & (T^{e}_{sc} - T^{e}_{flight} - T^{e}_{ft} - T^{e}_{f10} - R^{e}) - \\ & (T^{\pi}_{sc} - T^{\pi}_{flight} - T^{\pi}_{ft} - T^{\pi}_{f10} - R^{\pi}), \qquad (3.9) \end{aligned}$$

indicates the number of bunches which separates Sector 1 from the other five sectors. By definition, this number is zero for Sector 1. In Eq. (3.9) T^{e}_{f10} and T^{π}_{f10} are the constants obtained in the previous subsection. As before, the δt_{vtx} delay for different sectors should be subtracted from the measured time.

Alignment of the Backward Scintillators.

The final step in the paddle-to-paddle calibration procedure is the alignment of the time delays for the channels from #11 to #48. For these purposes events containing an electron and at least one pion are used. The electron is required to be detected in any counter from #1 to #10 in any sector, while the pion should have a signal in the scintillator being calibrated. The vertex time difference

$$\begin{aligned}\delta t_{vtx} \equiv\ & (T^e_{sc} - T^e_{flight} - T^e_{ft} - T^e_{f10} - T^e_{sec} - R^e) - \\ & (T^\pi_{sc} - T^\pi_{flight} - T^\pi_{ft} - T^\pi_{f10} - T^\pi_{sec} - R^\pi) \qquad (3.10)\end{aligned}$$

defines the time delay for the scintillator hit by the pion. Here, T^e_{sec} and T^π_{sec} are the time delays for sectors, determined in the previous subsection. This step concludes the crude tuning procedure. The fine tuning and crude tuning constants for each counter are added into a single time offset to be subtracted from the measured time.

3.3 Alignment of the TOF System to the RF-signal.

In order to determine the hadron mass using its flight time, one has to know the start time of the event. For the electron runs the natural choice would be using the electron timing to determine the start time of the event at the vertex. Then the flight time of the hadron and the corresponding resolution are given by:

$$T_{flight} = T^\pi_{sc} - \left(T^e_{sc} - \frac{L^e_{track}}{v_{el}}\right), \qquad (3.11)$$

$$\delta T_{flight} = \sqrt{\delta T^{\pi\,2}_{sc} + \delta T^{e\,2}_{sc} + \left(\frac{\delta L^e_{track}}{v_{el}}\right)^2}, \qquad (3.12)$$

where L^e_{track} is the length of the electron track from the vertex to the scintillators, v_{el} is the speed of the electron, approximately equal to the speed of light. In Eq. (3.12) the uncertainty of the electron speed determination is neglected. The electron timing resolution δT^e_{sc} makes a significant contribution into the uncertainty of the determination of the flight time. One of the ways of eliminating the contribution from the electron timing errors and improving the resolution of the hadron flight time is to use the RF-signal to determine the event start time. In fact, after the paddle-to-paddle calibration procedure is complete, the timing of all scintillator counters are adjusted to the same RF bunch. Therefore, the RF-corrected flight time, defined as:

$$T_{flight} = T^{\pi}_{sc} - \left(T^{e}_{sc} - \frac{L^{e}_{track}}{v_{el}} - R^{e} \right), \tag{3.13}$$

$$\delta T_{flight} = \sqrt{\delta T^{\pi\,2}_{sc} + \left(\frac{\delta L^{e}_{track}}{v_{el}} \right)^{2}}, \tag{3.14}$$

can be used to calculate the velocity of hadrons. Equation (3.14) is valid as long as all time-of-flight counters are adjusted with respect to the RF-signal. But because the tuning of the beam can change the path length of the electrons from the injector to the target, and because the signal propagation speed in the cables can vary with time, this alignment should be done for each run. In addition, one may need to use an additional correction for the z-position of the vertex for runs with an extended target ($L_{tgt} \geq 10$ cm) [56].

3.4 Results of the Calibration

The purpose of the procedures described above is to allow the CLAS off-line analysis software to reliably distinguish between different types of hadrons and to use the missing mass technique to select different multi-particle final states. The timing resolution, determined by the time-of-flight calibrations, directly affects the level of non-physical background for different final states with two or more detected particles. The quality of the PID calibration procedures can be monitored using different histograms. The dependence of β of the charged particle on its momentum, for all scintillator counters combined, is shown in Fig. 3.5. The data sample for this plot includes a loose kaon cut, which leads to enhancement of the kaon band relative

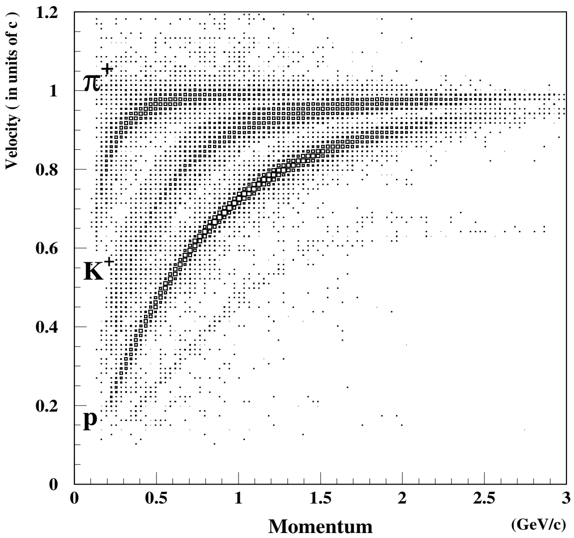

Figure 3.5: Velocity of positive hadrons versus momentum. The kaon band was artificially enhanced by preselecting events in the data sample with a loose kaon cut.

to the other particle types. The pion and proton bands are reliably separable up to a momentum of 2.5 GeV.

Knowing the velocity and the momentum of the hadron one can calculate its mass. The mass spectrum from an empty target run at 4 GeV electron beam energy is shown in Fig. 3.6. During this run the electrons scattered mostly from the aluminum walls of the target cell. In addition to the proton, pion and the small kaon peaks, one can see enhancements due to deuterons and tritons as well. The dependence of the hadron mass squared, determined using the scintillator counters and tracking, versus TOF strip number for all six sectors is shown in Fig. 3.7. The two clearly identifiable horizontal bands correspond to protons and pions. Using this plot one can determine if a particular channel is malfunctioning or is not properly calibrated.

At very low momentum the resolution of the TOF system is adequate for separation of positrons, pions and muons from pion decays, as illustrated in Fig. 3.8. The selected charged particles are required to have momentum $P < 0.25$ GeV and

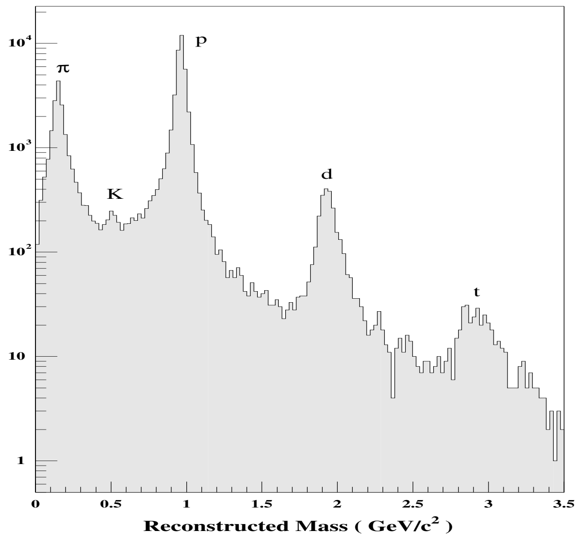

Figure 3.6: Mass spectrum of hadrons from an empty target run at $E_b = 4$ GeV. Clearly visible are the peaks corresponding to pions, kaons, proton, deuterons and tritons.

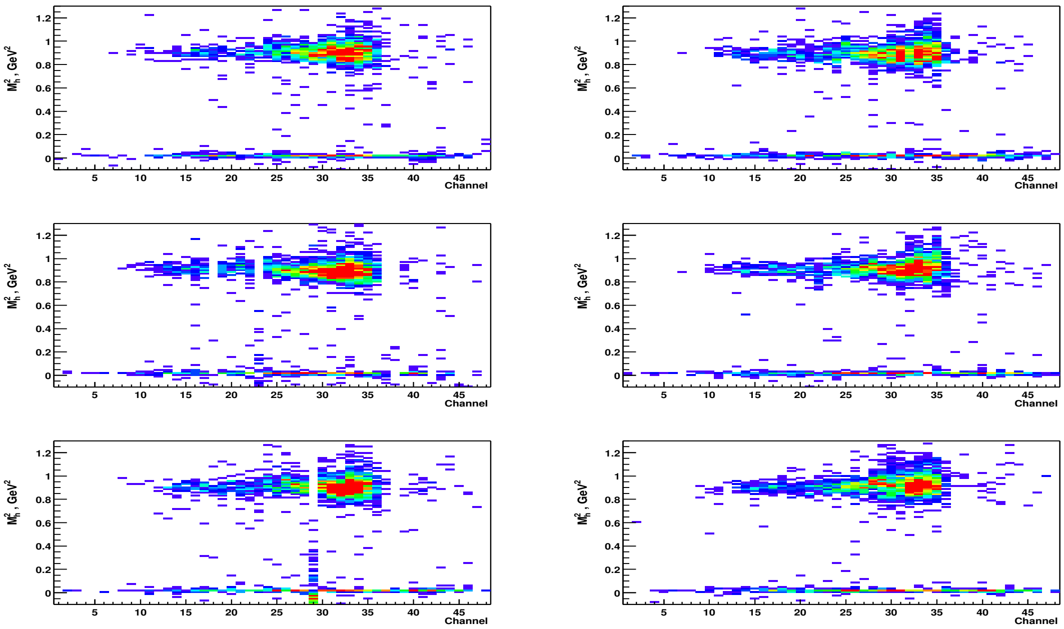

Figure 3.7: Mass squared of hadrons versus TOF channel number for all six sectors of CLAS at electron beam energy $E_b = 1.515$ GeV and torus current $I_t = 1500$ Amps.

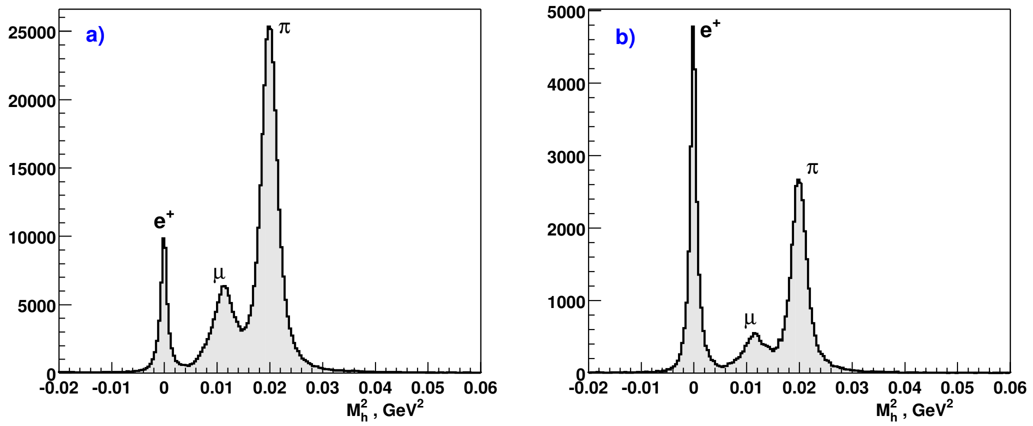

Figure 3.8: Mass squared for backward flying particles with momentum $P < 0.25$ GeV: a) without any sector cut; b) electron and the other particle are required to be in the same sector.

have a signal in the scintillator counters above #20. In Fig. 3.8 b only events with the electron and the other charged particle in the same sector are selected in order to enhance the positron peak. The feasibility for separation of these three types of particles is strongly momentum dependent, because at higher momentum the mass resolution deteriorates and these peaks merge. For this reason the default CLAS particle identification procedure always presumes all these particle to be pions.

The particle identification in the CLAS off-line software is done in the Simple Event Builder (SEB) package [59]. This package is responsible for the default electron identification, determination of the start time for the time-based-tracking, matching hits in different detector components into a single particle, and the particle identification. The start time for the particle identification and time-based-tracking[1] for electron runs is found using the formula:

$$t_{start} \equiv T^e_{sc} - T^e_{flight} - R^e, \tag{3.15}$$

where T^e_{sc} is the fully corrected time from the counter hit by the electron, T^e_{flight} is the

[1]The T^e_{flight} used to calculate the start time for time-based-tracking is based on the path length from hit-based-tracking, while T^e_{flight} for particle identification is based on path length from time-based-tracking, whenever available.

time of flight of the electron from the vertex to the scintillator plane, and R^e is the modulus defined in Eq. (3.7). In order to identify the type of the particle, the SEB package calculates the velocity β_{meas} of the detected particle and compares it with the expected β_{cand} corresponding to the measured momentum for different possible types of particles. The type of the particle is chosen based on the minimum difference between the measured β_{meas} and expected β_{cand}. The full set of the possible particle types in the SEB package consists of electrons, pions, kaons, protons, deuterons, ^{3}H, neutrons and photons. The last two neutrals are identified using the timing information from the electromagnetic calorimeter. Depending on the run conditions and the experimental goals the set of the candidate particles can be reduced in order to avoid losses of events due to possible particle misidentifications.

CHAPTER 4
Analysis

This thesis is based on the experimental data taken during the 1999 e1c run period with the electron beam energy of $E_b = 1.515$ GeV. The main analysis is performed on ≈ 450 million triggers taken at the $I_t = 1500$ Amps torus current setting, while the data taken with $I_t = 2250$ Amps was used to check the consistency of the results. The e1c run group consists of fifteen different experiments, therefore the running conditions were chosen to satisfy the requirements of all experiments, with higher priority given to the experiments with higher scientific ratings from the Program Advisory Committee. The calibration and data reduction procedures were done jointly by the entire e1c run group, while the physics analyses were performed separately by the individual groups associated with each experiment. The analysis of the data to obtain the single π^+ electroproduction cross sections is described in this chapter.

4.1 Data Reduction and Processing

The raw data from the CLAS detector were recorded on the tapes of the JLab tape silo in BOS format files [60]. After the calibration of all subsystems was finished, these files were retrieved from the silo and processed using the off-line analysis procedure described in [61]. For each raw data file a single job was launched on the JLab Linux batch farm. In each job a raw data file was analyzed and an output ("cooked") BOS file was produced. Then a sequence of filtering programs, selecting a significantly reduced data sample, were run on the output files to produce filtered BOS files, which contained the same BOS banks [60] but for far fewer number of events. The filtering procedure is effective for reactions with relatively small cross sections, such as processes involving kaon production. In addition, HBOOK files, containing standard ntuples, were produced from the cooked files. The ntuple files are relatively smaller in size than the cooked files and contain information from only the essential BOS banks. This makes them more convenient for a fast analysis, involving a smaller subset of total events.

The analysis, described in this paper, was done using general cooked files without any prefiltering. A code was developed to scan through the events in a file, selecting single π^+ event candidates, elastic event candidates and events which contain at least one deuteron. These events were written as ntuples into files in ROOT format, one file per cooked file. In addition to the ntuples for the actual events, the ROOT files had an ntuple containing information about live-time, elastic and single π^+ rates, as well as the charge corresponding to the events in the file. The output ROOT files were about a hundred times smaller than the original "cooked" files. This allowed us to keep all the files corresponding to the 1.515 GeV electron beam energy on the hard disks at JLab.

A separate program was developed to use the ROOT ntuples to calculate the cross sections. First, the events accumulated during times of unstable target density were identified and flagged as "bad". Then, the program scanned through the remaining "good" single π^+ events to produce the differential cross sections, which were then written into an ASCII file on the hard disk. Finally, different types of corrections, described below, were applied to obtain the final cross sections.

4.2 Electron Identification

One of the key issues in the electron scattering experiments is the ability of the detector to reliably identify electrons. One should be able to recognize as many scattered electrons as possible without significantly contaminating the data sample.

Matching	Tolerance
$TRK \otimes EC$	30 cm
$TRK \otimes CC$	5^o
$EC \otimes CC$	5^o

Table 4.1: Cuts for the geometrical matching in the SEB package.

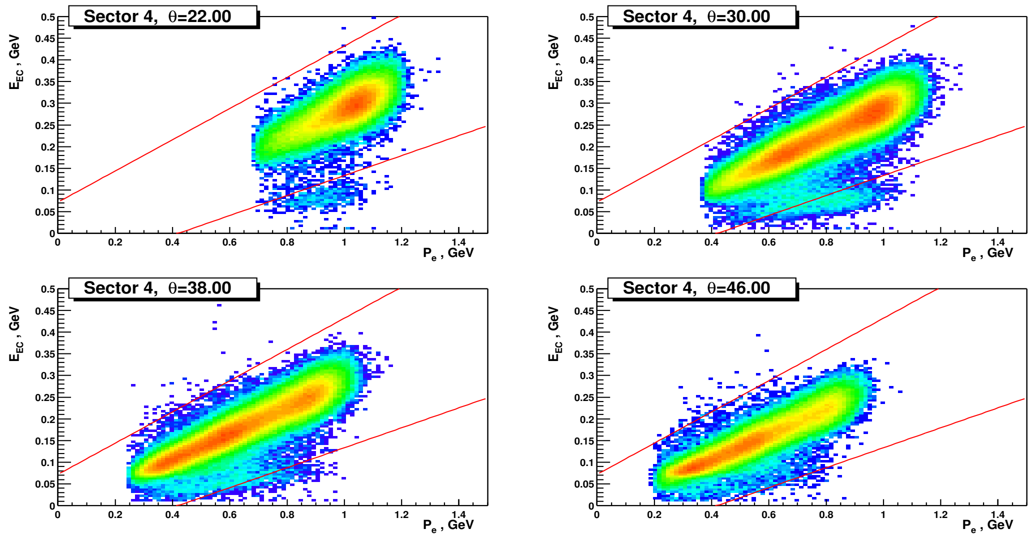

Figure 4.1: Visible energy deposited in the calorimeter versus momentum of the electrons for different electron scattering angles for Sector 4. Energy deposition was calculated by treating the whole sector as one module. The red lines show the cuts which must be satisfied by at least one of the methods of calculating the total energy in EC. Events outside the cuts satisfy the conditions with the total EC energy defined as $EC_{tot} \equiv EC_{in} + EC_{out}$.

CLAS electron identification at the trigger level is done by requiring a minimum amount of energy in the electromagnetic calorimeter (EC) in coincidence with a signal in the Čerenkov counter (CC). In the off-line analysis some additional requirements were used to select events with a good electron. First of all, one requires that the EC and CC hits are geometrically matched with a track reconstructed in the drift chambers (DC). The values of the geometrical cuts in the SEB software package are shown in Table 4.1.

Secondly, one has to ensure that the matched hits are caused by an electron and are not due to accidental background. In order to achieve this, a sampling fraction cut was used in the EC. The total energy deposited in the calorimeter can be calculated in two ways. Either one treats the inner and outer layers of one sector of the EC as a single module and calculates the total energy, or one adds the deposited energies in the inner and outer layers to obtain the total energy. The two ways give very close numbers for most events, and the differences occur due to close multiple hits in the calorimeter [59]. In this analysis the electron candidates satisfying the cuts using at least one of the two definitions of the EC total energy were considered as electrons. In Fig. 4.1 the cuts and the total deposited energy calculated by the first method for identified electrons versus their momentum are shown. As one can see, there are some events that are outside the cuts; for these events the conditions using the second method were satisfied. To eliminate the minimum ionizing particles, we also required a 40 MeV threshold on the visible energy in the inner part of the calorimeter. The loss of events due to the EC cuts are expected to be reproduced in the GSIM simulation [63] as a part of the acceptance corrections. The electron identification logic used in the off-line analysis can be summarized by:

$$EID = TBT \otimes CC \otimes EC \otimes EC_{in} \otimes [SF_1 \oplus SF_2]\,, \tag{4.1}$$

where TBT is the time-based tracking, CC and EC are the Čerenkov counter and the calorimeter geometrically matched hits, EC_{in} is the cut on the energy in the inner part of the calorimeter, SF_1 and SF_2 are the two sampling fraction cuts described above.

Unfortunately, the simulation of the response of the Čerenkov counter is an extremely difficult task and is not implemented in GSIM. To overcome this, only events within fiducial regions, where the CC efficiency is above 92%, were used in the analysis. The remaining inefficiency was taken into account with a function which calculates the efficiency of the Čerenkov counters versus position of the electron on

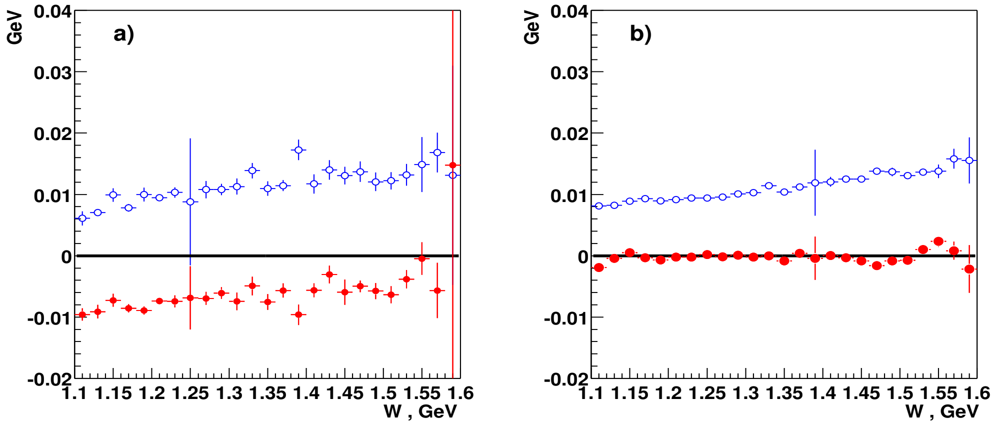

Figure 4.2: Deviation of the missing mass peak position from the neutron mass (red full circles) and missing mass resolution (blue empty circles) versus W with (b) and without (a) momentum corrections for electrons at $Q^2 = 0.3$ GeV^2, $\theta = 82.5°$ and $\phi = 105°$.

the inner plane of the calorimeter [62]. The shape and the parameters of this function were calibrated by counting the average number of photoelectrons at different positions and angles on the EC plane over a long period of time. The connection between the number of photoelectrons and the efficiency was done using runs with only the electromagnetic calorimeter in the CLAS trigger [62].

4.3 Momentum Corrections

The trigger during the e1c running period only required coincident hits in the electromagnetic calorimeter and the Čerenkov counter, which means that any event containing an electron above thresholds is recorded. One of the advantages of this is that the elastic scattering events were recorded simultaneously with the other reactions. For the elastic kinematics the fixed value of missing mass $W = 0.938$ GeV allows us to calibrate the momentum of the electron versus ϕ_e and θ_e , so that the W-peak for elastic events is always positioned at the proton mass. These corrections are necessary because the missing mass peaks in the elastic and single π^+ production processes are reconstructed a few MeV below the proton and neutron mass (see

Fig. 4.2 a). These deviations are believed to be due to drift chamber misalignments and magnetic field uncertainties. A procedure was developed to do this calibration both for real and GSIM data, which works in the following way. In each sector of CLAS the solid angle was divided into 60 bins for $\theta_e \in [15°, 55°]$ and 90 bins for $\phi_e \in [-30°, +30°]$. For every such bin the W-distribution was fitted with a Gaussian and the relative shift in momentum needed to align the W-peak with the proton mass was calculated as:

$$\frac{\delta p}{p} = -\frac{W^2 - M_p^2}{2M_pE_b}, \tag{4.2}$$

where p is the momentum of the scattered electron, δp is the required shift in the electron momentum, W is the measured elastic peak position from the fit, M_p is the proton mass and E_b is the incident beam energy. Then, this correction was applied to the electron momentum for inelastic events.

Note, that this method relies on a correct measurement of θ_e and only corrects the momentum versus θ_e and ϕ_e of the electrons. Also it assumes that $\frac{\delta p}{p}$ is independent of W. The deviation of the missing mass peak position from the neutron mass versus W for events containing an electron and a π^+, for uncorrected (a) and corrected (b) electrons, is shown with full red circles in Fig. 4.2. The blue empty circles are the widths of the missing mass distributions. One can see a significant improvement in the alignment of the missing mass peaks with the neutron mass, after the momentum corrections are applied.

4.4 Identification of π^+

Using the information from tracking and the time-of-flight system, one can determine the mass of a charged particle. For a charged particle in a magnetic field

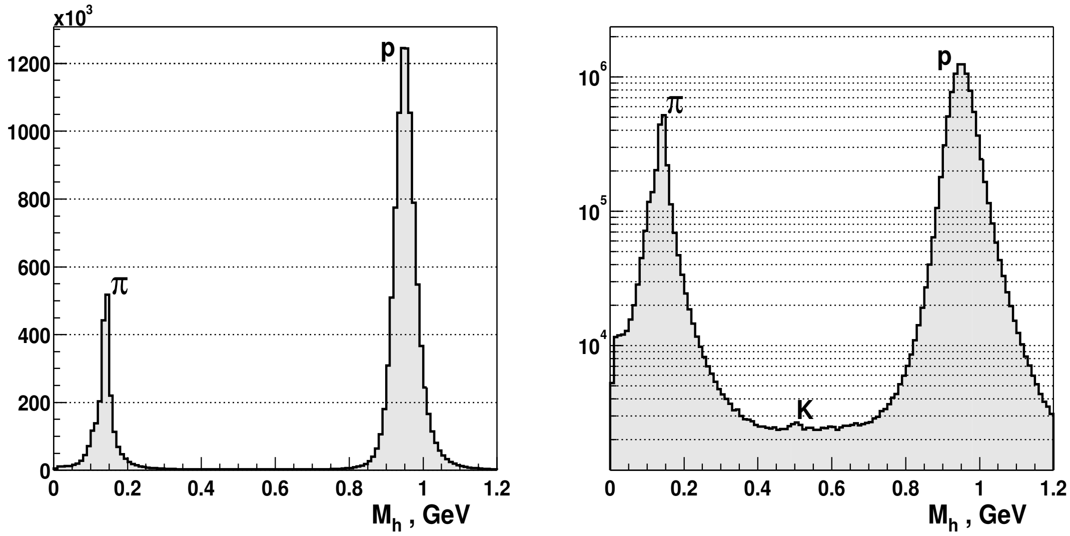

Figure 4.3: Mass spectrum for positive hadrons on linear (left) and logarithmic (right) scales. The left peak corresponds to pions[2] and the right peak corresponds to protons. A small peak at $M_h \approx 0.5$ GeV visible on the logarithmic scale is due to kaons.

one has:

$$p = \frac{m\beta}{\sqrt{1-\beta^2}} \tag{4.3}$$

$$\beta = \frac{L_{flight}}{t_{flight}}, \tag{4.4}$$

and therefore

$$m = p\sqrt{\left(\frac{t_{flight}}{L_{flight}}\right)^2 - 1}, \tag{4.5}$$

where m is the mass of the charged particle, β is its velocity, t_{flight} is the time of flight from the interaction vertex to the scintillator plane and L_{flight} is the path along the track from the vertex to the TOF counters. The mass spectrum of the positive particles from CLAS is plotted in Fig 4.3. Peaks corresponding to positive pions and protons are clearly separated.

In the off-line software the charged particle identification is done by the SEB package. It measures the distance from the point (p, β) for a given event to the

[2] The left peak also contains positrons and muons from pion decays, as shown in Fig. 3.8.

curves representing pions, kaons, protons, deuterons, and tritons. It then assigns the track the Particle Data Group (PDG) [83] number of the closest particle type. At 1.515 GeV beam energies the probability of producing a kaon is very low (see Fig. 4.3), and all the tracks that SEB identified as kaons were presumed to be pions for this analysis. In addition to the particle identification done by SEB a few more condition were imposed on the π^+ candidates. They should have passed the time-based-tracking in the DC, should have a hit in the scintillator counters, and the mass squared determined by the TOF should be less than $M_h^2 < 0.85$ GeV^2.

One of the problems in the charged particle identification is the rejection of positrons. Although pions and positrons with $P < 250$ MeV can be separated, their bands merge together at higher momenta $P > 400$ MeV [59]. For this reason all positrons were considered as pions, which, in principle, increases the background. But the missing mass and vertex cuts reduce it to a few percent level (see Fig. 4.20). This positron background should be considered as a systematic uncertainty.

Some of the channels of the time-of-flight system were dead or malfunctioning, which was manifest in the rates of pions in these counters compared with the rates in the neighboring counters. In these cases fiducial cuts were implemented to ignore the events with pion candidates in the bad scintillators. Another potential problem with the time-of-flight system was that at the backward angles the last 9 channels were actually two scintillator strips connected to a single TDC. Because the delays for these two counters were different, the time signal from these channels had two peaks, corresponding to the cases in which a particle hit one or the other strip of the pair (see Fig. 4.4). However, this does not affect the proton-pion separation because these two bands are far apart for hadrons with momentum $P_h < 1$ GeV.

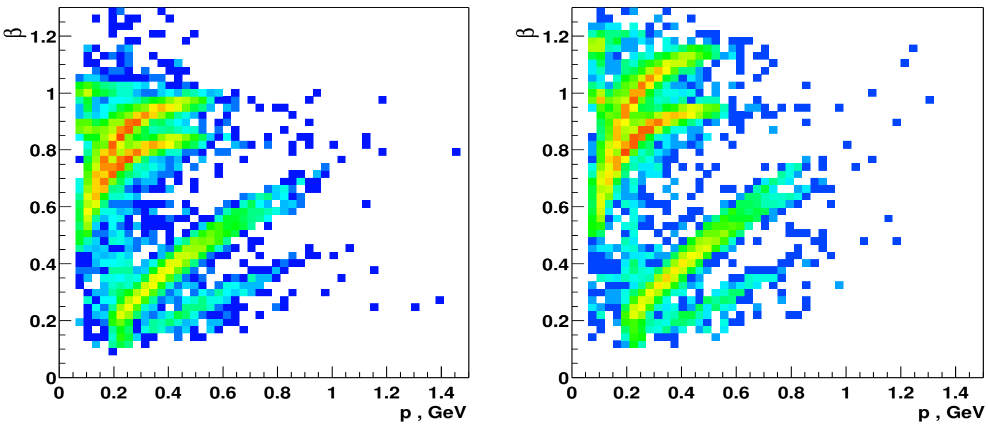

Figure 4.4: Illustration of two worst cases for counters with double bands showing counter #40 in Sector 1 (right) and Sector 2 (left). The pion bands in β versus p dependence are split in two. Nevertheless, the proton and pion bands are far apart and reliably separable.

4.5 Fiducial and Kinematic Cuts

There were two kinds of cuts in this analysis applied to both the real data and the Monte Carlo (MC) simulations. The first kind are the geometrical fiducial cuts, applied in order to select the regions of the detector which could be reliably reproduced by the GSIM simulation program. For instance, the Čherenkov counter efficiency distribution versus θ_e and ϕ_e at the edges of a sector has a very complicated pattern. Because there is no reliable way to account for these losses, fiducial cuts were developed to isolate the regions with uniform efficiency distributions. Since the toroidal magnetic field bends electrons forward, the fiducial cuts in θ_e and ϕ_e will depend on the momentum of the electron. The Čerenkov counter efficiency for electrons is shown in Fig. 4.5 as a function of electron angles θ_e and ϕ_e. The different graphs represent different bins in the electron momentum. The black curves show the fiducial cuts for the central momentum in that bin. Only events with electrons lying within these black curves were used in the analysis. In addition, a set of θ_e versus p_e cuts, shown in Fig. 4.6, were used to eliminate the areas with a depleted number of events due to bad time-of-flight counters, CC PMTs or broken wires in

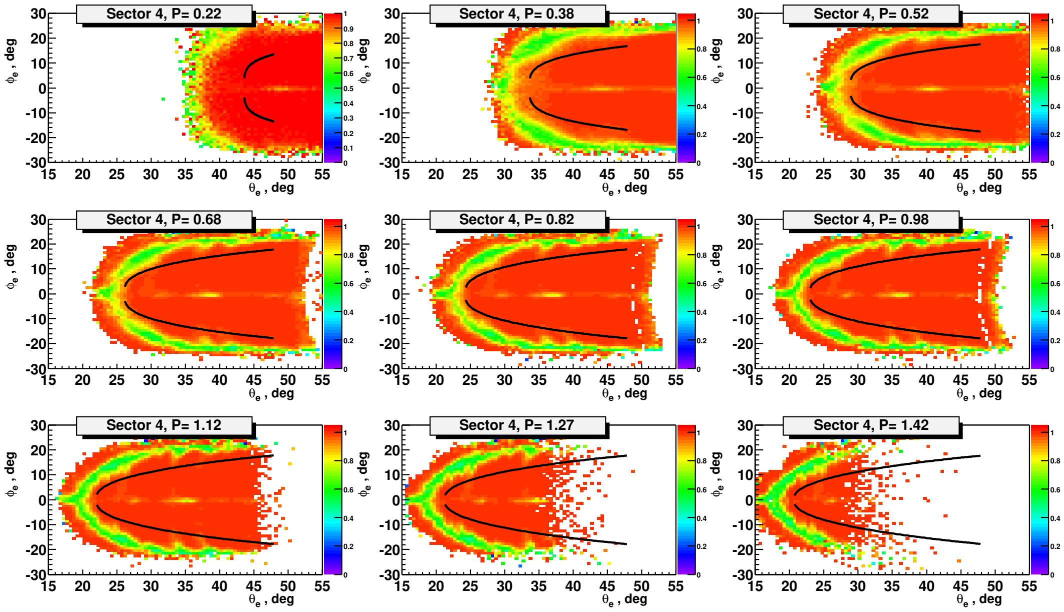

Figure 4.5: CC efficiency versus θ_e and ϕ_e for nine electron momentum bins in Sector 4. The black curves indicate the fiducial cuts for the central momentum. Only events with electrons in between the black curves were used.

DC. Events with electrons detected in the areas between pairs of curves of the same color were excluded from the analysis. Electrons with momentum $P_e < 500$ MeV were rejected as well, in order to avoid possible inefficiencies due to non-uniformity of the EC pre-trigger for deposited energies close to the EC_{total} threshold [53].

For pions two sets of fiducial cuts, shown in Fig. 4.7, were applied. The first one is a set of momentum-dependent curves selecting good regions of CLAS, where the detector response can be reliably reproduced by the detector simulation program. In addition, momentum independent cuts were applied in order to reproduce the asymmetries seen in the $\phi_{\pi^+}^{lab}$ versus $\theta_{\pi^+}^{lab}$ distributions in the laboratory frame. These asymmetries are apparently caused by deformations of the mini-torus coils not accounted for in the detector simulation program. As in the case of the electrons, the missing TOF channels and the bad DC regions were excluded from the analysis using the software cuts, illustrated in Fig. 4.8. Events with pions detected

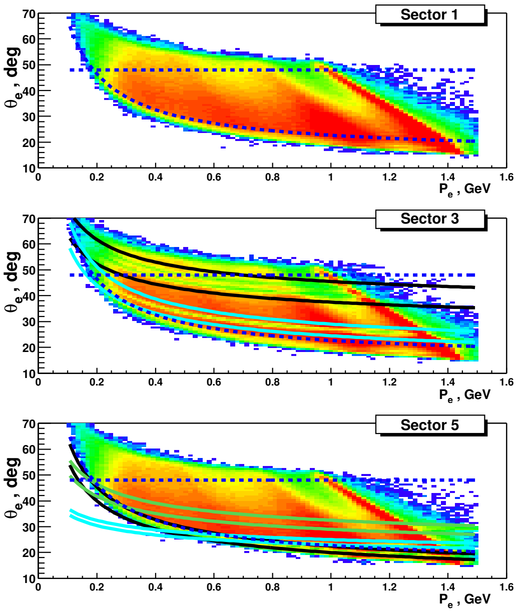

Figure 4.6: Electron angle θ_e versus momentum p_e distribution for the entire data set, including elastic events. The blue dashed curves show the minimum and maximum angles for the electron fiducial cuts. Pairs of curves of same color indicate the upper and lower edges of the cuts for rejecting electrons in bad TOF and CC counters.

between pairs of curves of the same color were not used in the analysis.

The second kind are the kinematic cuts which are imposed on the kinematic quantities characteristic to a given reaction. In our case, the primary cut is on the missing mass after detecting an electron and a pion, as shown in Fig. 4.9 a. The upper boundary of the cut must be far enough from the peak so that the knowledge of the resolution and the radiative effects has a small effect on the cross sections. On the other hand, the multi-pion background starts to contribute above the two pion threshold, thus setting the upper bound of the cut. About 20% of the single π^+ events are lost due to the missing mass cut 0.884 GeV $< M_X <$ 0.994 GeV. But, because the acceptance calculation is based on the MC event generator which has radiative losses incorporated into it, the true number of events is accounted for by the acceptance corrections. Another kinematic cut applied in the analysis is on the z-coordinate of the vertex, shown in Fig. 4.9 b. Since we are looking for an electron

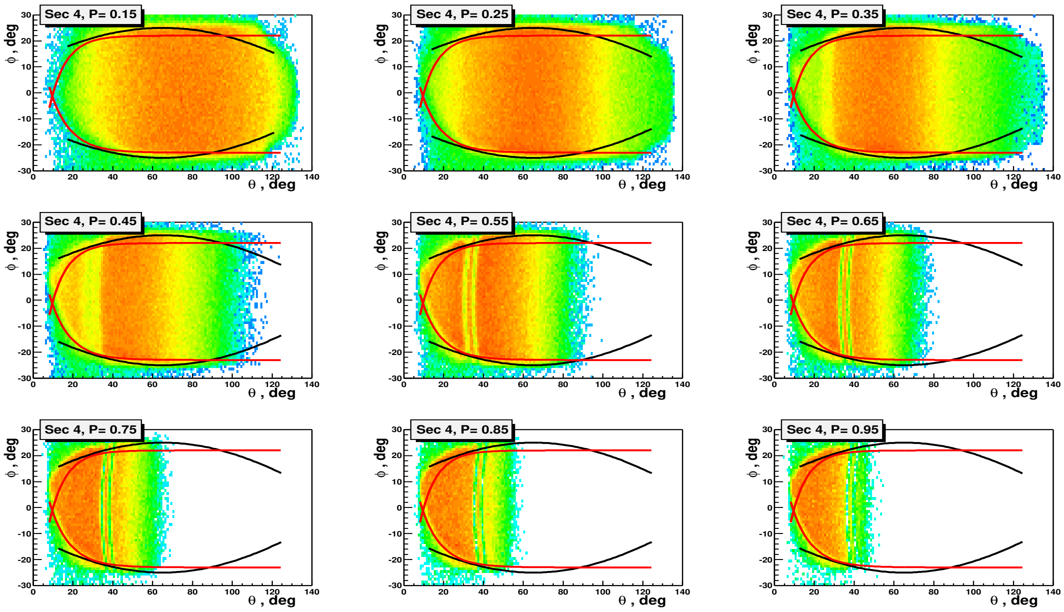

Figure 4.7: Pion ϕ_π^{lab} versus θ_π^{lab} distributions for different momentum ranges in Sector 4. The black curves are the momentum dependent fiducial cuts, while the red curves show the momentum independent cuts to eliminate the asymmetry around the $\phi_\pi^{lab} = 0$ axis. Only events between both red and black curves were used in the analysis.

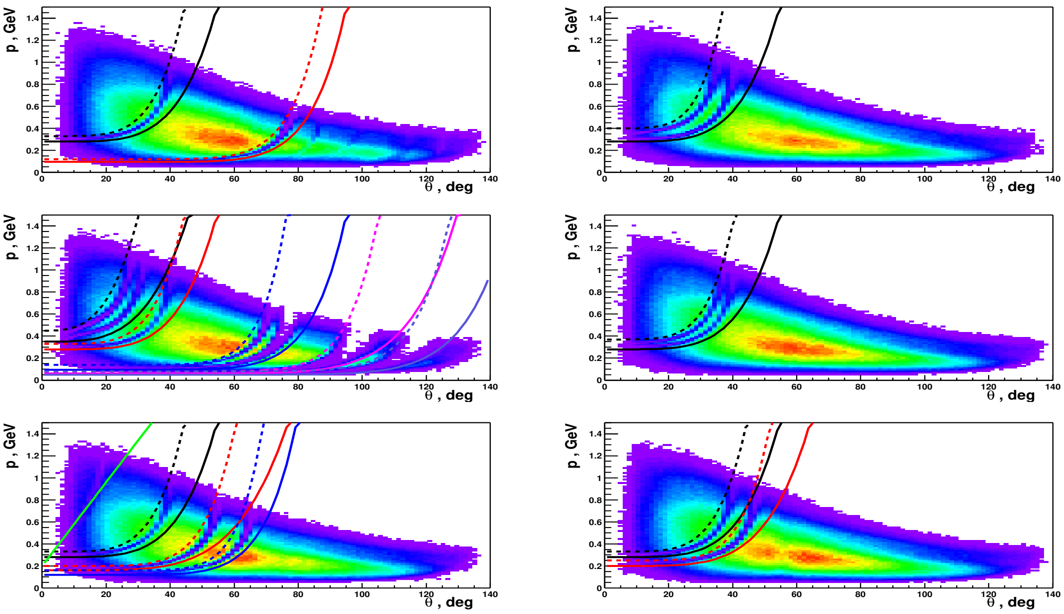

Figure 4.8: Pion p_π^{lab} versus θ_π^{lab} distributions for the six sectors of CLAS. Pairs of curves of the same color indicate the upper (dashed line) and lower (solid line) edges of cuts, developed to reject events with pions in the vicinity of the malfunctioning TOF counters.

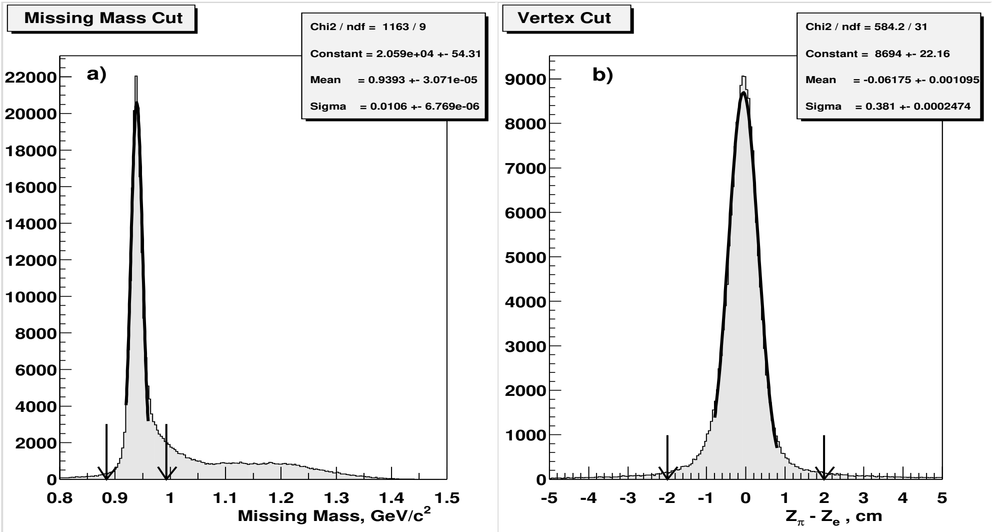

Figure 4.9: Cuts in a) Missing mass; and b) Vertex position along the beam direction. The upper and lower bounds of the cuts are represented by the arrows. In both cases the width of the cut is more than five times the resolution of the detector.

and a π^+ originating from the same vertex, a 2 cm cut was imposed on the difference between z-coordinates of the single track vertices (i.e. -2 cm $< Z_e - Z_{\pi^+} < +2$ cm) to reduce the number of decaying pions. Studies using GSIM [66] show that this reduces the number of decayed pions from 8% to 4% while reducing the number of undecayed pions by less than 1%.

4.6 Binning

For single pion electro-production at a fixed beam energy one needs to specify five independent kinematical variables to uniquely determine all other kinematical quantities. But one of these quantities can be chosen to be the electron polar angle ϕ_e in the laboratory frame. In the absence of any transverse polarization of the target or the beam, the cross section of the pion electro-production is uniform in ϕ_e, therefore averaging over 2π does not introduce any uncertainty, and only increases the statistics in the bins. The binning in the remaining 4 variables is done as shown in Table 4.2 and illustrated in Fig. 4.10.

Variable	# of bins	Lower limit	Upper limit	Width
Q^2	4	0.25 GeV^2	0.65 GeV^2	0.10 GeV^2
W	25	1.1 GeV	1.6 GeV	20 MeV
θ	12	0°	180°	15°
ϕ	12	0°	360°	30°

Table 4.2: The number and the sizes of data bins. Values for the limits indicate the upper and lower edges of the bins, rather than the bin centers.

The size of the bins was determined by the resolution of the spectrometer, the sensitivity of the physics analysis procedure to the distributions, and the available statistics. The finest binning for this reaction is required for W and θ. The fine W binning is necessary to be able to follow the phase motion in the physics analysis in order to precisely determine the resonance parameters. The fine θ binning is important in the forward region, where one needs a better sensitivity to the t-channel background behavior. Therefore, a uniform binning in θ, rather than in $\cos\theta$, is more suitable for the π^+ production channel. With the W resolution determined from the elastic peak to be about 8 MeV$-$15 MeV, the bin size of 20 MeV was chosen. The sizes of the bins in Q^2, θ and ϕ variables are chosen such that the average statistical error would be $5\% - 6\%$.

4.7 Acceptance

In order to relate the experimental yields to the cross sections, one needs to calculate the acceptance and the efficiency of the detector. Since CLAS is a very complicated detector covering almost 4π of solid angle, it is virtually impossible to separate efficiency calculations from geometrical acceptance calculations. For this reason in this analysis we refer to acceptance corrections as a combined correction factor due to the geometry of the detector and the inefficiencies of detection and reconstruction. Our definition of acceptance is the ratio of the number of recon-

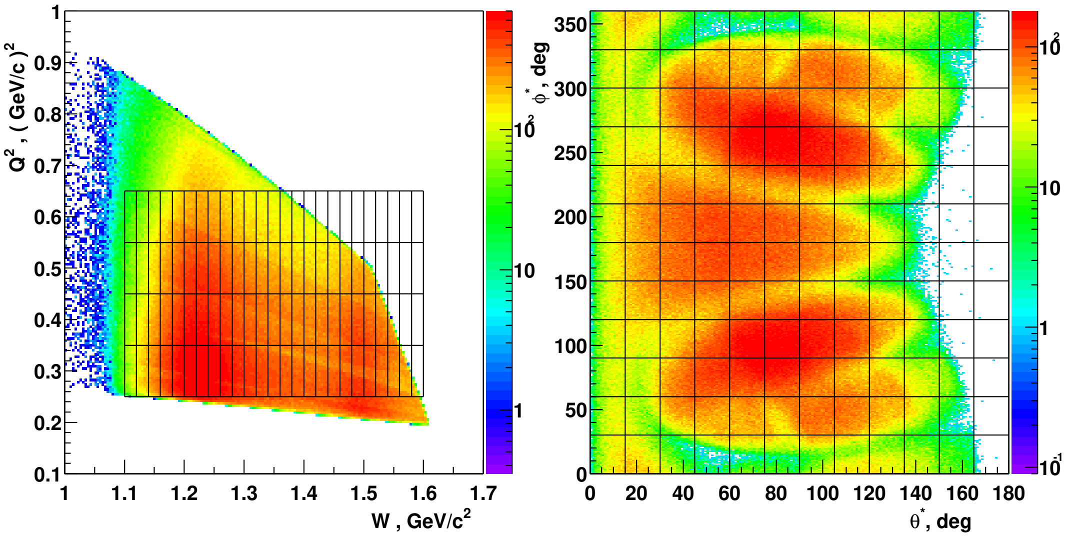

Figure 4.10: The kinematic coverage of the data and the binning, used in the analysis. The color indicates the number of events.

structed simulated events in a bin to the total number of simulated events for the same bin. Since the detector has a finite resolution it is possible that an event produced in one bin is reconstructed in a different bin, and therefore one would need a matrix to fully account for such bin migration effects. If the number of events created in the i-th bin is N_i and the number of reconstructed events in j-th bin is R_j, then:

$$R_i = \sum_j M_{ij} N_j, \tag{4.6}$$

$$N_i = \sum_j M_{ij}^{-1} R_j, \tag{4.7}$$

where M_{ij} is a large $N_{bin} \times N_{bin}$ square matrix. But in order to be able to use such a method one would also need a very large number of simulated events, which is not affordable due to the slow (1.5 event/sec) speed of the detector simulation program. In addition, the determination of the inverse of such a large square matrix is known to be a very unstable procedure. But if the event generator produces realistic distributions, then one does not need the full matrix and our definition of the acceptance as a ratio would suffice. However, the remaining model-dependence of the final results should be estimated as systematic uncertainty (see Sect. 4.11.1). It is important to note that in our method of calculating acceptance the loss of events due to the radiative tail, extending beyond the missing mass cut, is considered as an acceptance correction. Additional radiative correction are applied to the cross sections afterwards.

The acceptance corrections were applied on an event-by-event basis. Each event was weighed by a factor determined from an acceptance look-up table. This factor is defined as the ratio of number of events reconstructed in a given bin to the number of generated events:

$$A = \frac{N_{rec}}{N_{sim}}. \tag{4.8}$$

The look-up table contains $8 \times 30 \times 24 \times 48$ bins in Q^2, W, θ and ϕ, respectively, and has smaller bins than the data table. In each data bin the cross section is calculated as:

$$\sigma = \sum_{events} \frac{C}{A_{evt}} = \sum_{bin} \frac{C \cdot N_{bin}}{A_{bin}}, \tag{4.9}$$

where C is a constant for all events, A_{evt} is the acceptance factor for an event determined from the acceptance table. The second sum is over all acceptance bins which are contained in or overlap with that data bin. A_{bin} and N_{bin} are the values of the acceptance in the particular bin of the acceptance table and the number of detected events in that bin. Both the number of events in each bin and the value of the acceptance have statistical errors; therefore the relative statistical error for the cross section in each data bin can be written as:

$$\left(\frac{\delta\sigma}{\sigma}\right)^2 = \frac{\sum_{events} \frac{1}{A_{evt}^2} + \sum_{bins} \frac{N_{bin}^2 \delta A_{bin}^2}{A_{bin}^4}}{(\sum_{events} \frac{1}{A_{evt}})^2}, \tag{4.10}$$

where δA_{bin} is the statistical error for the value of the acceptance. In the trivial

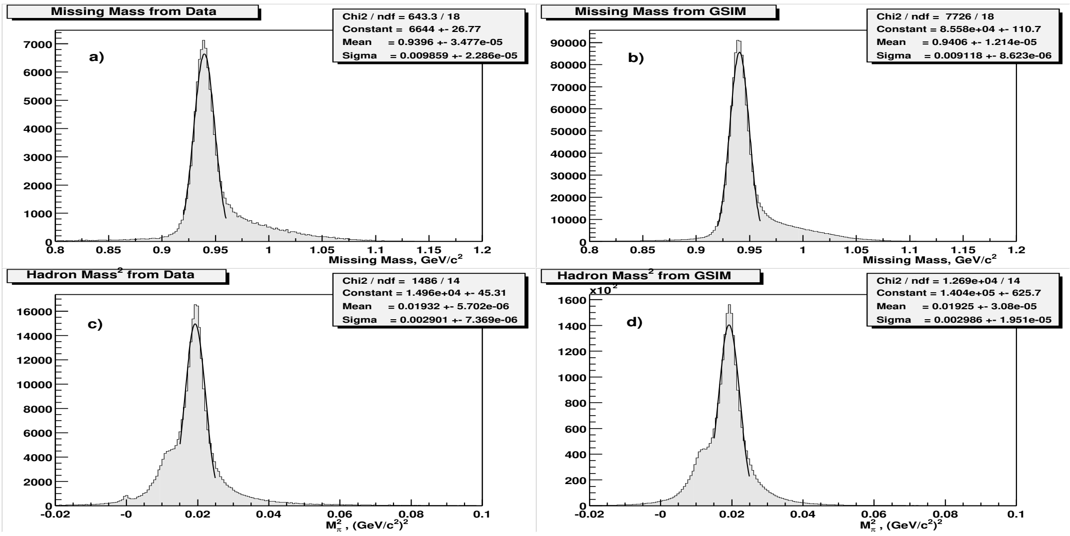

Figure 4.11: a) Missing mass distribution from the data; b) Missing mass distribution from the MC; c) Hadron mass from TOF for the data; d) Hadron mass from TOF for the MC. One can see that the GSIM data very well resembles the actual data, with the exception of the small positron peak in the hadron mass from the real data. The positrons are due to $\pi^0 \rightarrow \gamma e^+ e^-$, a process not included in the simulation.

limit of a single acceptance bin within a data bin Eq. 4.10 simply yields:

$$\left(\frac{\delta\sigma}{\sigma}\right)^2 = \frac{1}{N} + \frac{\delta A^2}{A^2}, \tag{4.11}$$

where N is the number of events in the data bin, A and δA are the acceptance and the acceptance error for that bin. In this analysis the statistical error for the acceptance δA_{bin} is determined using the formula for the binomial distribution:

$$\delta A_{bin} = \sqrt{\frac{A_{bin}(1 - A_{bin})}{N_{gen} - 1}}, \tag{4.12}$$

where N_{gen} is the number of the Monte-Carlo (MC) events generated in the bin.

In order to calculate the acceptance, approximately 200 million $ep \rightarrow e\pi^+ n$ events were generated using a MC program, based on the MAID isobar model [71] and incorporating the radiative effects [69]. The output file, containing "PART" banks from the event generator, were fed to GSIM [63] - a program which simulates the response of the CLAS detector. The Čerenkov counter response from GSIM was not used, since it has not yet been adequately modeled in the detector simulation program. Instead, a function for the Čerenkov counter efficiency, depending on the trajectory of the track, was used to correct for the CC inefficiency. The GSIM geometry was set using the straight track analysis [65] for the drift chambers and the survey geometry for the TOF system [64]. In order to eliminate signals from known dead channels, the GSIM Post Processor (GPP) program was used to remove signals from dead wires in the drift chambers and bad tubes in the scintillator counters. It also allows the user to smear the distance-of-closest-approach distribution in the DC and the TOF signals to match the missing mass distributions and hadron spectrum in the real data (see Fig. 4.11). Then the GSIM files were processed with the RECSIS program to reconstruct the simulated events. The executable of the reconstruction program was build with the same libraries which were used for processing the actual data from the e1c running period. In the final stage the output files were analyzed to produce the acceptance tables. The same cuts used on the experimental data were also applied to the simulated data to determine the acceptance. The Fig. 4.12 illustrates the analysis scheme.

Two sample graphs, representing the CLAS acceptance for the $ep \to e\pi^+n$ reaction, are shown in Fig. 4.13. Six cryostats of the CLAS detector can be clearly seen in dark blue colors. The holes due to the beam line and bad scintillator counters can be seen as well. If the virtual photon was produced in the beam direction[3], these six bands would be parallel to each other. The detector provides a wide coverage in solid angle, but the beam line and the torus cryostats create areas with low acceptance. In some cases the acceptance is actually zero, which means that we cannot reconstruct events which fall into these kinematical regions. If the area with zero acceptance covers more than 15 percent of the data bin size, that bin is dropped. Most of the losses occur in the backward direction where acceptance is low due to

[3]This would correspond to scattering angle $\theta_e = 180°$.

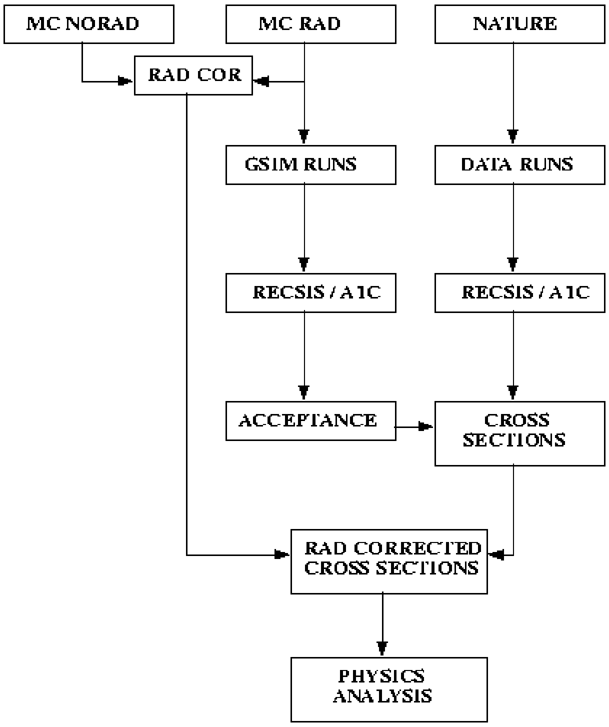

Figure 4.12: The analysis scheme. Radiative corrections are obtained using two Monte-Carlo (MC) generators with and without radiative corrections. The acceptance corrections are done using the MC generator with radiative effects. The events are processed with GSIM and the reconstruction code and then used to calculate the acceptance table.

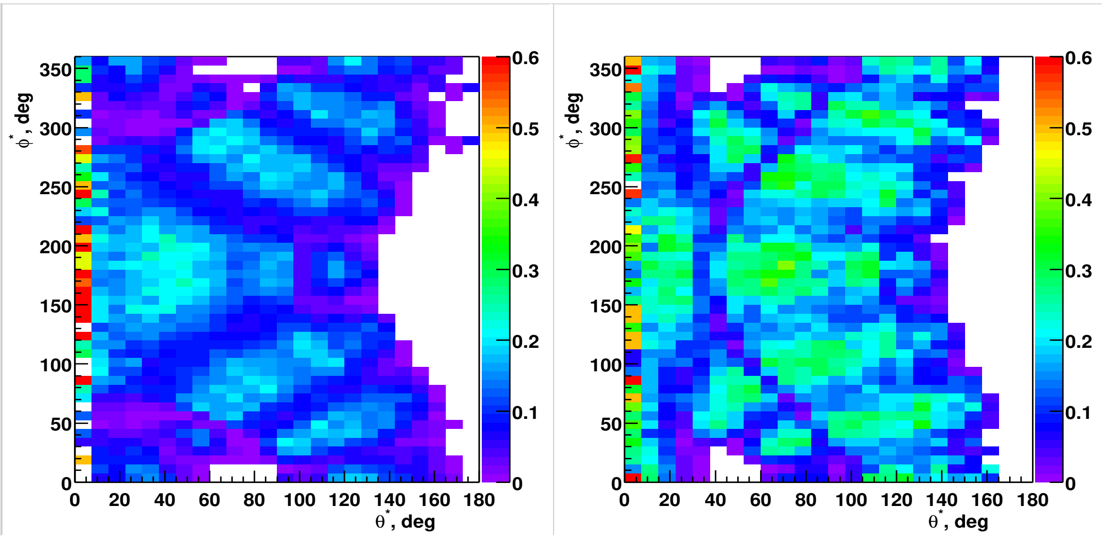

Figure 4.13: CLAS acceptance for π^+ versus CM angles θ and ϕ for $Q^2 = 0.4$ GeV^2 at $W = 1.232$ GeV (left) and $W = 1.44$ GeV (right) bins. Each plot represents a single bin in Q^2 and W. Colors show the acceptance value.

no coverage by the drift chambers beyond 140°. The white areas in the forward direction at $\phi = 0°$ and $\phi = 360°$ are due to the beam pipe.

4.8 Empty Target Cell Contributions

In order to achieve high luminosities $\approx 10^{33}$ cm^{-2}sec^{-1} during the experiment, a cryogenic liquid hydrogen target was used, because it has a higher density than hydrogen gas. The aluminum walls of the target cell can create background which has to be subtracted from the measured rates. In addition, the downstream wall of the target cell can also accumulate ice, which makes the background rate dependent on time. Therefore, it is necessary to be able to keep track of the thickness of the nuclear material around the liquid hydrogen. One way to do this is to look at deuteron events, which can only be produced on a nuclear target. The ratio of the deuteron rate in runs with a full target cell and an empty target cell allowed us to estimate how much the target cell contributed to the total counts during a particular run period.

Let us assume that the rate of pions and deuterons in the runs with the full target cell are:

$$F_{\pi^+} = H_{\pi^+} + C_{\pi^+} \tag{4.13}$$

$$F_d = C_d, \tag{4.14}$$

where H_{π^+} is the pion rate from hydrogen, C_{π^+} is the pion rate coming from the target walls, and the C_d is the deuteron rate from the cell walls. Defining quantities

$$\alpha_{full} \equiv \frac{F_d}{F_{\pi^+}}, \qquad \alpha_{empty} \equiv \frac{E_d}{E_{\pi^+}}, \tag{4.15}$$

where E_d and E_{π^+} are deuteron and pion rates from the runs with empty target, and assuming

$$\frac{E_d}{E_{\pi^+}} \approx \frac{C_d}{C_{\pi^+}}, \tag{4.16}$$

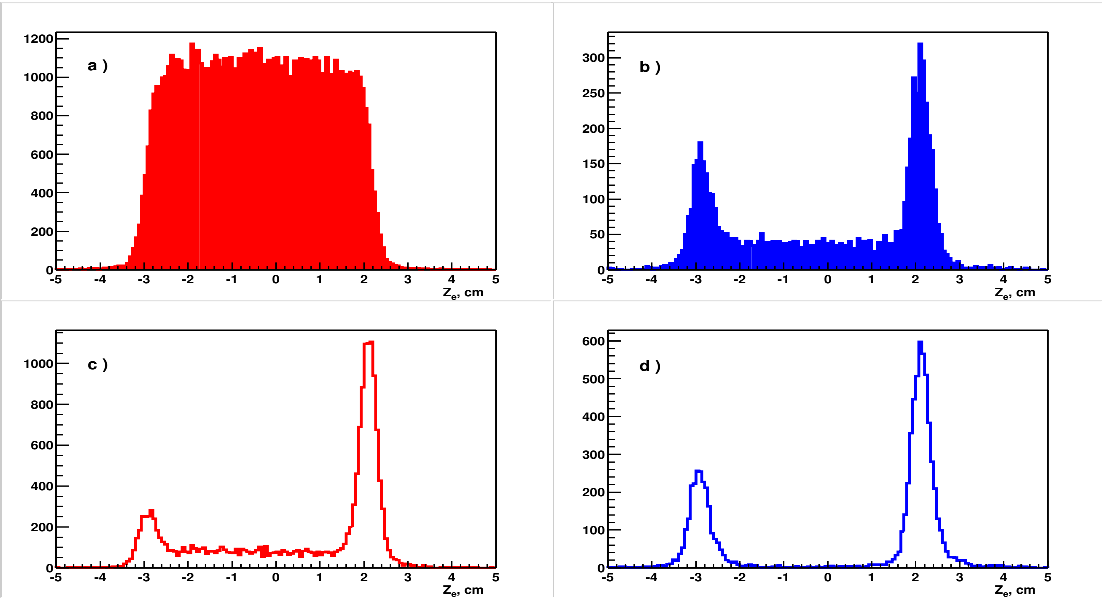

Figure 4.14: Distribution of the number of events versus z-coordinate of the electron vertex from full and empty target runs for single π^+ and deuteron events. a) - π^+ events from full target, b) - deuterons events from full target, c) - π^+ events from empty target cell, d) - deuterons events from empty target cell.

yields:

$$H_{\pi^+} \approx F_{\pi^+}(1 - \frac{\alpha_{full}}{\alpha_{empty}}). \tag{4.17}$$

The assumption in Eq. 4.16 states that almost all events in the empty target run come from the target cell walls, shown to be true for the deuteron events in Fig. 4.14 d. But about 35% of the single π^+ events in the empty target runs (see Fig. 4.14 c), comes from the remaining hydrogen gas and needs to be subtracted from E_{π^+} for Eq. 4.16 to hold. The ratio $\frac{\alpha_{full}}{\alpha_{empty}}$ determines the amount by which the measured single π^+ rate F_{π^+} should be decreased to obtain the π^+ rate only coming from the liquid hydrogen.

Figure 4.14 displays the distributions of the events from full and empty target runs. Almost all of the deuteron events, even from the full target runs, come from the entrance and exit windows of the target cell. In the analysis a 2σ cut around the center of the peaks in the electron z-vertex distributions was used for counting the deuteron rate. The background under these peaks, which contains events with protons misidentified as deuterons, was subtracted using the rate in the center of the target. The amount of empty target cell corrections for single π^+ production was found to be $1.5\% \pm 0.5\%$.

4.9 Radiative Corrections

In the electroproduction processes there is a finite probability that in the presence of the electromagnetic field of the atoms of the target the electron will emit one or more photons before or after interacting with the nucleus of the target, in this case a proton. This process is called external radiation. The probability of emitting a real photon of a particular energy is proportional to the path length of the electron in the target material and the radiative correction to the cross sections is of the form [68]:

$$\left.\frac{d\sigma}{d\Omega_e d\Omega_\pi dE'}\right|_{Meas} \Big/ \left.\frac{d\sigma}{d\Omega_e d\Omega_\pi dE'}\right|_{Born} =$$
$$\exp\left(-\{[b_w t_{iw} + \frac{1}{2}bT]\ln\left(\frac{E_1}{\Delta E}\right) + [b_w t_{fw} + \frac{1}{2}bT]\ln\left(\frac{E_3}{\Delta E}\right)\}\right), \quad (4.18)$$

where T, t_{iw}, t_{fw} are the thickness of the target, and the initial and the final windows, respectively, in units of radiation lengths. The coefficients b and b_w are numbers very close to 4/3. In this experiment the target windows contained much less material than the hydrogen inside the target, and their contributions to the radiative effects are negligible. In Eq. 4.18 $\left.\frac{d\sigma}{d\Omega_e d\Omega_\pi dE'}\right|_{Born}$ is the unradiated Born cross section.

In addition, there are radiative processes represented by Feynman diagrams similar to the original single photon exchange diagrams, but with an additional photon leg, that also contribute to the cross sections (internal radiation). In fact, it can be shown that the probability corresponding to the process of the original diagram without emitting a real photon is zero, because it is equal to the probability of emitting a photon with energy exactly $E_\gamma = 0$.

The radiative cross section for an exclusive process can be written as [67] :

$$d\sigma_r = \frac{(4\pi\alpha)^3 dQ^2 dW^2 d\Omega_h}{2(4\pi)^7 S^2 W^2} \int d\Omega_k dv \frac{v\sqrt{\lambda_W}}{f_W^2 Q^4} L_{\mu\nu}^{(r)} W_{\mu\nu}, \tag{4.19}$$

where $S \equiv 2E_i M_p$, $d\Omega_h$ is the differential solid angle of the π^+, $v \equiv M_X^2 - M_n^2$, $L_{\mu\nu}^{(r)}$ and $W_{\mu\nu}$ are the leptonic and the hadronic tensors, and

$$\lambda_W \equiv (W^2 - m_{\pi^+}^2 - M_{miss}^2)^2 - 4m_{\pi^+}^2 W^2 \tag{4.20}$$

$$\begin{aligned} f_W \equiv\ & W - E_\pi + p_\pi(\cos\theta_\pi \cos\theta_k \\ & + \sin\theta_\pi \sin\theta_k \cos(\phi_\pi - \phi_k)). \end{aligned} \tag{4.21}$$

Here, θ_π, ϕ_π, θ_k and ϕ_k are the pion and radiated photon's angles in the hadronic center of mass reference frame. The full integration in Eq. 4.19, which involves all four structure functions, has only been done recently, and has not been tested extensively.

In the present analysis a hybrid approach is adopted [69]. It incorporates the inclusive electroproduction radiative correction formalism, involving only two structure functions, and an ansatz used to model the radiative effects due to σ_{TL} and σ_{TT} terms in the exclusive electroproduction cross section formula. This involves a replacement of the integrand in Eq. 4.19 by:

$$\begin{aligned} L_{\mu\nu}^{(r)} W_{\mu\nu} \longrightarrow\ & \tilde{L}_{\mu\nu}^{(r)} W_{\mu\nu} \\ \times\ & \left(1 + \frac{\sqrt{\epsilon(1+\epsilon)/2}\cos\phi\sigma_{TL} + \epsilon\cos 2\phi\sigma_{TT}}{\sigma_T + \epsilon\sigma_L}\right), \end{aligned} \tag{4.22}$$

where $\tilde{L}_{\mu\nu}^{(r)}$ is the leptonic tensor for inclusive scattering obtained using the Mo and Tsai formalism [68].

The cross sections are corrected using a multiplicative factor for each bin. This factor is defined as:

$$\alpha_{RC} \equiv \frac{\sigma_{norad}}{\sigma_{rad}}, \tag{4.23}$$

where σ_{norad} and σ_{rad} are non-radiated and radiated cross sections, calculated using two programs AAO_NORAD and AAO_RAD, which are based on the MAID isobar model. The first one, AAO_NORAD, calculates the Born cross sections and simulates events distributed according to unradiated cross sections. The AAO_RAD program is similar to AAO_NORAD, but it also incorporates the radiative effects both due to the external radiation (or straggling) and the internal radiation coming from the Feynman diagrams with one extra photon line. Both programs create an output event file in BOS format and a summary file, containing the value of the integrated luminosity which would produce the number of generated events. Using these events and the integrated luminosity, one can calculate the cross sections and obtain the radiative correction as the ratio defined in Eq. 4.23. No missing mass cuts are applied in the radiative correction procedure, because they are already accounted for by the acceptance corrections.

Since the new code for calculating exclusive radiative corrections is expected to be tested and be better understood in the near future, the uncorrected cross sections will be made available for a future analysis involving a full integration over the photon kinematics.

4.10 Target Stability and Normalization

During the 1.5 GeV portion of the e1c running period the cryogenic target was not very stable. Periodically part of the liquid hydrogen would evaporate, leaving the liquid hydrogen level below the beam position on the target, thus decreasing the effective density of the target for the run. The automatic control system recovered the liquid phase of the target within a few seconds. But these variations of the target density with time can cause errors in the luminosity determination. For this reason, the events collected during the short time intervals, when the target density was lower than normal, were dropped from the analysis.

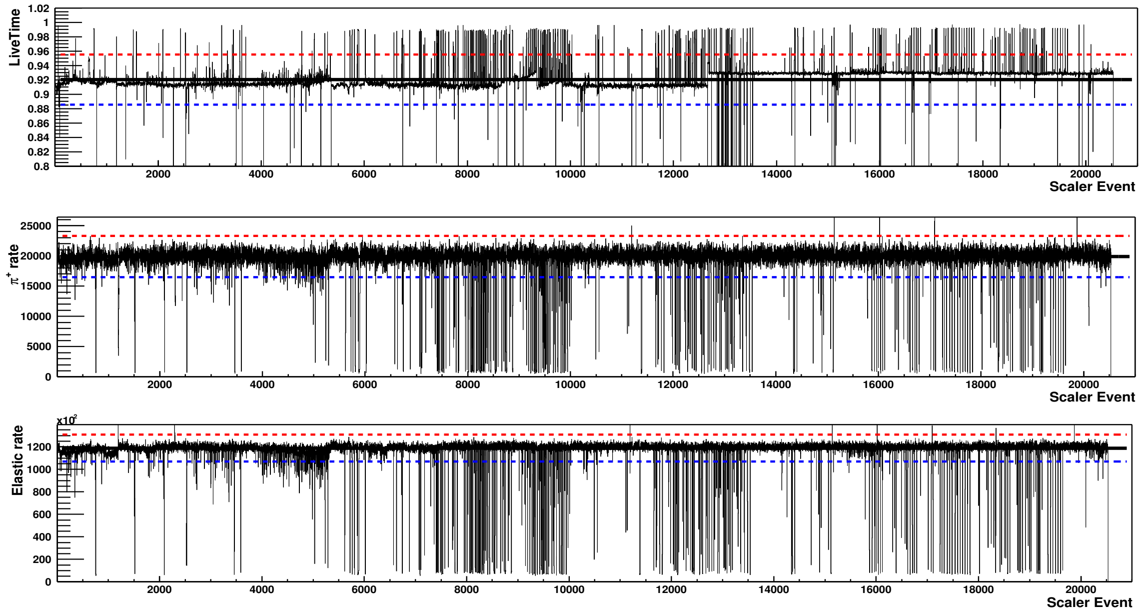

Figure 4.15: Live-time (top), the π^+ rate (middle) and the elastic rate (bottom), calculated using live-time corrected charge, versus scaler event number. The blue and red horizontal lines represent the cuts used to reject the events with unstable target densities.

There are a number of ways to diagnose the problems associated with the varying target density. One of the signatures of the target getting empty is the increase of the live-time of the data acquisition system (DAQ) above the working range of $90\% - 95\%$. Another is the dramatic decrease of the event rates normalized to the live-time corrected charge, measured in the Faraday cup. The live-time, single π^+ and the elastic scattering rates versus scaler event number are shown in Fig. 4.15. For some of the intervals between two scaler events the live-time or the event rates are outside of the imposed limits, shown by the red and blue lines. In most cases one can see correlations between such anomalies in these three plots. The events which occurred within these time intervals were ignored and the charge, corresponding to these "bad" time intervals, was subtracted from the integrated charge of the run.

To ensure that the normalization procedure was done correctly, the elastic cross section was calculated and was compared with the elastic cross sections calculated

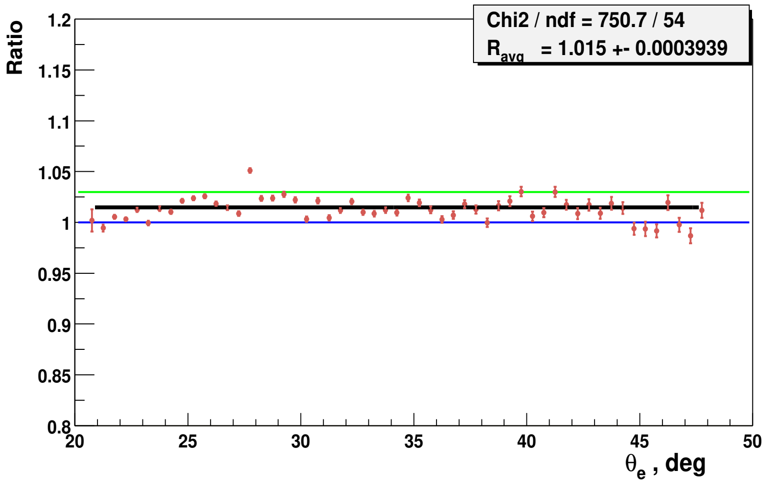

Figure 4.16: Ratio of the elastic cross section, averaged over five sectors, to the Bosted parameterization [70], plotted versus θ_e angle of the electron. The lower blue line corresponds to unity, the upper green line indicates a 3% deviation from the parameterization, and the black line is a fit of the experimental elastic cross sections to a straight line.

using the form factor parameterizations of the world data by Bosted [70]. The model cross sections were radiated using the formalism of Mo and Tsai [68]. A comparison on a sector-by-sector basis showed that the elastic cross section in Sector 2 is by $\approx 5\%$ lower than in the other five sectors. This discrepancy has not been understood yet, and therefore the events with the electron detected in Sector 2 were excluded from the analyzed data sample. Fig. 4.16 shows the comparison of the elastic cross sections averaged over the remaining five sectors with the parameterization. The single π^+ electroproduction cross sections were corrected for the 1.5% discrepancy found from this comparison.

4.11 Systematic Error Studies

4.11.1 Acceptance Errors

Because of the finite bin size, the result of averaging the acceptance over an acceptance bin depends on the distribution of events in that bin. If the physics model used in the MC simulation differs from the real data, then the averaging over a bin

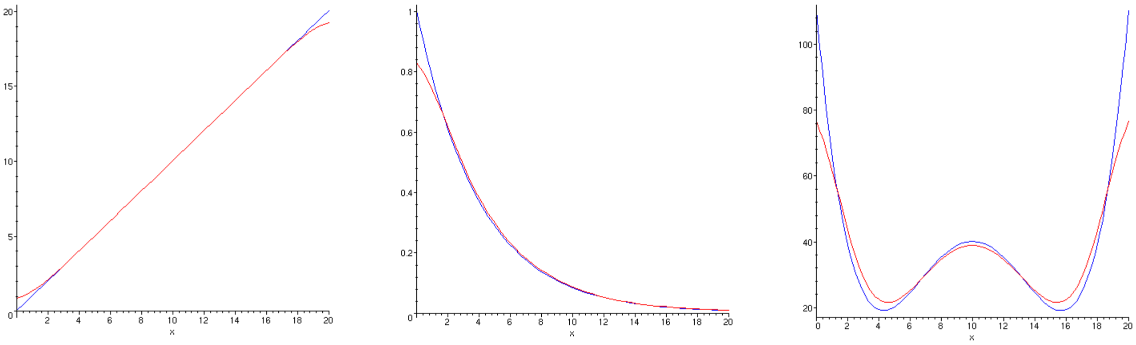

Figure 4.17: Bin migration effects for linear, exponential and “Mexican hat” distributions. The blue curves show the original distributions, and the red curves show the distorted result due to finite resolution in x, here set $\sigma_x = 1$. For linear distribution there are no distortions in the central part of the curve; only the edges are distorted. For the curves with non-zero curvature there can be distortion even away from the edges. Note that these analytical curves are equivalent to infinitely small acceptance bins.

may result in an incorrect cross section. The introduced error depends on the shape of the acceptance function and the cross sections as well as on the acceptance bin size. If the acceptance function and the cross section have very strong variation within an acceptance bin, then it becomes important to use a realistic physics model in the Monte-Carlo simulations to determine the acceptance. Reducing the acceptance bin size obviously will reduce the error associated with averaging over the bin.

Since the CLAS detector has a finite resolution, some of the events produced in one acceptance bin will be reconstructed in a different bin. It can be shown analytically that for distributions with large curvatures the resolution of the detector can cause significant distortions, as illustrated in Fig. 4.17. Even for distributions with a small curvature there is a significant effect at the edges, where events can migrate only in one direction. In order to correctly account for bin migration effects one has to have a realistic physics generator and to use the GSIM detector simulation package to reproduce the resolution of the CLAS detector. Unlike the effects from averaging over an acceptance bin, this kind of systematic uncertainty cannot be reduced by decreasing the bin size.

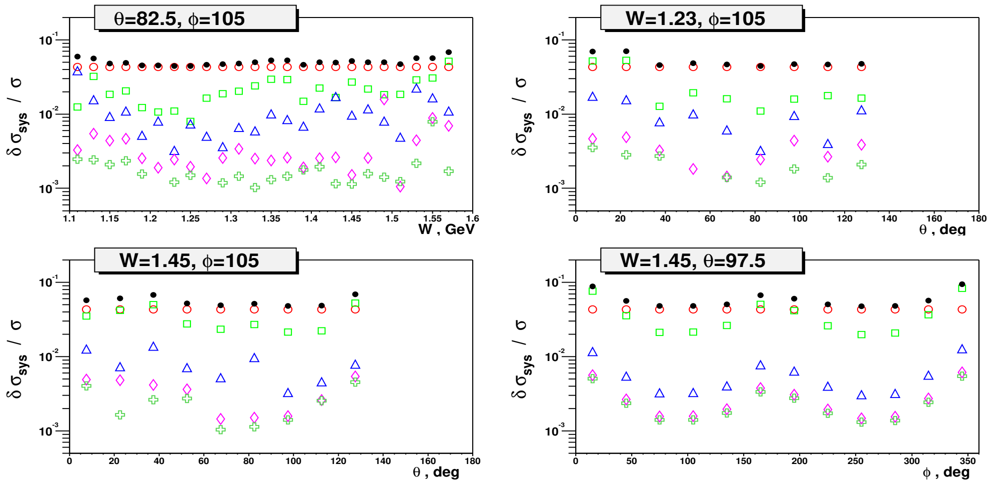

Figure 4.18: Relative systematic errors versus W, θ and ϕ. Open circles - "global" errors due to electron and pion efficiencies; open squares - due to missing mass cuts, open triangles - due to vertex cut; open diamonds - due to physics model in the acceptance calculations; open crosses - due to PID cuts. Solid circles represent the combined systematic uncertainty.

In order to estimate the errors in the final results due to the model used in the acceptance calculations, we considered two realistic isobar models: MAID2000 and MAID98 [71]. These are two versions of the same model with different unitarization procedures. However, the difference between them is comparable to the difference between the CLAS data and MAID2000. Therefore, the comparison of the results with MAID2000 acceptance corrections and MAID98 acceptance corrections allows us to estimate the systematic errors due to the acceptance model dependence (see open purple diamonds in Fig. 4.18).

4.11.2 Missing Mass Cut Errors

As was mentioned in the previous sections, we use a missing mass cut around the neutron peak to select single pion production events, which causes loss of some events. This should be accounted for by using "radiated" events in the MC simulations for the acceptance calculations, assuming the radiative processes were calculated exactly. In our MC simulation the radiative effects are calculated using the modified Mo and Tsai formalism [69], which is correct for inclusive electroproduction. For the exclusive channels this formalism is, generally speaking, not correct. The error associated with the missing mass cut was estimated by calculating the difference in the cross sections with two different missing mass cut applied both on the real data and MC data sample.

Although the standard missing mass cut used in the data is 0.884 GeV $< M_X <$ 0.994 GeV, we used two other cuts to estimate the systematic uncertainty due to the missing mass cut. One of the cuts was more narrow than the standard cut, 0.972 GeV $< M_X <$ 0.906 GeV, while the other was wider, 0.862 GeV $< M_X <$ 1.016 GeV. The absolute value of the difference between the cross sections calculated with these two cuts, averaged over ϕ at fixed Q^2, W and θ, was considered as the systematic uncertainty for all ϕ for that fixed Q^2, W and θ. As one can see from Fig. 4.18, the errors due to missing mass cuts, shown with open green squares, are about $2\% - 3\%$ of the measured cross sections.

4.11.3 Two Pion Background

In order to estimate the background coming from two pion production, a MC sample of two pion events was analyzed as if it were the actual data sample. From the resulting missing mass plot, shown in Fig. 4.19 , one can see that there is very little background in the region of missing mass $M_X < 1$ GeV, and it is on the order of 1.0% of the number of events above the pion threshold at 1.07 GeV. Because the height of the multi-pion background in the actual data sample is always much lower than the height of the neutron peak, we assign a conservative 1% global systematic uncertainty to all bins.

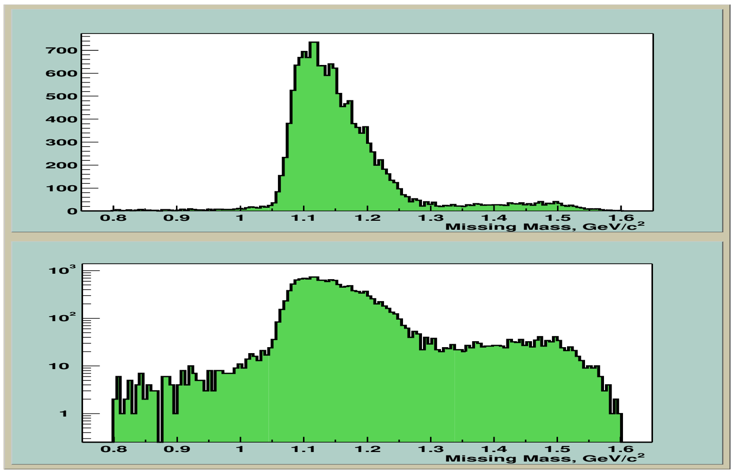

Figure 4.19: Missing mass distribution produced by two pion MC events on a linear (upper graph) and logarithmic scale (lower graph). The number of events with $M_X < 1$ GeV is less than 10% of the population above the pion threshold.

4.11.4 π^+ Identification Errors

Because all the positive tracks in this analysis are considered to be either π^+'s or protons, there may be some background from misidentified positrons. In Fig. 4.20 the mass squared of pion candidates, determined by TOF, is shown for the final data sample with all the cuts applied. In addition, a cut on the momentum $P_h <$ 0.25 GeV is applied to amplify the positron peak, because most of the positrons are created with low momentum. One can see the prominent pion peak at $M_h^2 =$ 0.019 GeV^2, and a peak near $M_h^2 = 0.01$ GeV^2 corresponding to muons from pion decays. The positron peak is located at $M_h^2 \approx 0$. The height of the positron peak is about $\approx 1\%$ of the height of the pion peak. Since for the higher momentum pions the background from positrons is significantly less, it is safe to assign a 1% global systematic uncertainty due to positrons for each data bin.

In order to see what effect the pion identification cuts can have on the cross section, a cut $M_h^2 < 0.15$ GeV^2 was applied to the GSIM events in the acceptance

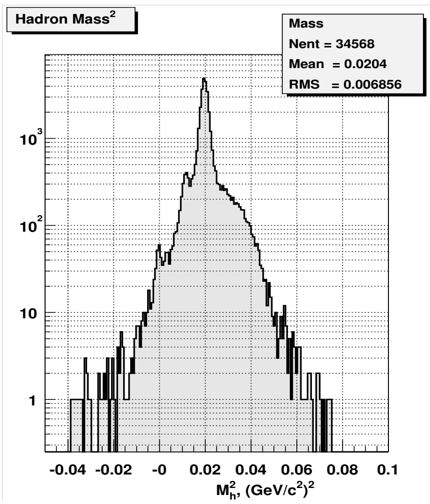

Figure 4.20: Mass squared of the pion candidates with $P < 0.25$ GeV. The selected events also satisfy the standard missing mass, vertex and fiducial cuts.

calculation while leaving the cut fixed for the real data. The difference between the resulting cross sections and the cross sections calculated with the nominal π^+ identification was under 0.5% (see open green crosses in Fig. 4.18).

4.11.5 Errors due to Normalization, e^- Identification and Electron Detection Efficiency

One of the main sources of systematic errors in this experiment is the uncertainty in the normalization. This can arise from miscalibrations of the Faraday cup, target density instabilities, and errors in determining the target length and its temperature, DAQ live-time and other factors. However, the presence of the elastic events in the data set allows us to check the normalization of the cross sections by comparing the elastic cross sections to the world data. This way we can combine the normalization, electron detection, electron tracking and electron identification errors into one global uncertainty factor. In Fig. 4.16 the ratio of the elastic cross section to the Bosted parameterization [70] of the elastic cross sections is shown.

The parameterization cross sections are also "radiated", while the elastic cross sections from the CLAS data are not corrected for radiative effects. One can see that there is an overall 1.5% offset, with all the points positioned within the upper and lower lines, indicating 3% and 0% offsets, correspondingly. This procedure allows us to assign a 3.5% global uncertainty due to the normalization, electron identification and electron efficiency.

4.11.6 Errors due to the Vertex Cut

Charged pions are not stable particles and they can decay into a $\mu\nu_\mu$ pair with 99.9% branching ratio [83]. Since the mass of muons is very close to the mass of pions, it is practically impossible to reliably separate them using the time-of-flight technique. In order to reduce the number of events with decayed pions, a ± 2 cm vertex cut was used (see Fig. 4.9 b). From the simulation it was determined that this cut would reduce the number of undecayed pions by $0.5\% - 1\%$. Although the expectation is that a GSIM based acceptance calculation will account for most of these losses, a systematic uncertainty due to differences in the vertex resolution in the simulation and the real data is still possible. In order to determine these errors the analysis was repeated with a different vertex cut of ± 4 cm. The averaged absolute value of the errors over the ϕ variable was considered as the systematic error due to the vertex cut. Typically it is on the order of 1%, as illustrated by the blue open triangles in Fig. 4.18.

4.11.7 π^+ Efficiency Errors

As for the case of the electron, the pion detection efficiency, including its decay in the detector, can be simulated by the GSIM program. Application of these acceptance corrections, which in this analysis is a combination of the geometrical acceptance and the detector efficiency, will recover the correct pion production cross

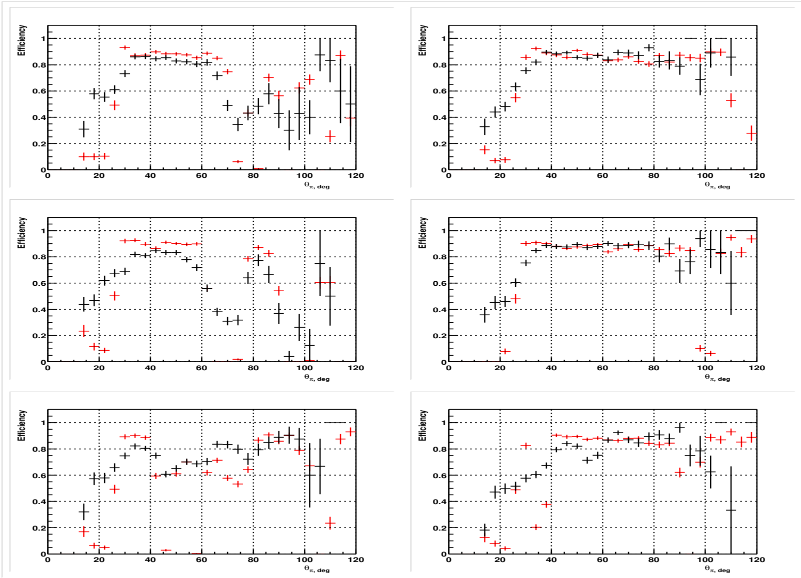

Figure 4.21: Pion efficiency from GSIM (red) and data (black) versus pion angle θ_{π}^{lab} in the laboratory frame for six sectors of CLAS. Pion momentum is in the 0.2 GeV $< P_{\pi} <$ 0.4 GeV range.

section. In order to verify that GSIM can indeed reproduce the pion efficiency, double pion production data was used to compare the π^+ efficiency from GSIM with the π^+ efficiency estimated from the actual data.

If in a process of scattering electrons off protons one detects an electron, a proton and a π^-, then from the charge conservation law one expects at least another positive particle in the final state. Using the missing mass technique one can require that the missing particle be a pion. The ratio of the number of events where the expected π^+ was detected to the number of events where a π^+ was expected, would yield the efficiency of π^+ detection and reconstruction.

As shown in Fig. 4.21, the efficiency calculated with two different methods mostly agree. By fitting the flat areas in Sectors 1, 2 and 4 to horizontal lines and calculating the average difference between the constants of the fits for the two methods, one obtains an estimate for the uncertainty due to pion efficiency modeling

e^- efficiency and normalization	global	3.5%
π^+ efficiency	global	2.5%
π^+ identification	global	0.5%
missing mass cut	local	2.0%
vertex cut	local	1.5%
acceptance	local	1.0%
two pion background	local	0.5%
Total systematic error		5.2%

Table 4.3: Summary of the averaged systematic uncertainties.

in the GSIM program, which in this analysis was found to be 2.5%. This number was used as a global systematic error.

The plots for the three other sectors have larger disagreements, because the definitions for the pion angles are different in the two methods. For pions from the two pion events from the actual data set one associates the missing momentum of $ep\pi^-$ system with the momentum of the positive pions. But for GSIM events the generated π^+ momentum is used instead. Because the missing momentum technique gives a very poor angular resolution, the presence of the large holes can affect the reconstruction efficiency for a wide area in their vicinity. For this reason only the three sectors with relatively flat efficiency dependence on the pion angle $\theta^{lab}_{\pi^+}$ were chosen to estimate the systematic uncertainty due to π^+ efficiency.

As one can see in Fig. 4.18, the largest systematic uncertainty comes from the normalization and electron efficiency, combined with the π^+ efficiency errors, shown with red open circles. Next come uncertainties due to the vertex cut and the acceptance model. The particle identification cut and the two pion background introduce negligible errors. Table 4.3 summarizes the average size of each of the systematic uncertainties. The "global" systematic errors are applied as an overall systematic error to all data bins. The "local" systematic errors are calculated for every data bin, then for fixed Q^2, W, θ averaged over the ϕ variable. The values for the “local” errors in Table 4.3 are averaged over the whole data set.

CHAPTER 5

Results

5.1 Cross Sections

The cross section of single π^+ electroproduction with unpolarized beam and target can be written [1] as:

$$\begin{aligned}\frac{\partial^5\sigma}{\partial E_f \partial\Omega_e \partial\Omega^*_\pi} &= \Gamma \cdot \frac{d\sigma}{d\Omega^*_\pi},\\ \frac{d\sigma}{d\Omega^*_\pi} &= \sigma_T + \epsilon\sigma_L + \epsilon\sigma_{TT}\cos 2\phi + \sqrt{2\epsilon(1+\epsilon)}\sigma_{TL}\cos\phi, \end{aligned} \tag{5.1}$$

where ϵ is the virtual photon polarization parameter, Γ is the virtual photon flux, and $\frac{d\sigma}{d\Omega^*_\pi}$ is the photoabsorption cross section. Since the cross section does not depend on the azimuthal angle ϕ_e of the electron in the laboratory frame, the data were binned in four variables (Q^2, W, θ, ϕ), averaging in ϕ_e over five sectors of CLAS[1]. The cross section for each bin was determined using the following formula:

$$\begin{aligned}\frac{\partial^5\sigma}{\partial E_f \partial\Omega_e \partial\Omega^*_\pi} &= \frac{1}{2\pi}\sum_{events}\frac{1}{AL\epsilon_{cc}} \cdot \frac{1}{\Delta Q^2 \Delta W \sin\theta\Delta\theta\Delta\phi} \cdot \frac{\partial(W,Q^2)}{\partial(E_f,\cos\theta_e)},\\ L &= \frac{Q_{FCUP}}{e}N_a\rho L_T,\\ \frac{\partial(W,Q^2)}{\partial(E_f,\cos\theta_e)} &= \frac{W}{2M_pE_iE_f}, \end{aligned} \tag{5.2}$$

where A is the acceptance correction factor for an event, L is the integrated luminosity, N_a is the Avogadro number, ρ is the target density, L_T is the target length, Q_{FCUP} is the integrated charge corrected for the live-time, e is the electron charge, ϵ_{cc} is the Čerenkov efficiency correction factor, ΔQ^2, ΔW, $\Delta\theta$, $\Delta\phi$ are the bin sizes,

[1] Events with an electron in Sector 2 were dropped because the measured elastic cross section in Sector 2 was lower than in the other five sectors by $\approx 5\%$.

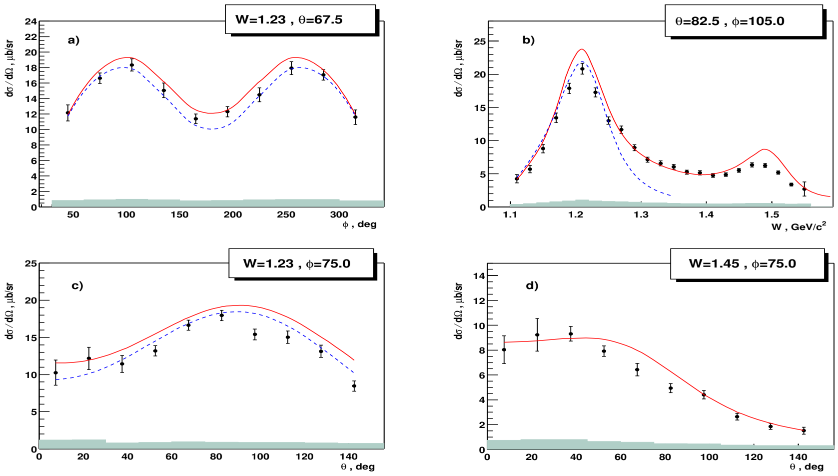

Figure 5.1: Photoabsorption cross sections $d\sigma/d\Omega^*$ at $Q^2 = 0.4$ GeV^2 from the CLAS experiment, compared to MAID2000 [71] (red solid curves) and Sato-Lee model [72] (blue dashed curves): a) ϕ dependence of the cross section at $W = 1.23$ GeV; b) W dependence at $\theta = 82.5^o$ and $\phi = 105^o$; c) and d) θ dependence at $\theta = 75^o$ and $W = 1.23$ GeV and $W = 1.45$ GeV.

$\frac{\partial(W,Q^2)}{\partial(E_f,\cos\theta_e)}$ is the Jacobian between the (W, Q^2) and $(E_f, \cos\theta_e)$ sets of variables. The values of all kinematical variables are calculated for each particular event, as opposed to being taken at the center of the bin. The statistical error for the cross sections is calculated using Eq. (4.10). Sample plots of the cross sections compared with MAID [71] and with Sato-Lee [72] models are shown in Fig. 5.1. The solid curves represent the MAID [71] model and the dashed curves are from Sato-Lee calculations [72]. The shaded area underneath shows the estimated systematic errors, while the error bars on the experimental data points are from statistical error analysis only. One can see that the data and the models globally are in reasonable agreement, but they differ significantly in detail. Due to the large number of such histograms it is more suitable to compare the structure functions from the theoretical models and this experiment, rather than the cross section histograms themselves.

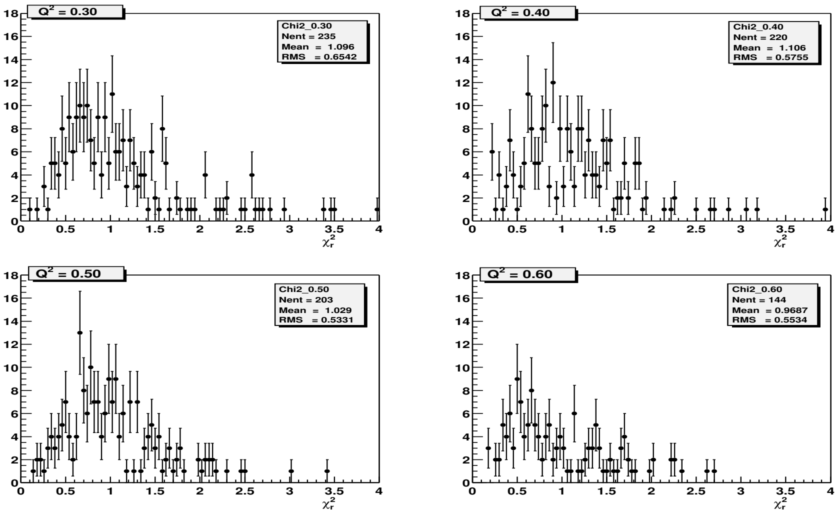

Figure 5.2: χ^2_r distributions for fits of the ϕ dependences at $Q^2 = 0.3,\ 0.4,\ 0.5,\ 0.6\ \text{GeV}^2$. The mean value of the χ^2_r distributions is approximately 1, which indicates consistency between the size of statistical errors and the spread of the data points.

5.2 Structure Functions

By fitting the ϕ-dependence of the cross sections one can separate the structure functions σ_{TT} , σ_{TL} and the linear combination of the transverse and longitudinal structure functions $\sigma_T + \epsilon\sigma_L$. Each ϕ-dependent histogram corresponding to a single Q^2, W and θ bin was fitted with a function of the form:

$$F(\phi) \quad = \quad A + B\cos 2\phi + C\cos\phi. \tag{5.3}$$

The reduced χ^2_r distributions of the fits for different values of Q^2 is shown in Fig. 5.2. Reduced χ^2_r is defined as the χ^2 per degree of freedom:

$$\chi^2_r \quad \equiv \quad \frac{\chi^2}{N_{pts} - 3}, \tag{5.4}$$

where N_{pts} is the number of non-zero points in the ϕ-dependent histogram, and 3 is the number of free parameters in the fit function in Eq. (5.3). The average value of χ^2_r is close to 1, which indicates that the statistical error bars on the cross sections are consistent with the spread of the data points. Sample plots of the structure

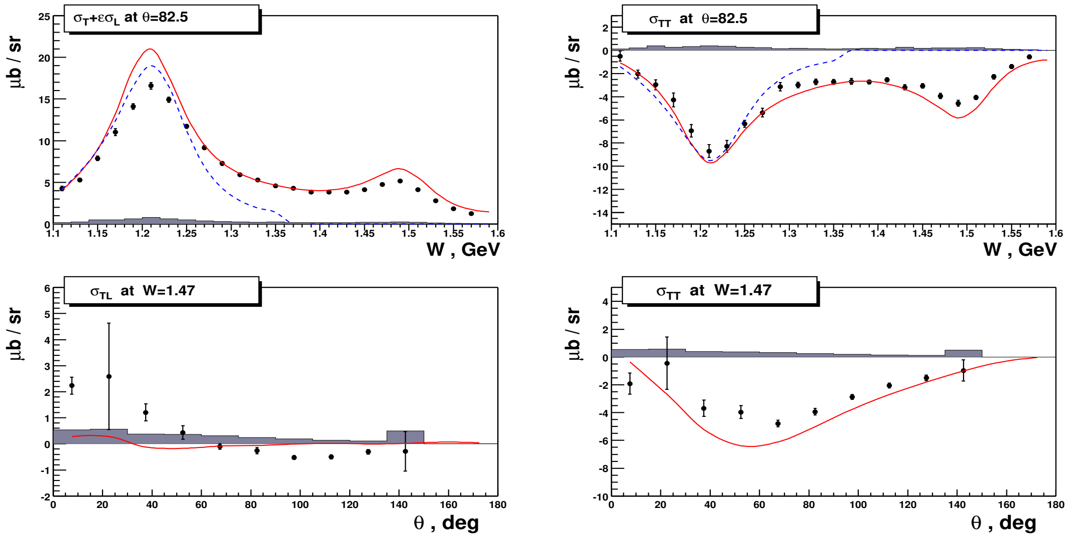

Figure 5.3: Structure functions at $Q^2 = 0.3$ GeV^2 compared with MAID [71] (red solid curve) and Sato-Lee [72] models (blue dashed curve). Shaded areas represent the estimated systematic errors.

functions versus θ and W compared with MAID [71] and Sato-Lee [72] models are shown in Fig. 5.3. The full set of the structure function plots is presented in Appendices A and B. The solid red curves show the MAID2000 predictions, while the dashed blue curves are from Sato-Lee calculations. The latter incorporates only $\Delta(1232)$ resonance, and therefore, does not describe the data above the first resonance region. The shaded areas around zero indicate the estimated systematic uncertainties for the structure functions, while the error bars on the data points represent the statistical errors only. Systematic errors for the structure functions were obtained by comparing the fit results for each bin from the data sets with different cuts described in the Chapter 4. The combined systematic uncertainty was calculated as:

$$\sigma_{comb}^{(sys)^2} = \sum_i \sigma_i^{(sys)^2}, \tag{5.5}$$

where $\sigma_i^{(sys)}$ are the deviations of the structure functions from different data sets with respect to the results obtained from the standard data set. From Fig. 5.3 one can see that the experimental $\sigma_T + \epsilon\sigma_L$ is lower than the MAID [71] and Sato-Lee [72] model predictions in the $\Delta(1232)$ resonance region. On the other hand, the σ_{TT} structure function, which incorporates only transverse helicity amplitudes, is in a better agreement with the theoretical predictions. This suggests that in these models the resonance contributions are better understood than the background terms, where most of the longitudinal contributions come from. The σ_{TL} term is the smallest term, and therefore, the relative size of the error bars are bigger than for the other two terms. One can also notice a significant difference between the data and the MAID curves for $W \in [1.41, 1.45]$ GeV for σ_{TT} and σ_{TL} terms (see Fig. 5.3 or Figs. A.2, A.3 in Appendix A). This is indicative of an incomplete understanding of the $P_{11}(1440)$ resonance excitation in the MAID calculations. Therefore, these data can be used to improve the knowledge of electroproduction amplitudes for the Roper and the other two states in the second resonance region, as well as to better constrain the background amplitudes for single π^+ electroproduction.

5.3 Fit with JANR

In order to analyze the CLAS pion electroproduction data a special fitting program "JLab Analysis of Nucleon Resonances" (JANR) was developed [78], which allows us to extract the resonance parameters by fitting the observables from the experiment. This program is based on the Mainz Unitary Isobar Model (UIM or MAID) [71] with modifications for higher energy behavior of the multipoles. The model assumes Breit-Wigner forms for the resonant multipoles:

$$D_{l\pm}(W) = d_{l\pm} f_{\gamma N} \frac{W_R \Gamma}{W_R^2 - W^2 - i W_R \Gamma_{total}} f_{\pi N} C_{\pi N}, \tag{5.6}$$

where $f_{\gamma N}$ and $f_{\pi N}$ are kinematic factors associated with the two vertices of the s-channel Feynman diagram, $C_{\pi N}$ are isospin Clebsch-Gordan coefficients, and $d_{l\pm}$ are fit parameters for each resonant amplitude. The non-resonant contributions are

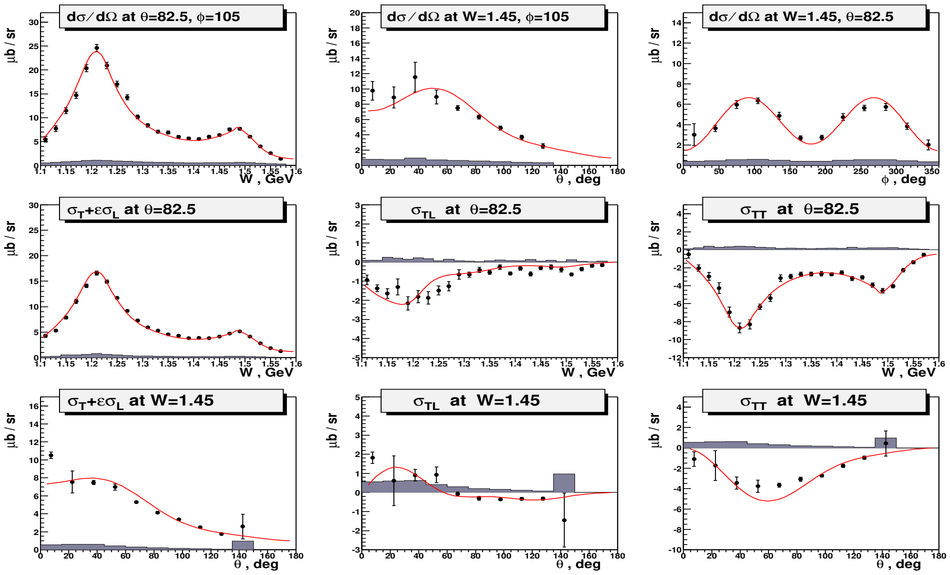

Figure 5.4: JANR fit results (red curve) compared with the experimental values of cross sections and structure functions for a few bins at $Q^2 = 0.3$ GeV^2.

calculated using an effective Lagrangian of the form:

$$L = L_{\gamma NN} + L_{\gamma\pi\pi} + L_{\pi NN} + L_{\gamma\pi V} + L_{VNN}, \tag{5.7}$$

where $L_{\gamma NN}$ and $L_{\gamma\pi\pi}$ describe the nucleon and pion electromagnetic vertices, the $L_{\pi NN}$ describes the πN interaction, $L_{\gamma\pi V}$ and L_{VNN} terms account for vector meson exchange contributions. A mixed type for πNN coupling is used in this model:

$$L_{\pi NN} = \frac{\Lambda^2}{\Lambda^2 + q^2} L^{PV}_{\pi NN} + \frac{q^2}{\Lambda^2 + q^2} L^{PS}_{\pi NN}, \tag{5.8}$$

where $L^{PV}_{\pi NN}$ and $L^{PS}_{\pi NN}$ are Lagrangian terms describing pseudo-vector and pseudo-scalar pion-nucleon interaction [71]; Λ is a scale parameter, chosen to be $\Lambda =$ 0.45 GeV; and q is the pion 3-momentum in the center of mass frame. With such a pion-nucleon interaction Lagrangian the pseudo-vector coupling $L^{PV}_{\pi NN}$ dominates at low values of pion momentum, while at higher momentum the pseudo-scalar πNN interaction starts playing a larger role. The parameters in the Lagrangian are fixed at the real photon point to agree with the VPI analysis results [82]. Only the reso-

Q^2, GeV^2	$M_{P_{11}}$, GeV	$M_{S_{11}}$, GeV	$M_{D_{13}}$, GeV
0.3	1.434 ± 0.003	1.532 ± 0.002	1.515 ± 0.002
0.4	1.421 ± 0.004	1.532 ± 0.003	1.512 ± 0.003

Table 5.1: Masses of the resonances obtained with JANR fit.

Q^2, GeV^2	$\Gamma_{P_{11}}$, GeV	$\Gamma_{S_{11}}$, GeV	$\Gamma_{D_{13}}$, GeV
0.3	0.429 ± 0.022	0.121 ± 0.006	0.112 ± 0.004
0.4	0.324 ± 0.011	1.122 ± 0.009	0.125 ± 0.006

Table 5.2: Widths of the resonances obtained with JANR fit.

nance amplitude parameters $d_{l\pm}$, their masses and their widths are allowed to vary during the fit. Their best values are found by minimizing

$$\chi^2 \equiv \sum_i \frac{({y_i}^{(exp)} - {y_i}^{(mod)})^2}{{\sigma_i}^{(exp)2}}, \tag{5.9}$$

where $y_i^{(exp)}$ and $y_i^{(mod)}$ are values for observables from the experiment and the model, respectively, and $\sigma_i^{(exp)}$ is the estimated standard deviation for the i-th experimental point.

The data from the single π^+ production experiment were fitted with JANR to obtain the resonant amplitudes for the four dominant resonances in the first and second resonance regions. The experimental data for each Q^2 bin were analyzed separately. The first two bins at $Q^2 = 0.3$ GeV^2 and $Q^2 = 0.4$ GeV^2 were fit allowing the resonant amplitudes for the states in the first and second resonant regions to vary. The masses and widths for $P_{11}(1440)$, $D_{13}(1520)$ and $S_{11}(1535)$ were allowed to float as well, and their fit values are presented in Tables 5.1 and 5.2. For the last two bins at $Q^2 = 0.5$ GeV^2 and $Q^2 = 0.6$ GeV^2 only resonant amplitudes for $\Delta(1232)$ were allowed to vary, while other parameters were fixed at their values obtained from the fit at $Q^2 = 0.4$ GeV^2. The reason for doing this is that the upper limit in the W coverage decreases as Q^2 increases (see Fig. 4.10),

State	Mass	Full Width	π Branching Ratio
$S_{11}(1535)$	1.535 GeV	0.150 GeV	0.4
$D_{13}(1520)$	1.520 GeV	0.120 GeV	0.5

Table 5.3: Masses, widths and pion branching ratios used in calculations of photon coupling amplitudes.

leaving the second resonance region outside of the acceptance for the last two Q^2 bins. The values for masses, widths and pion branching ratios for the $D_{13}(1520)$ and $S_{11}(1535)$ resonances, used to calculate the photon coupling amplitudes, are shown in Table 5.3.

The errors $\sigma_i^{(exp)}$ in Eq. 5.9 were set to be equal to the estimated statistical errors of the cross sections. The systematic uncertainty was estimated by comparing the results from fitting sets of cross sections with different cuts, similar to the procedure performed to estimate systematic errors for the cross sections and the structure functions. In addition, any discrepancy between the results from data sets with two different magnetic field settings with $I_t = 1500$ Amps and $I_t = 2250$ Amps was considered as an additional systematic uncertainty. This can overestimate the total error bars, because this discrepancy can be explained in part by statistical fluctuations.

The ratios R_{EM} and R_{SM} obtained from the fit are shown in Fig. 5.5, where the CLAS data is represented with black circles. The black portions of the error bars show the statistical errors obtained as the estimated uncertainty for the fit parameters in MINUIT [84]. The blue portions of the error bars are due to systematic uncertainties. The values for R_{EM} and R_{SM} are given in Table 5.4. The E_{1+}/M_{1+} ratio is found to be small and positive, and it shows a steep rise with Q^2. It was found [79] that the E_{1+} amplitude is much more sensitive to the details of the model used in the fitting program than the S_{1+} amplitude. The uncertainty due to the

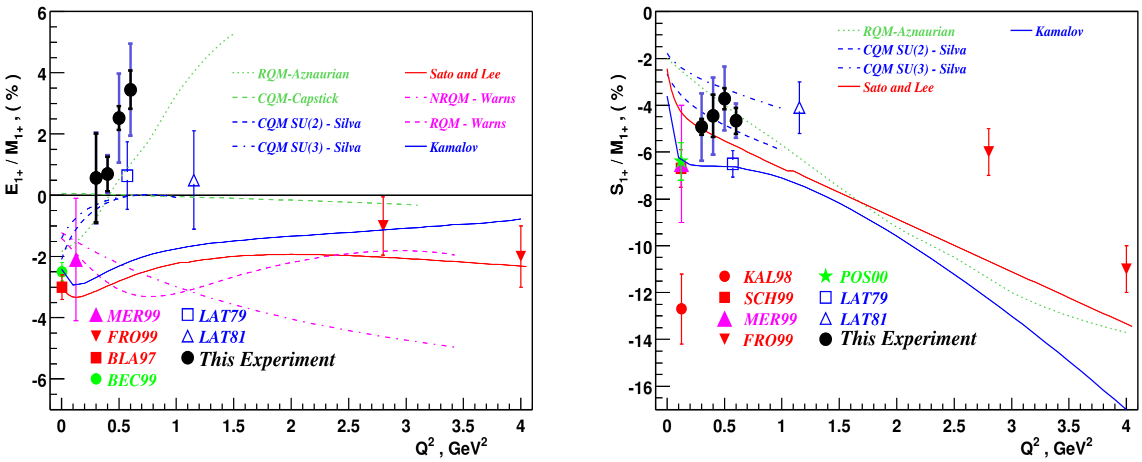

Figure 5.5: Results for R_{EM} (left) and R_{SM} (right) ratios for $P_{11}(1232)$. The curves are from [10, 36, 72, 74, 75, 77].

Q^2	R_{EM} (%)	R_{SM} (%)
0.3 GeV^2	$0.567^{\pm 0.31}_{\pm 1.45}$	$-4.930^{\pm 1.40}_{\pm 0.34}$
0.4 GeV^2	$0.695^{\pm 0.26}_{\pm 0.56}$	$-4.456^{\pm 1.38}_{\pm 0.90}$
0.5 GeV^2	$2.520^{\pm 1.40}_{\pm 0.39}$	$-3.714^{\pm 1.29}_{\pm 0.45}$
0.6 GeV^2	$3.449^{\pm 1.37}_{\pm 0.63}$	$-4.665^{\pm 0.47}_{\pm 0.56}$

Table 5.4: Results for R_{EM} and R_{SM} in percents. The systematic errors are shown as superscripts and the statistical errors are shown as subscripts.

physics model in the extraction procedure is not shown on this plot. A combined fit with the π^0 channel cross sections is necessary to extract the R_{EM} ratio more accurately. R_{SM} is negative and agrees within the error bars with most recently measured values and with predictions of many theoretical models.

The JANR fits failed to produce reasonable results for Roper multipoles. Large differences were observed between the results of the fit with single π^+ cross sections and a combined fit with the preliminary data from the beam spin asymmetry measurements at CLAS [79]. A combined analysis of π^+ and π^0 cross sections along with the single and double polarization data will help extract the Roper electroexcitation

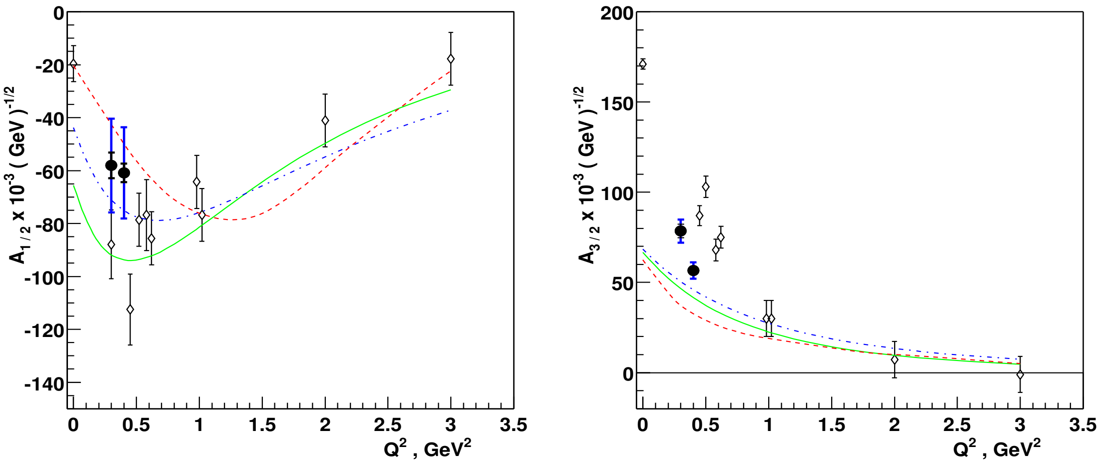

Figure 5.6: Results for $A_{1/2}$ and $A_{3/2}$ photon coupling amplitudes for $D_{13}(1520)$ shown with black circles. Black portions of the error bars represent statistical errors only. The pre-existing data are from [4, 1, 38]. Red dashed curves from [74], green solid curves from [80], dashed blue curves from [81].

multipoles in the near future.

Figure 5.6 shows our results for the $D_{13}(1520)$ amplitudes compared with the existing data. The agreement is reasonable for both $A_{1/2}$ and $A_{3/2}$. The large systematic errors for the $A_{1/2}$ amplitude are due to the discrepancy between the results from the data sets with two different magnetic field settings. Our values indicate a steeper fall-off for the $A_{3/2}$ amplitude at $Q^2 < 1$ GeV^2 than previously measured [1]. We also observe a possible transition from a negative value $A1^{sys}_{stat} = -0.292^{\pm 0.28}_{\pm 0.089}$ at $Q^2 = 0.3$ GeV^2 to a positive value $A1^{sys}_{stat} = +0.072^{\pm 0.28}_{\pm 0.074}$ at $Q^2 = 0.4$ GeV^2 for the transverse photon asymmetry A_1, shown in Fig. 5.7. Both of these points are consistent with zero at 1σ confidence level. The values for the photon coupling amplitudes are presented in Table 5.5.

Even though η production is the cleanest channel for studying the excitation of the $S_{11}(1535)$ resonance, it is very useful to extract the $A_{1/2}$ independently from the pion electroproduction data. The values obtained for the $A_{1/2}$ amplitude are shown by black solid circles in Fig. 5.8 and are given in Table 5.5. The full error

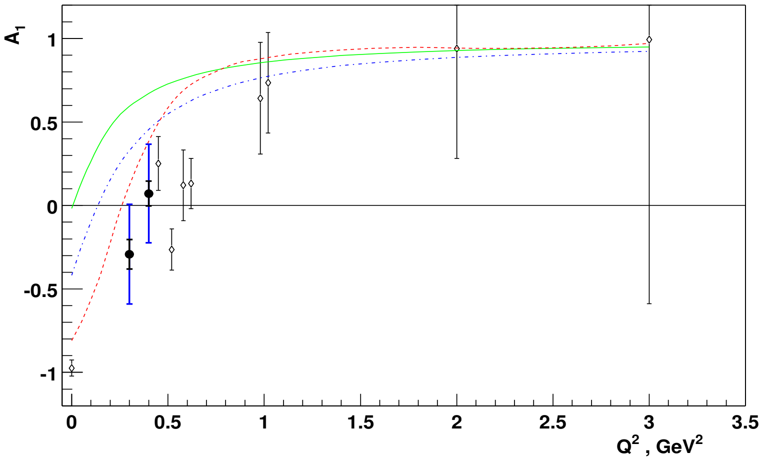

Figure 5.7: Results for A_1 asymmetry for $D_{13}(1520)$. CLAS points shown with black circles. Black portions of the error bars represent statistical errors only. The pre-existing data are from [4, 1, 38]. Red dashed curves from [74], green solid curves from [80], dashed blue curves from [81].

Q^2	$A_{1/2}$ for $D_{13}(1520)$	$A_{3/2}$ for $D_{13}(1520)$	$A_{1/2}$ for $S_{11}(1535)$
0.3 GeV^2	$-58.085^{\pm 17.1}_{\pm 4.8}$	$78.473^{\pm 5.2}_{\pm 3.7}$	$104.703^{\pm 6.5}_{\pm 2.4}$
0.4 GeV^2	$-60.837^{\pm 16.9}_{\pm 3.5}$	$56.624^{\pm 3.8}_{\pm 2.4}$	$110.997^{\pm 7.5}_{\pm 2.2}$

Table 5.5: Results for photocoupling amplitudes for $D_{13}(1520)$ and $S_{11}(1535)$ in $10^{-3}\times$GeV^{-2} units. The systematic errors are shown as superscripts and the statistical errors are shown as subscripts.

bars in Fig. 5.8 represent statistical and systematic errors combined in quadrature. Our result is by $\approx 2\sigma$ higher than the recent η production result from CLAS [45]. The disagreement may be due to uncertainty in the pion and η decay branching ratios of the $S_{11}(1535)$: the Particle Data Group values [83] are $\Gamma_\pi/\Gamma = 35\% - 55\%$, and $\Gamma_\eta/\Gamma = 30\% - 55\%$. The analysis programs used to extract the amplitude from these experiments are different, and the disagreement may also be due to the model-dependence of the extraction procedures. The error bars for both of these data sets do not include the uncertainties associated with selecting a particular physics analysis model. The world data set is best described by the hypercentral quark model [80], represented with the black solid curve.

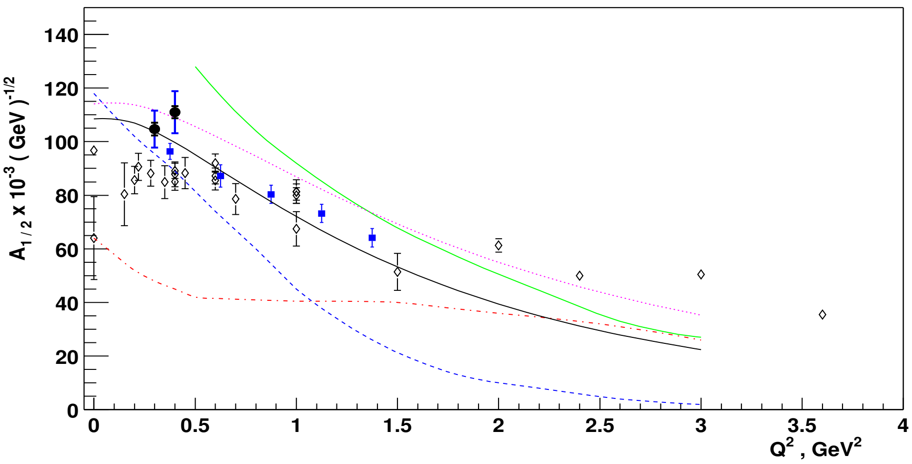

Figure 5.8: Results for $A_{1/2}$ photon coupling amplitudes for $S_{11}(1535)$ shown with black circles. The black portions of the error bars represent statistical errors only. Green solid line is [34], blue dashed line is [74], red dash-dotted line is [39], black solid line is [80], pink dotted line is [81]. The pre-existing data are from [40, 41, 42, 43, 44] .

5.4 Summary

The experiment described in this thesis is the first measurement of single π^+ electroproduction cross sections in the resonance region with a nearly complete angular coverage in the center-of-mass frame. In this analysis the cross sections were extracted at four points in the range 0.25 GeV^2 $< Q^2 <$ 0.65 GeV^2 and for W between 1.1 GeV and 1.6 GeV. The size of combined statistical and systematic error bars for the cross sections, averaged over $\approx$ 8600 data bins, is under 10%. The structure functions σ_{TL}, σ_{TT} and the linear combination $\sigma_T + \epsilon\sigma_L$ were obtained by fitting the ϕ-dependence of the cross sections. Comparisons with the MAID and Sato-Lee models in the $\Delta(1232)$ region indicate that the dominant M_{1+} resonant amplitude is well known, while the background terms for π^+ electroproduction are less understood. In the region of the $P_{11}(1440)$ resonance considerable disagreements were found between MAID predictions and the experimental values for the interference structure functions.

An isobar fit was performed using the newly developed JANR program using single π^+ electroproduction cross sections only. The value for R_{SM} obtained for $\Delta(1232)$ is small and negative, in agreement with the π^0 data analysis. The R_{EM} ratio is small and positive, but is very-model dependent [79]. A combined fit with π^0 data is necessary to reliably determine the R_{EM} and R_{SM} for the $\Delta(1232)$.

The values obtained for the $A_{1/2}$ and $A_{3/2}$ photon coupling amplitudes for the $D_{13}(1520)$ resonance are in reasonable agreement with the existing data. The transverse photon asymmetry A_1 appears to change its sign somewhere in-between $Q^2 = 0.3$ GeV^2 and $Q^2 = 0.4$ GeV^2 values of the momentum transfer.

The $A_{1/2}$ amplitude for $S_{11}(1535)$ from single π^+ electroproduction data is in 2σ disagreement with the latest result from the η electroproduction analysis at CLAS, possibly due to uncertainty in the knowledge of the decay branching ratios.

The results for the resonance amplitudes obtained in this thesis were based on the single π^+ electroproduction cross sections only. Even though the experimental systematic uncertainties were estimated, the final results for resonant amplitudes are likely to have sizable uncertainties due to the model used in the extraction procedure. However, these uncertainties are expected to be significantly smaller than those of many previous analyses based on data sets with limited kinematic coverage. Clearly, one needs more experimental observables, such as cross sections from different decay channels or polarization observables, to have more constraints on the fit.

The main result of this work is the single π^+ electroproduction cross section covering nearly full angular range in the hadronic rest frame in the first and second resonance regions. The future analyses of these data along with single π^0 electroproduction cross sections will allow us to determine the R_{EM} and R_{SM} ratios for $\Delta(1232)$, while a combined fit with the beam and beam-target asymmetry data will improve our knowledge of the resonant amplitudes for the excited states in the second resonance region.

APPENDIX A

Dependence of the Structure Functions on θ

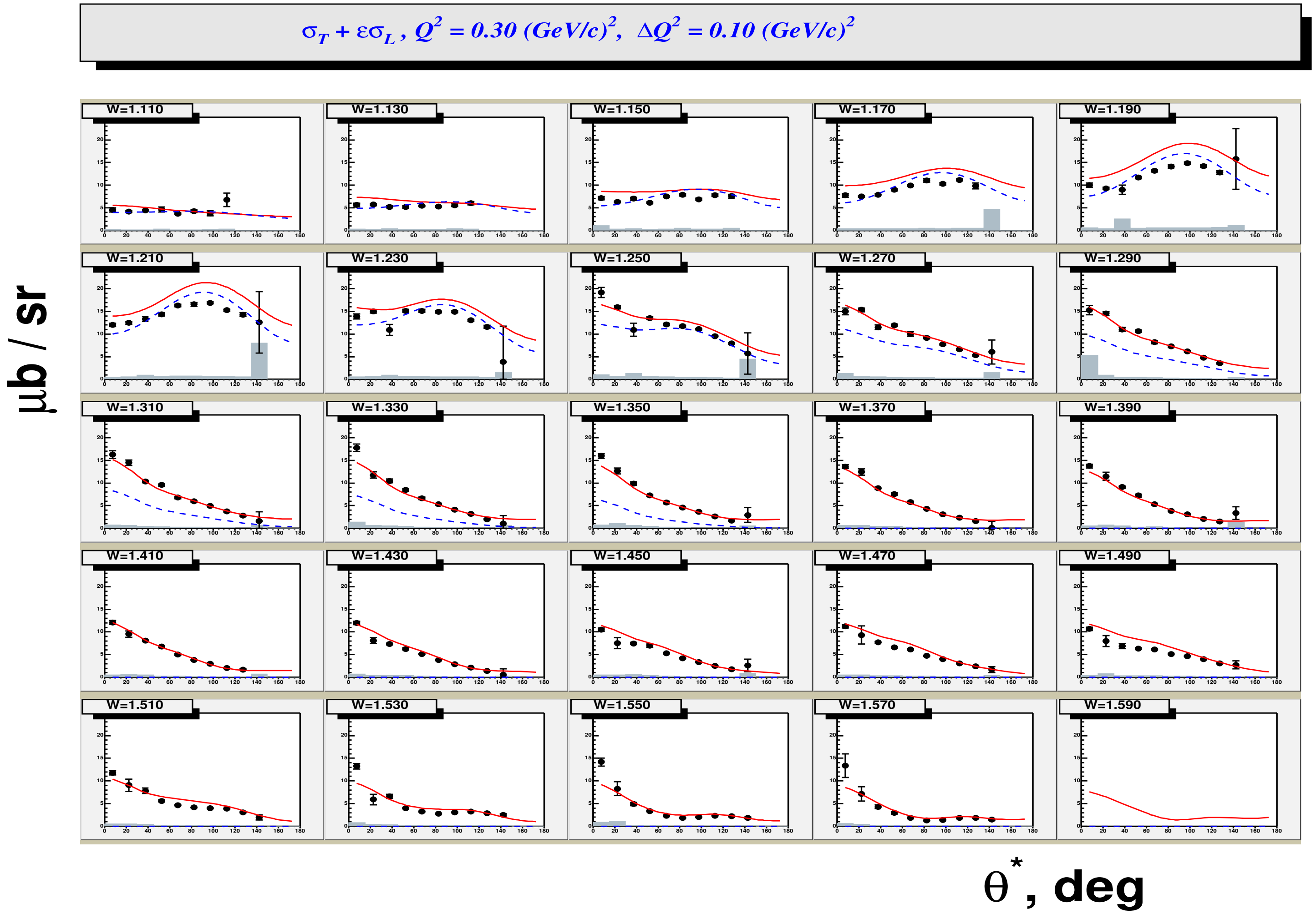

Figure A.1: Dependence of $\sigma_T + \epsilon\sigma_L$ on θ at $Q^2 = 0.3$ GeV^2. Red solid curve represents MAID-2000 calculations, while the blue dashed curve shows the predictions of the Sato-Lee model. Shaded areas represent the systematic uncertainties.

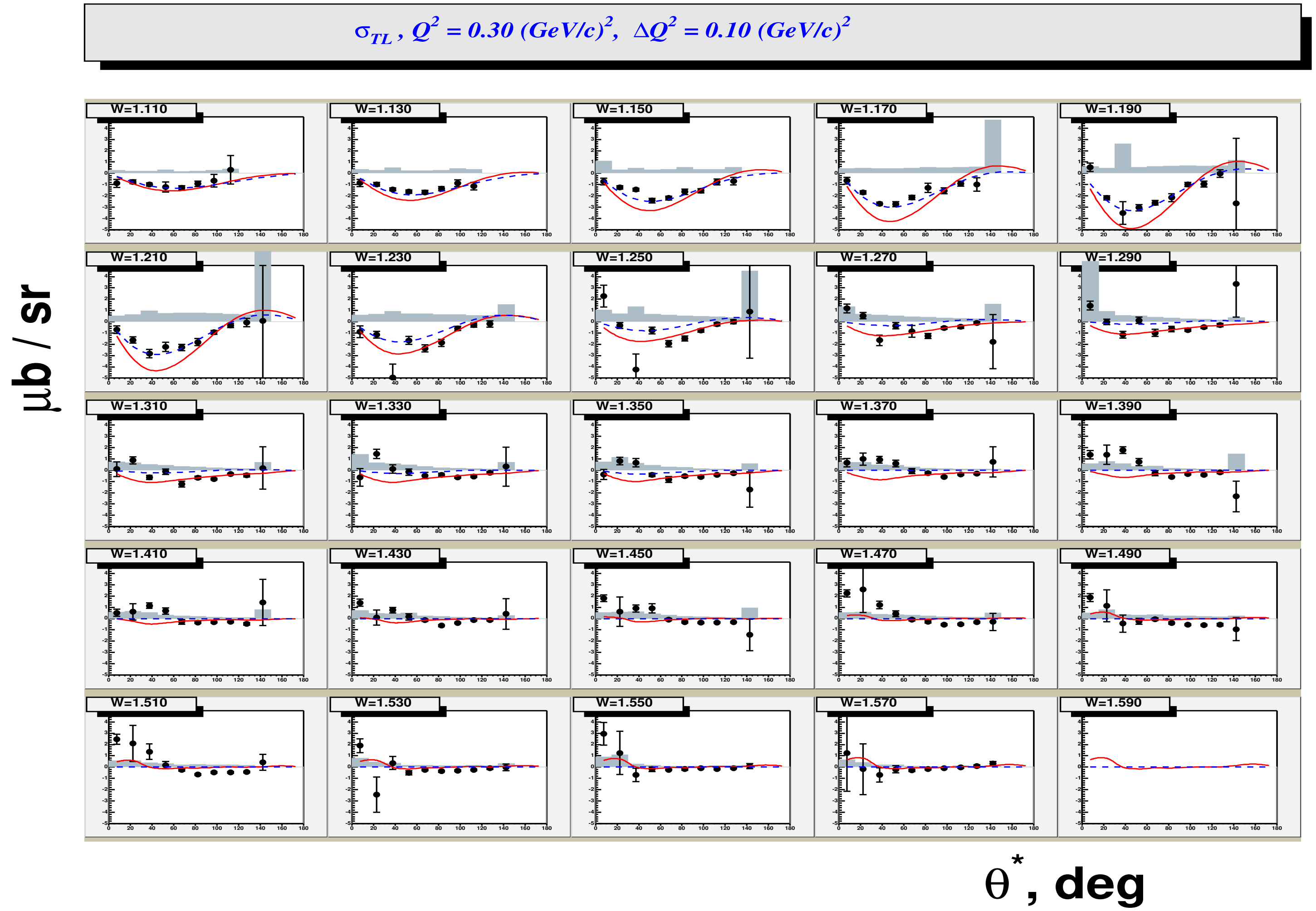

Figure A.2: Dependence of σ_{TL} on θ at $Q^2 = 0.3$ GeV^2. Red solid curve represents MAID-2000 calculations, while the blue dashed curve shows the predictions of the Sato-Lee model. Shaded areas represent the systematic uncertainties.

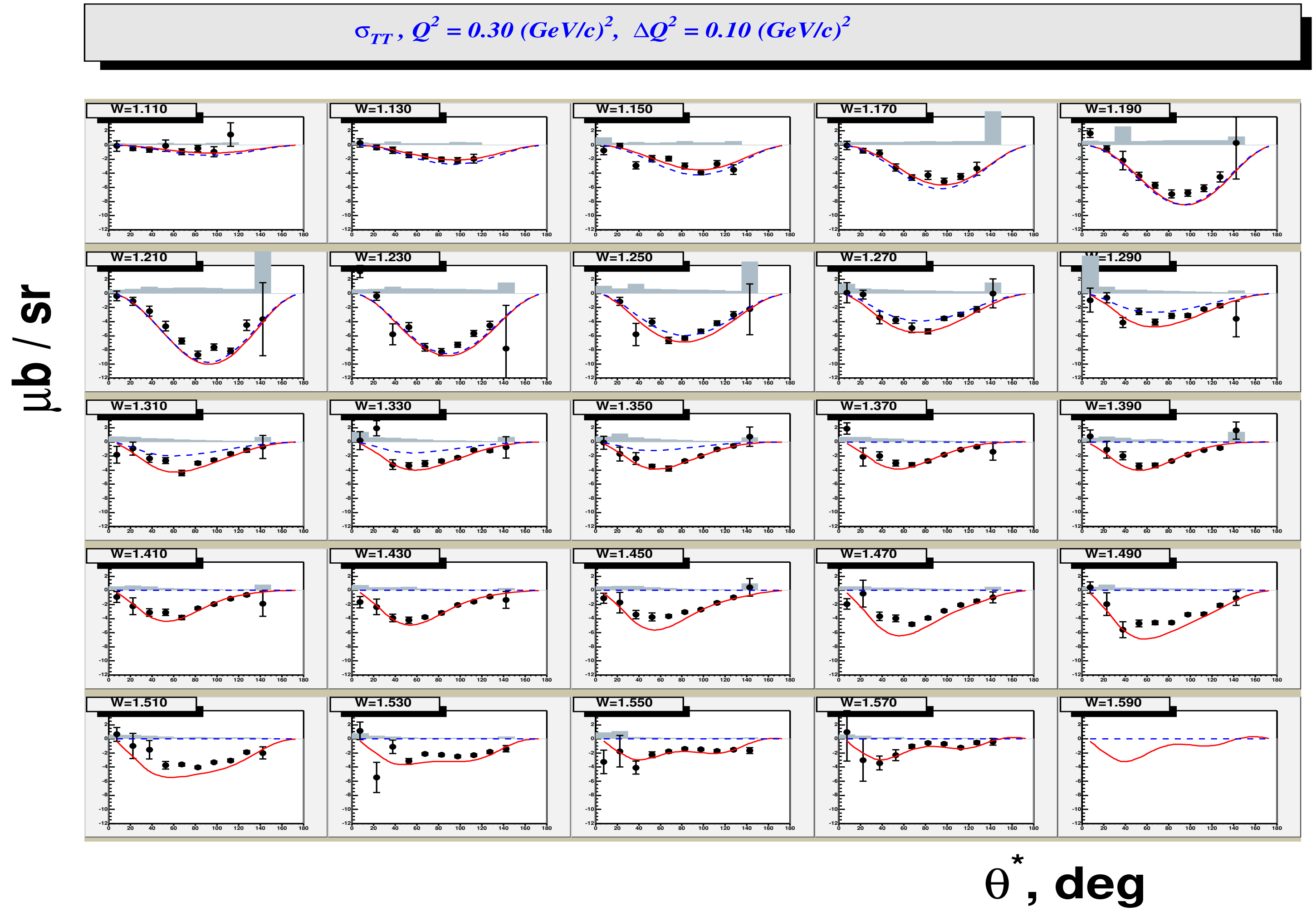

Figure A.3: Dependence of σ_{TT} on θ at $Q^2 = 0.3$ GeV^2. Red solid curve represents MAID-2000 calculations, while the blue dashed curve shows the predictions of the Sato-Lee model. Shaded areas represent the systematic uncertainties.

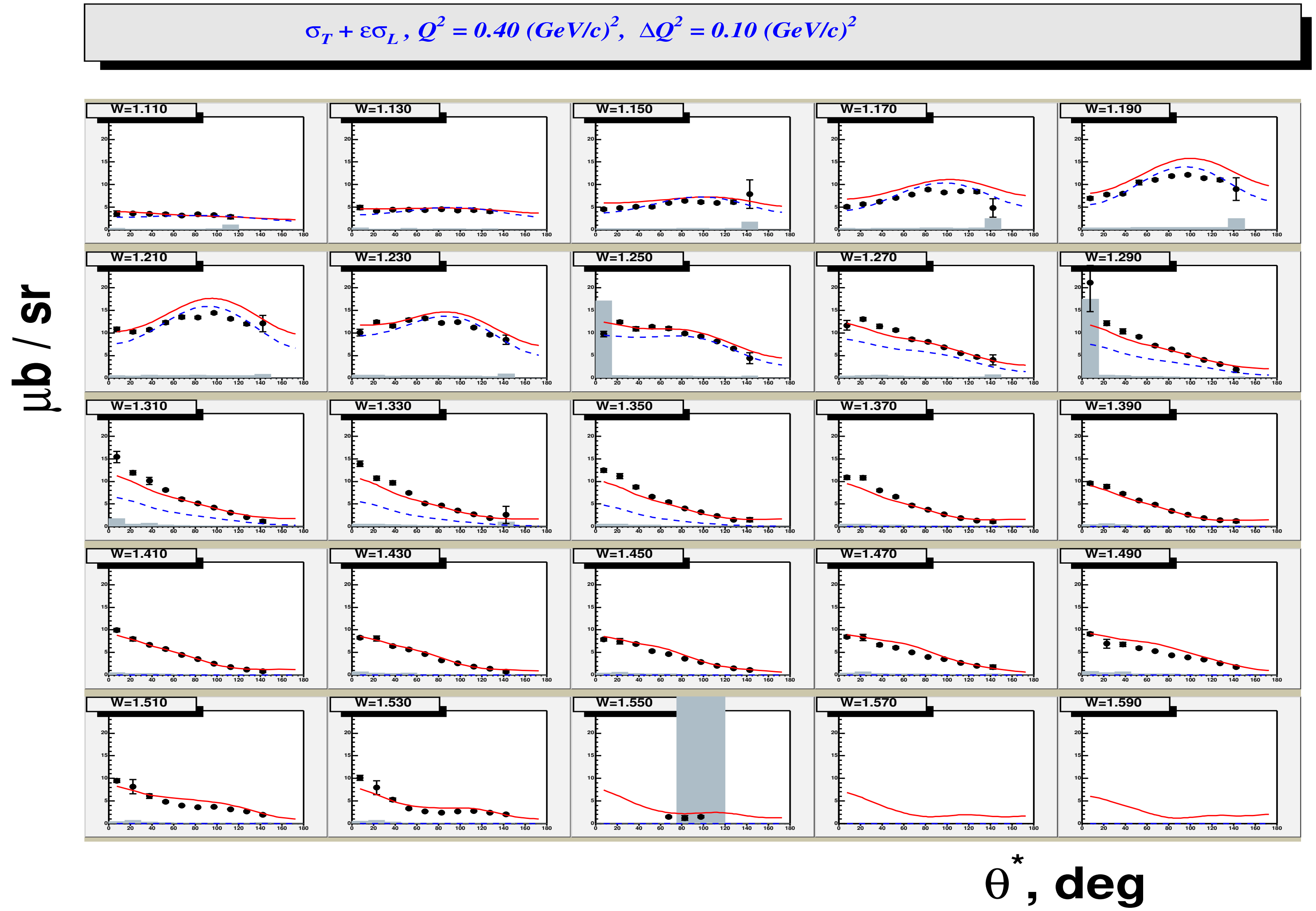

Figure A.4: Dependence of $\sigma_T + \epsilon\sigma_L$ on θ at $Q^2 = 0.4$ GeV^2. Red solid curve represents MAID-2000 calculations, while the blue dashed curve shows the predictions of the Sato-Lee model. Shaded areas represent the systematic uncertainties.

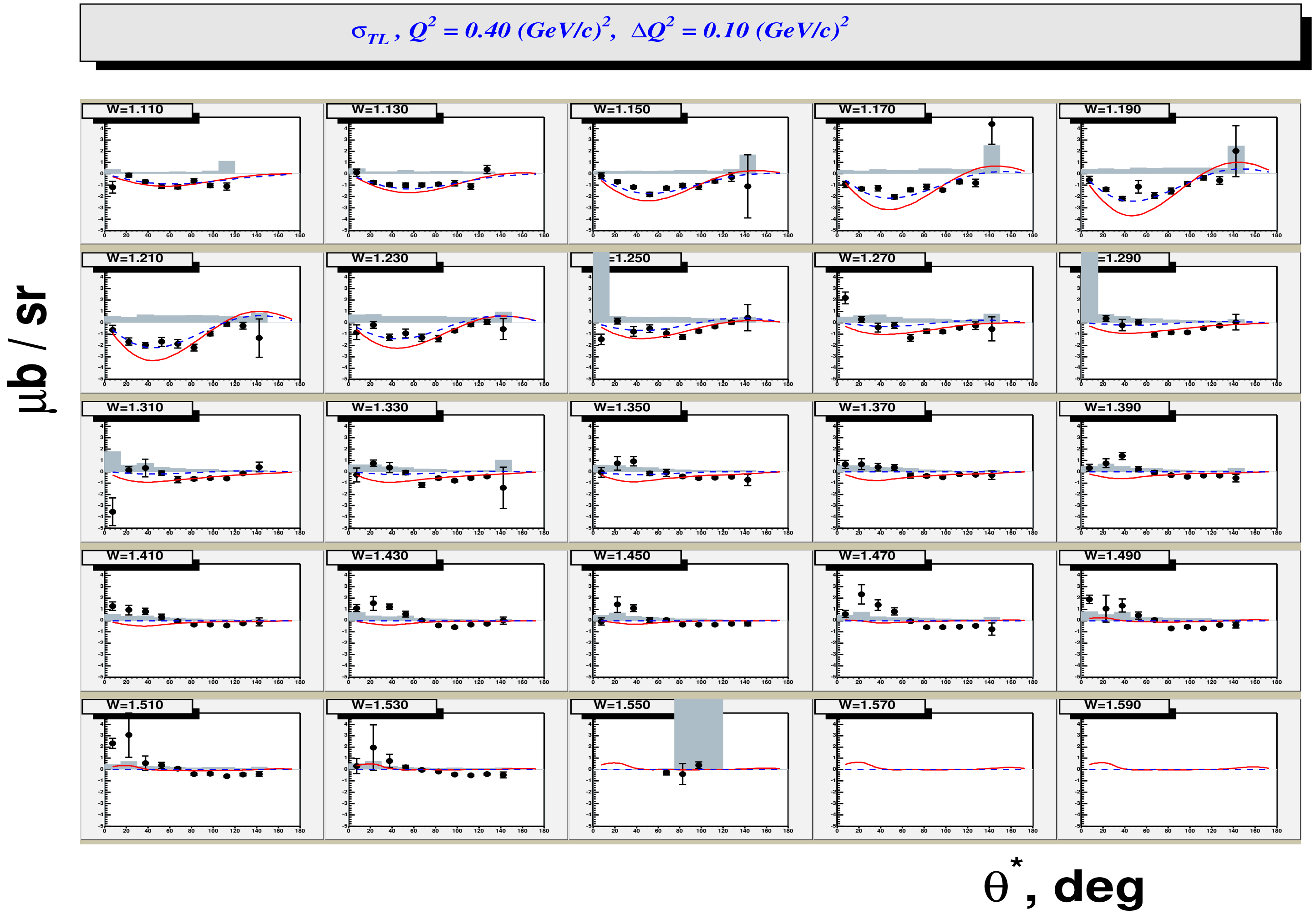

Figure A.5: Dependence of σ_{TL} on θ at $Q^2 = 0.4$ GeV^2. Red solid curve represents MAID-2000 calculations, while the blue dashed curve shows the predictions of the Sato-Lee model. Shaded areas represent the systematic uncertainties.

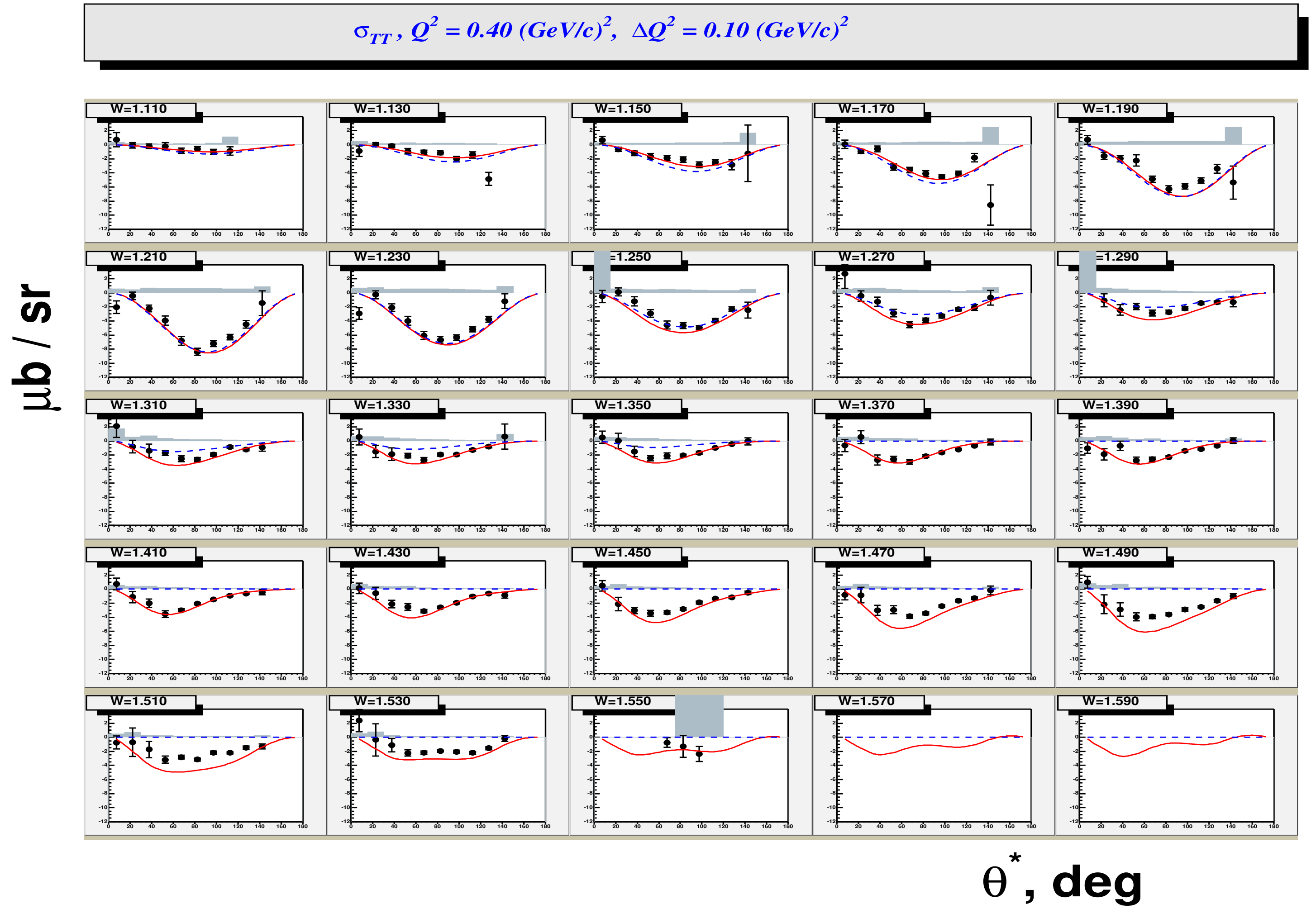

Figure A.6: Dependence of σ_{TT} on θ at $Q^2 = 0.4$ GeV^2. Red solid curve represents MAID-2000 calculations, while the blue dashed curve shows the predictions of the Sato-Lee model. Shaded areas represent the systematic uncertainties.

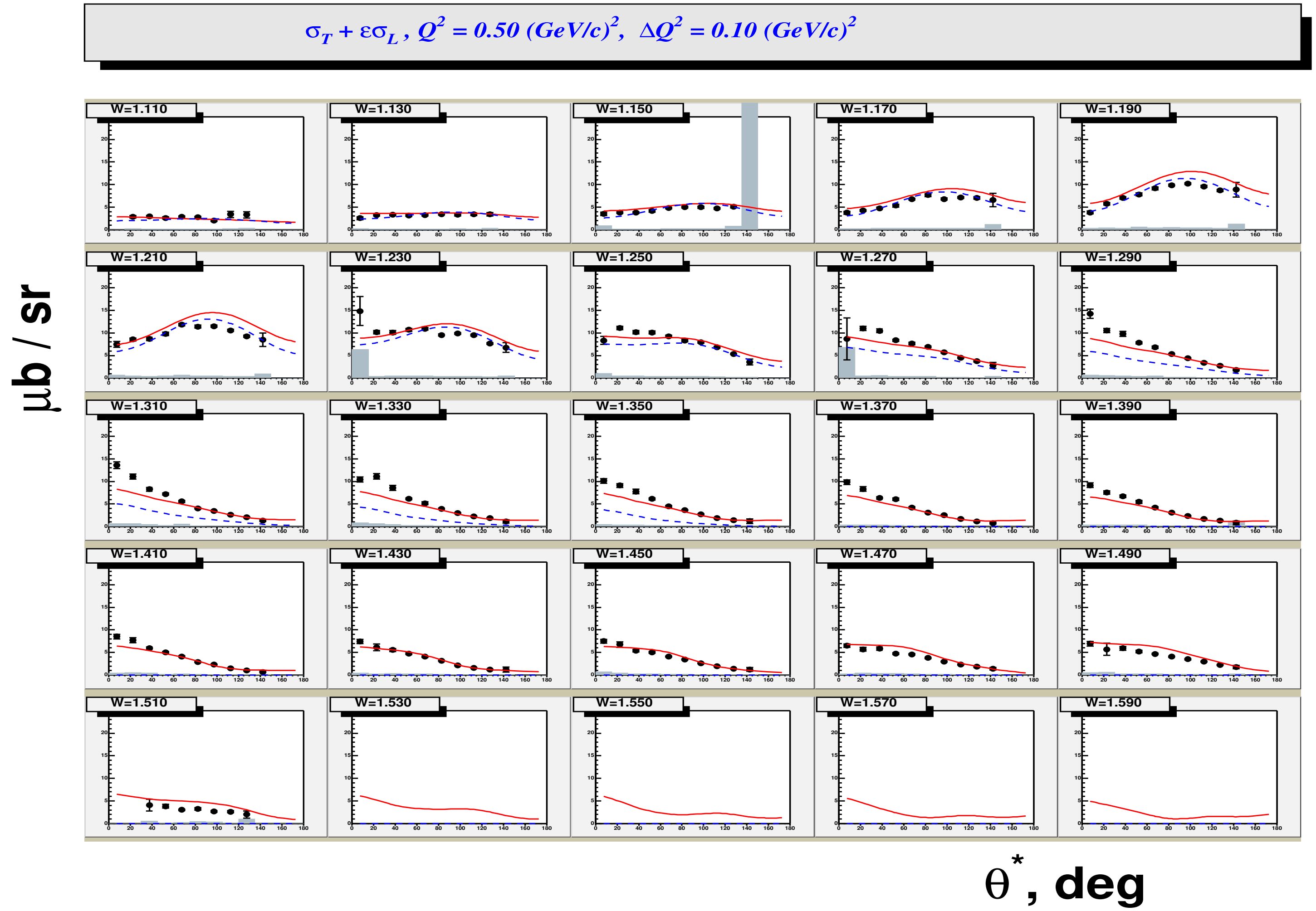

Figure A.7: Dependence of $\sigma_T + \epsilon\sigma_L$ on θ at $Q^2 = 0.5$ GeV^2. Red solid curve represents MAID-2000 calculations, while the blue dashed curve shows the predictions of the Sato-Lee model. Shaded areas represent the systematic uncertainties.

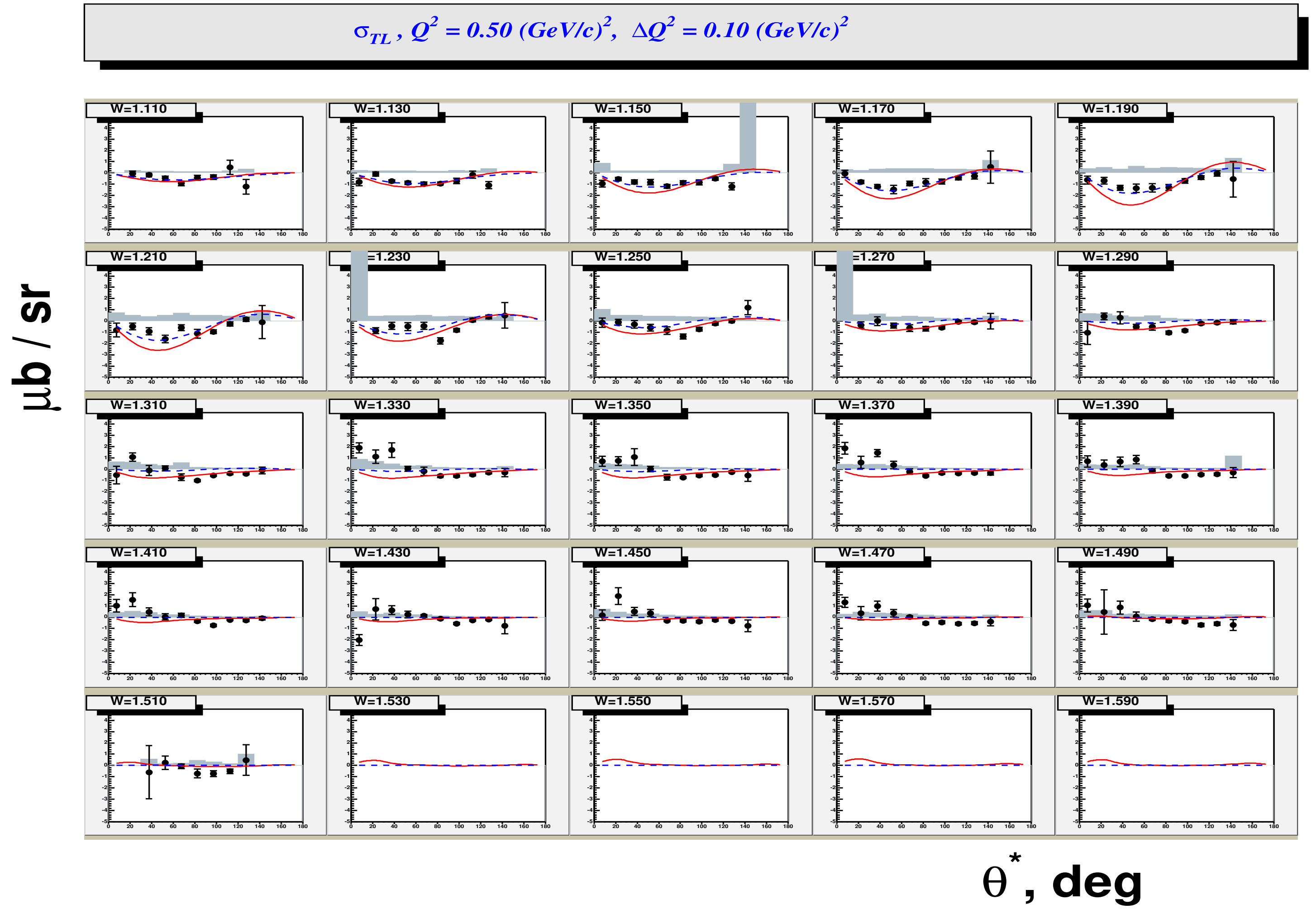

Figure A.8: Dependence of σ_{TL} on θ at $Q^2 = 0.5$ GeV^2. Red solid curve represents MAID-2000 calculations, while the blue dashed curve shows the predictions of the Sato-Lee model. Shaded areas represent the systematic uncertainties.

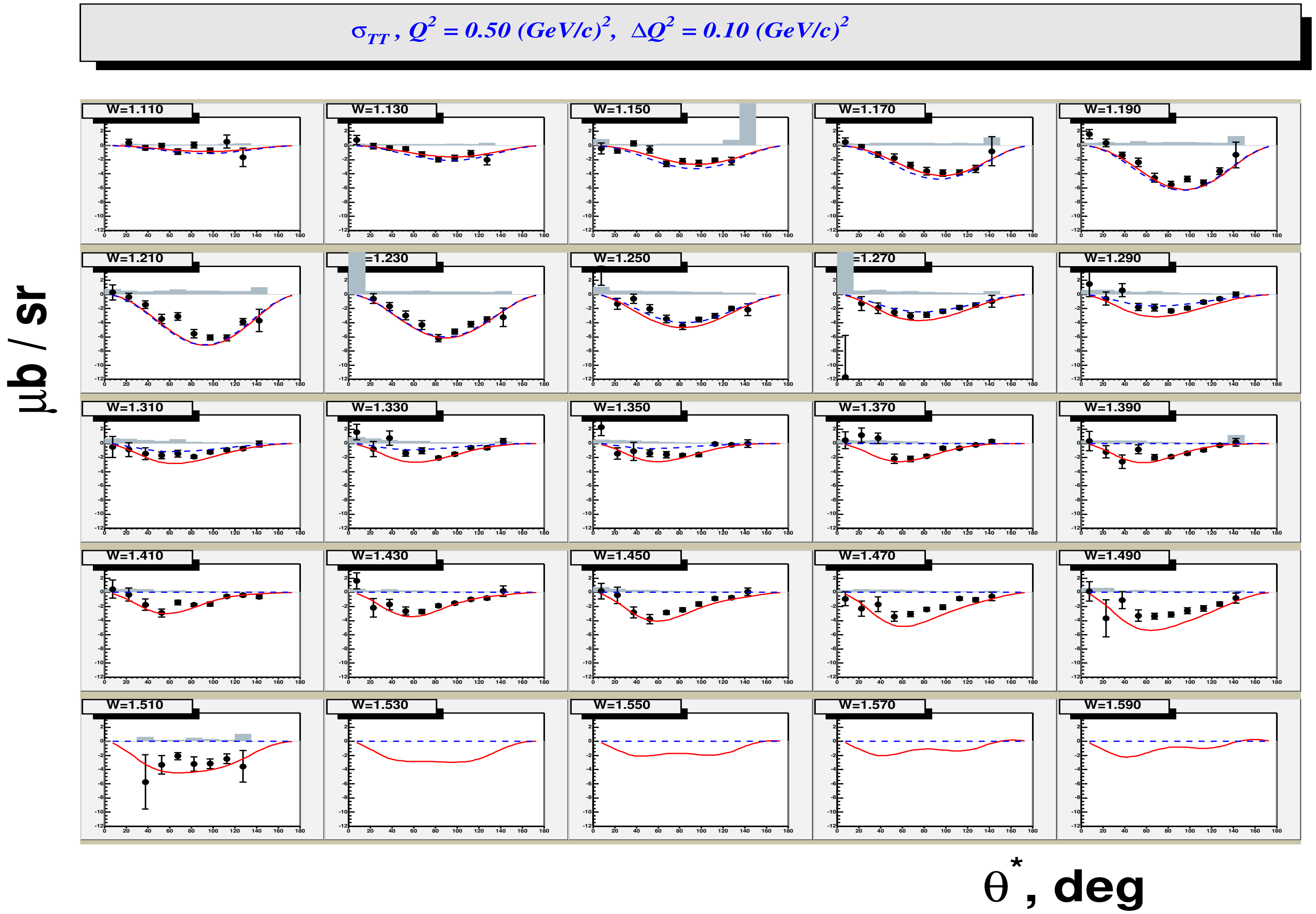

Figure A.9: Dependence of σ_{TT} on θ at $Q^2 = 0.5$ GeV^2. Red solid curve represents MAID-2000 calculations, while the blue dashed curve shows the predictions of the Sato-Lee model. Shaded areas represent the systematic uncertainties.

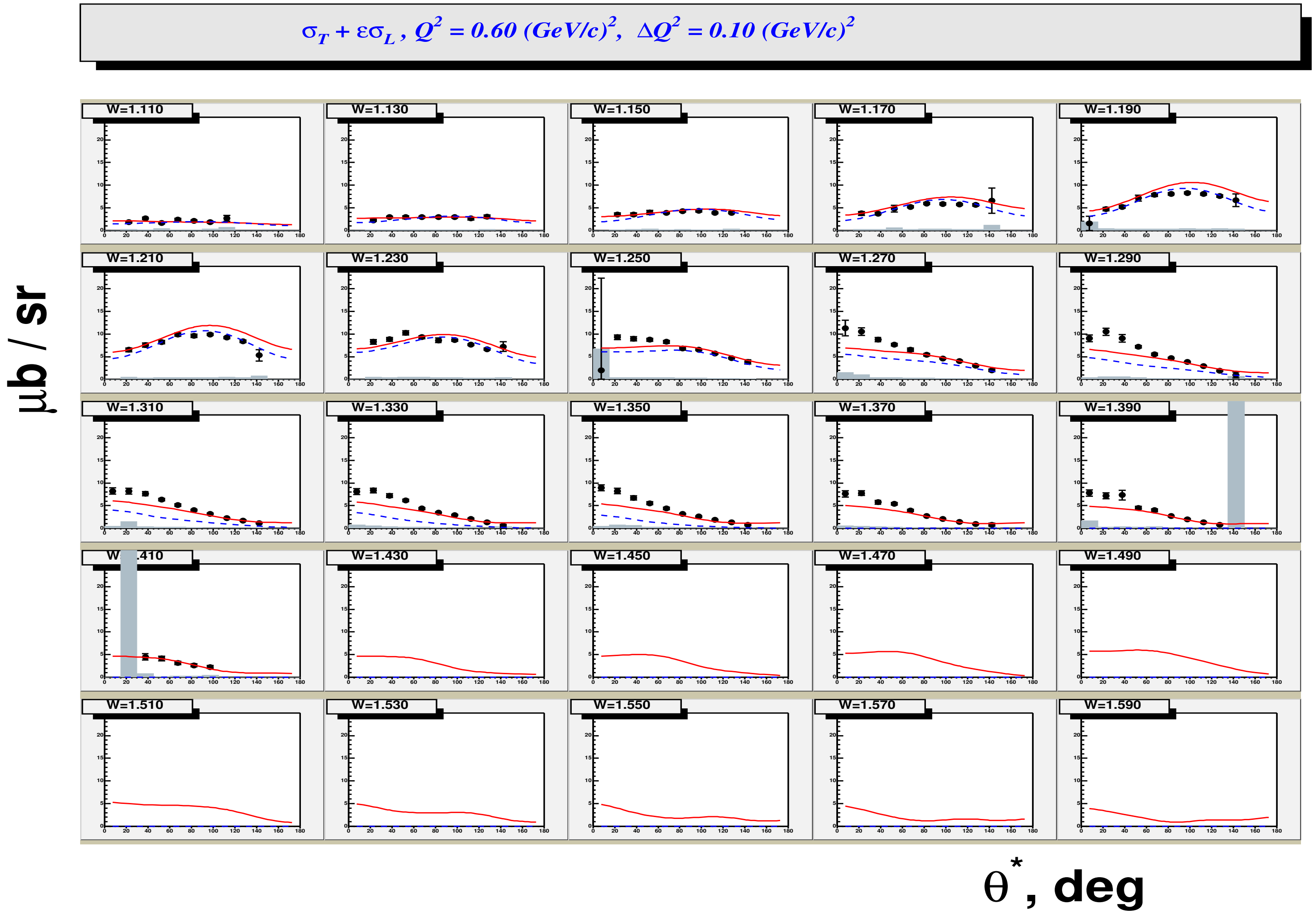

Figure A.10: Dependence of $\sigma_T + \epsilon\sigma_L$ on θ at $Q^2 = 0.6$ GeV^2. Red solid curve represents MAID-2000 calculations, while the blue dashed curve shows the predictions of the Sato-Lee model. Shaded areas represent the systematic uncertainties.

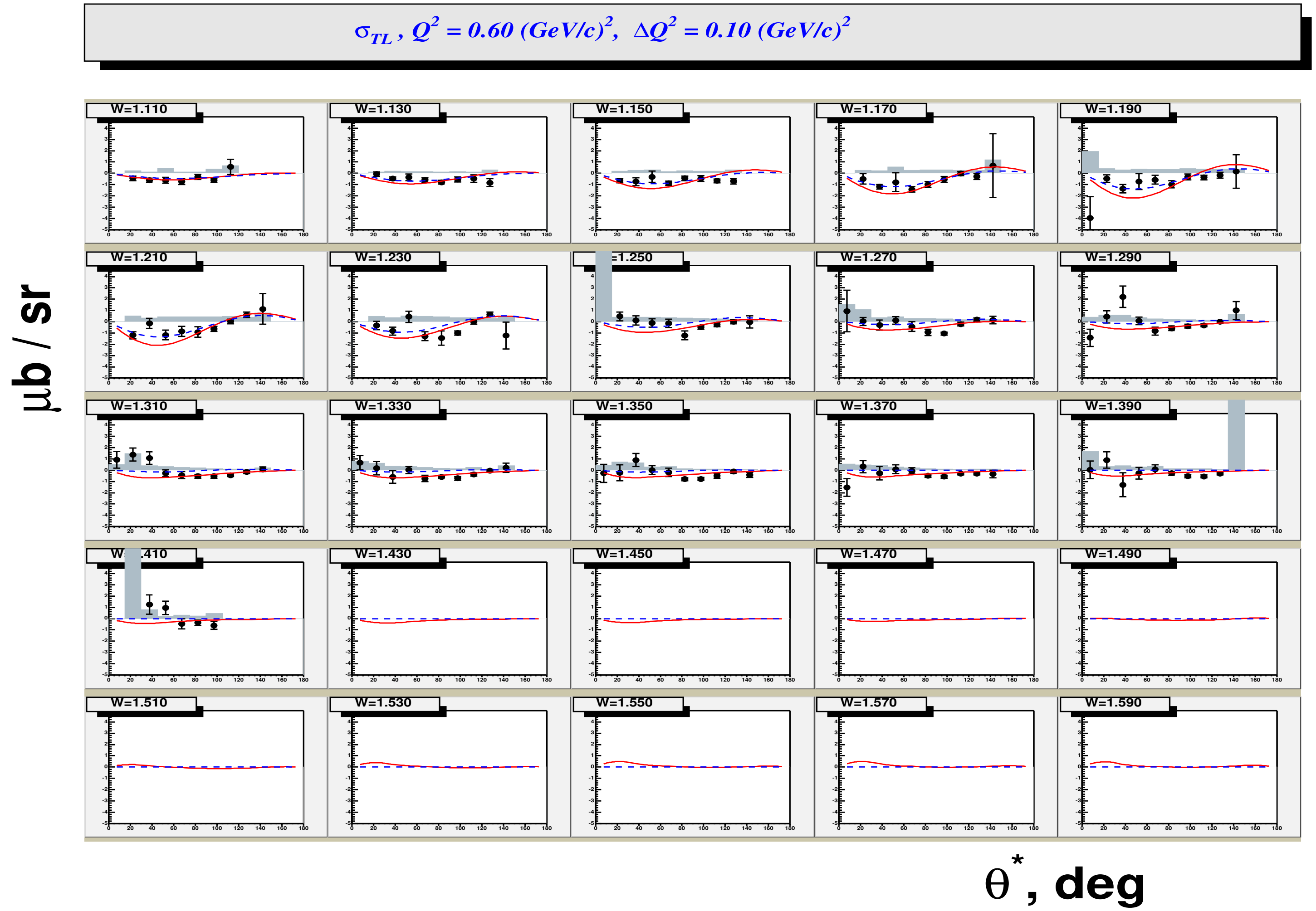

Figure A.11: Dependence of σ_{TL} on θ at $Q^2 = 0.6$ GeV^2. Red solid curve represents MAID-2000 calculations, while the blue dashed curve shows the predictions of the Sato-Lee model. Shaded areas represent the systematic uncertainties.

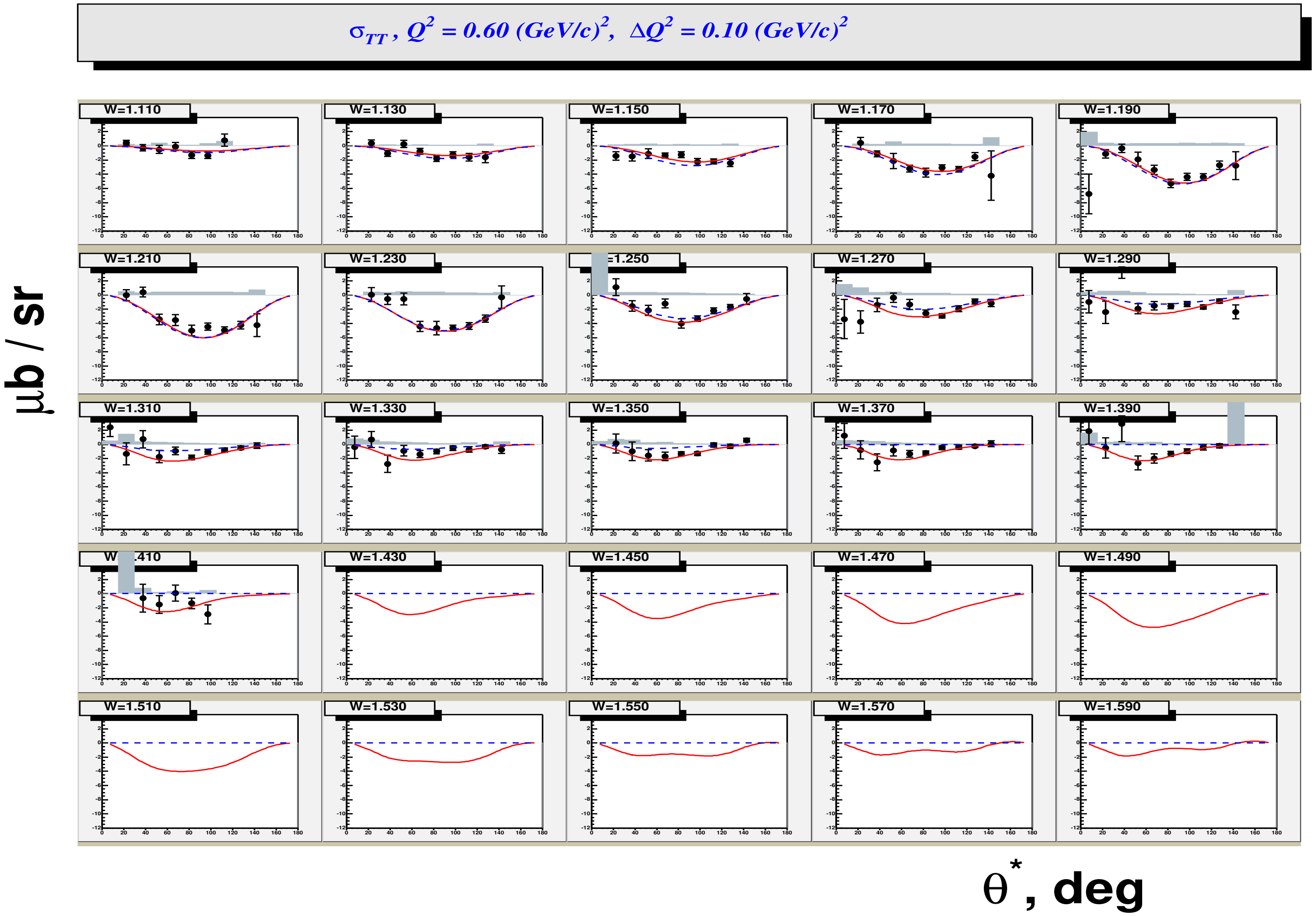

Figure A.12: Dependence of σ_{TT} on θ at $Q^2 = 0.6$ GeV^2. Red solid curve represents MAID-2000 calculations, while the blue dashed curve shows the predictions of the Sato-Lee model. Shaded areas represent the systematic uncertainties.

APPENDIX B

Dependence of the Structure Functions on W

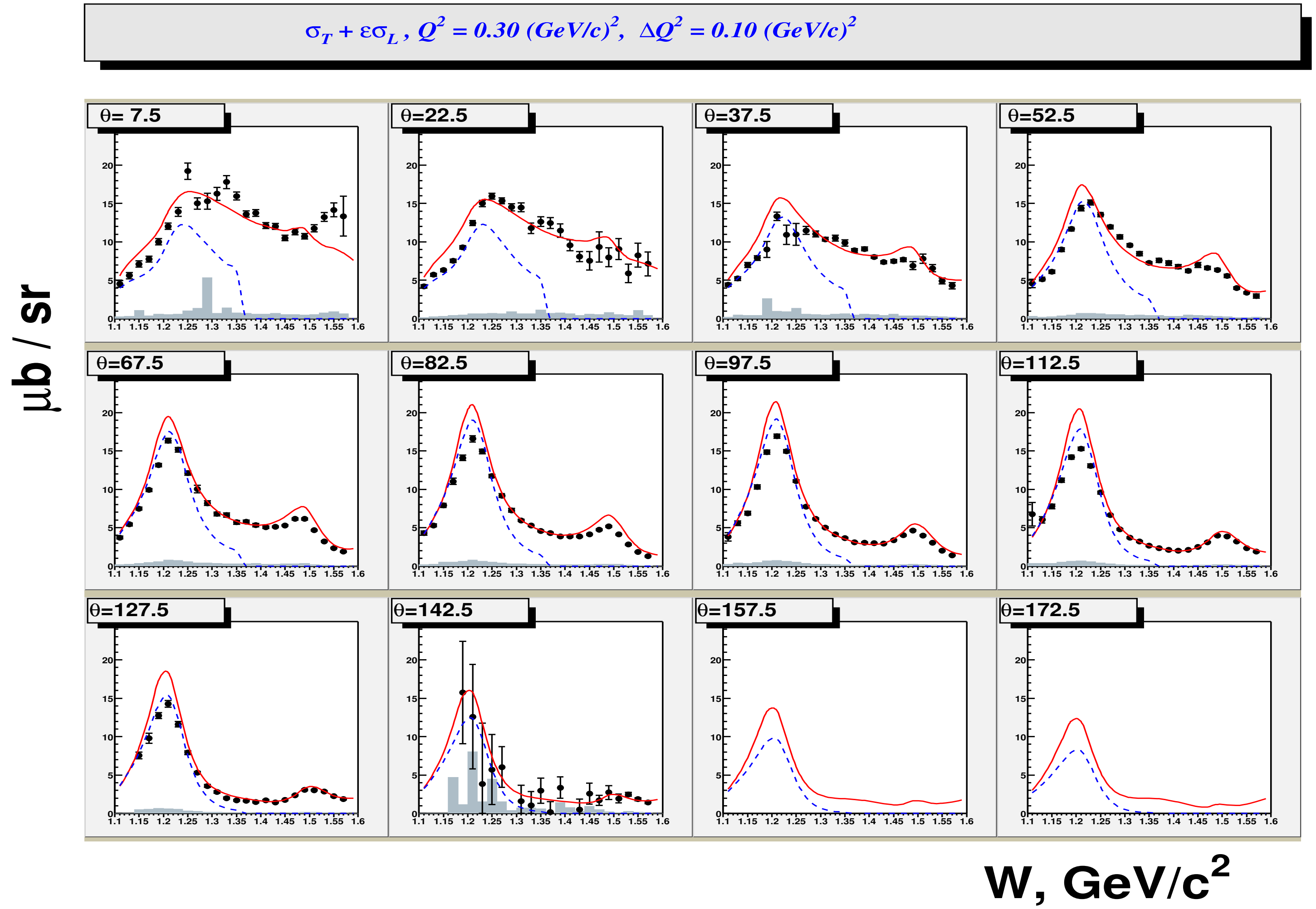

Figure B.1: Dependence of $\sigma_T + \epsilon\sigma_L$ on W at $Q^2 = 0.3$ GeV^2. Red solid curve represents MAID-2000 calculations, while the blue dashed curve shows the predictions of the Sato-Lee model. Shaded areas represent the systematic uncertainties.

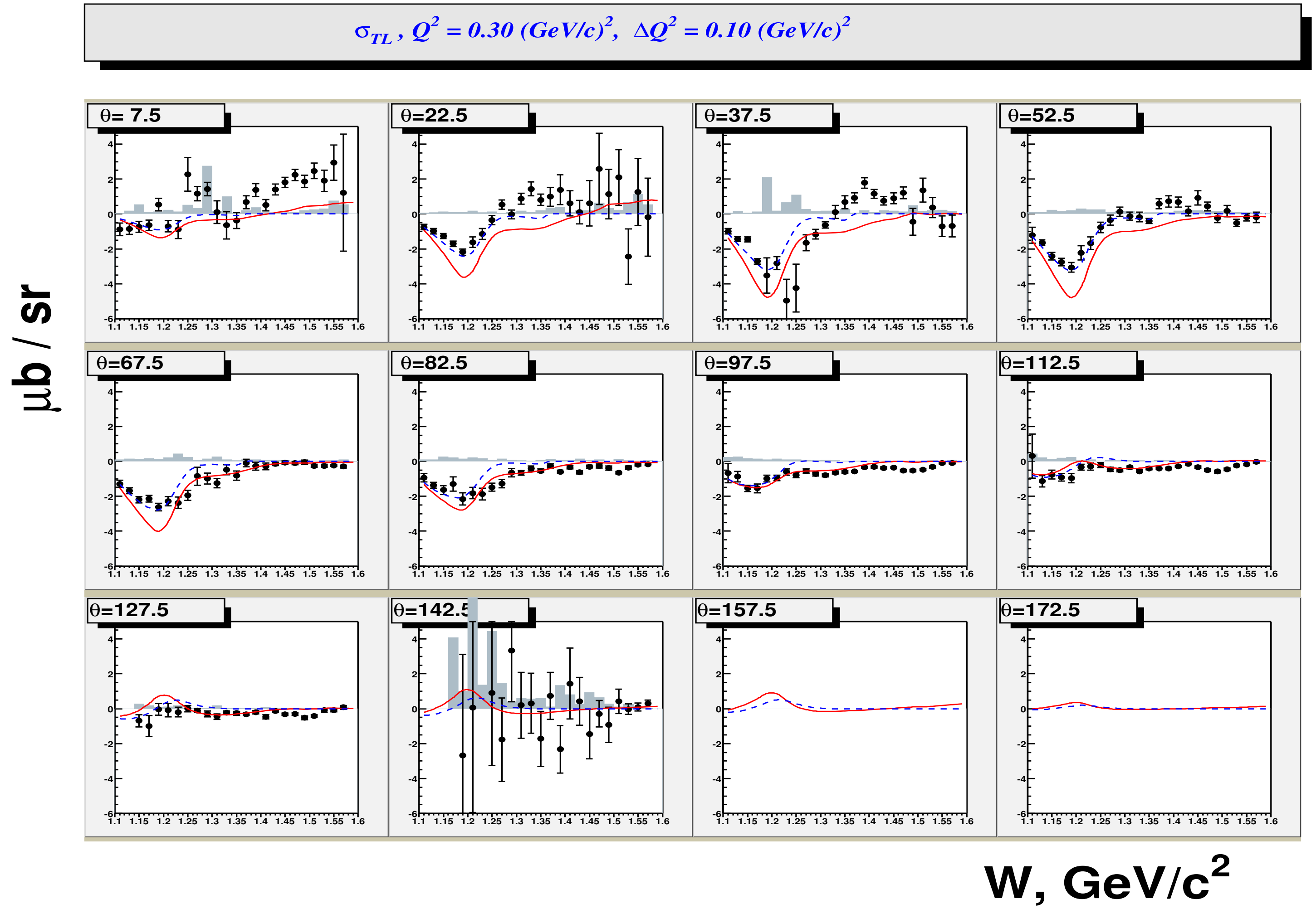

Figure B.2: Dependence of σ_{TL} on W at $Q^2 = 0.3$ GeV^2. Red solid curve represents MAID-2000 calculations, while the blue dashed curve shows the predictions of the Sato-Lee model. Shaded areas represent the systematic uncertainties.

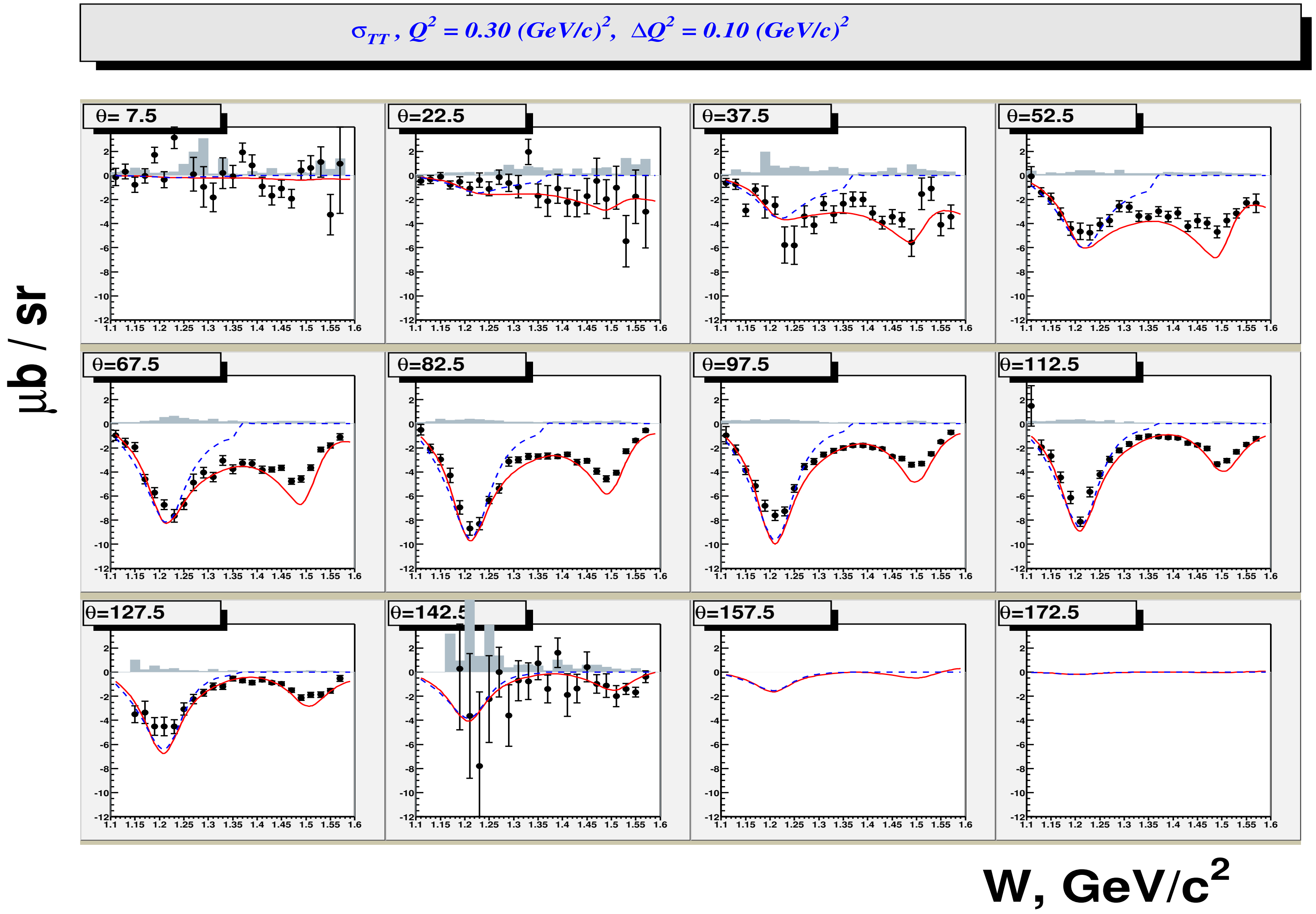

Figure B.3: Dependence of σ_{TT} on W at $Q^2 = 0.3$ GeV^2. Red solid curve represents MAID-2000 calculations, while the blue dashed curve shows the predictions of the Sato-Lee model. Shaded areas represent the systematic uncertainties.

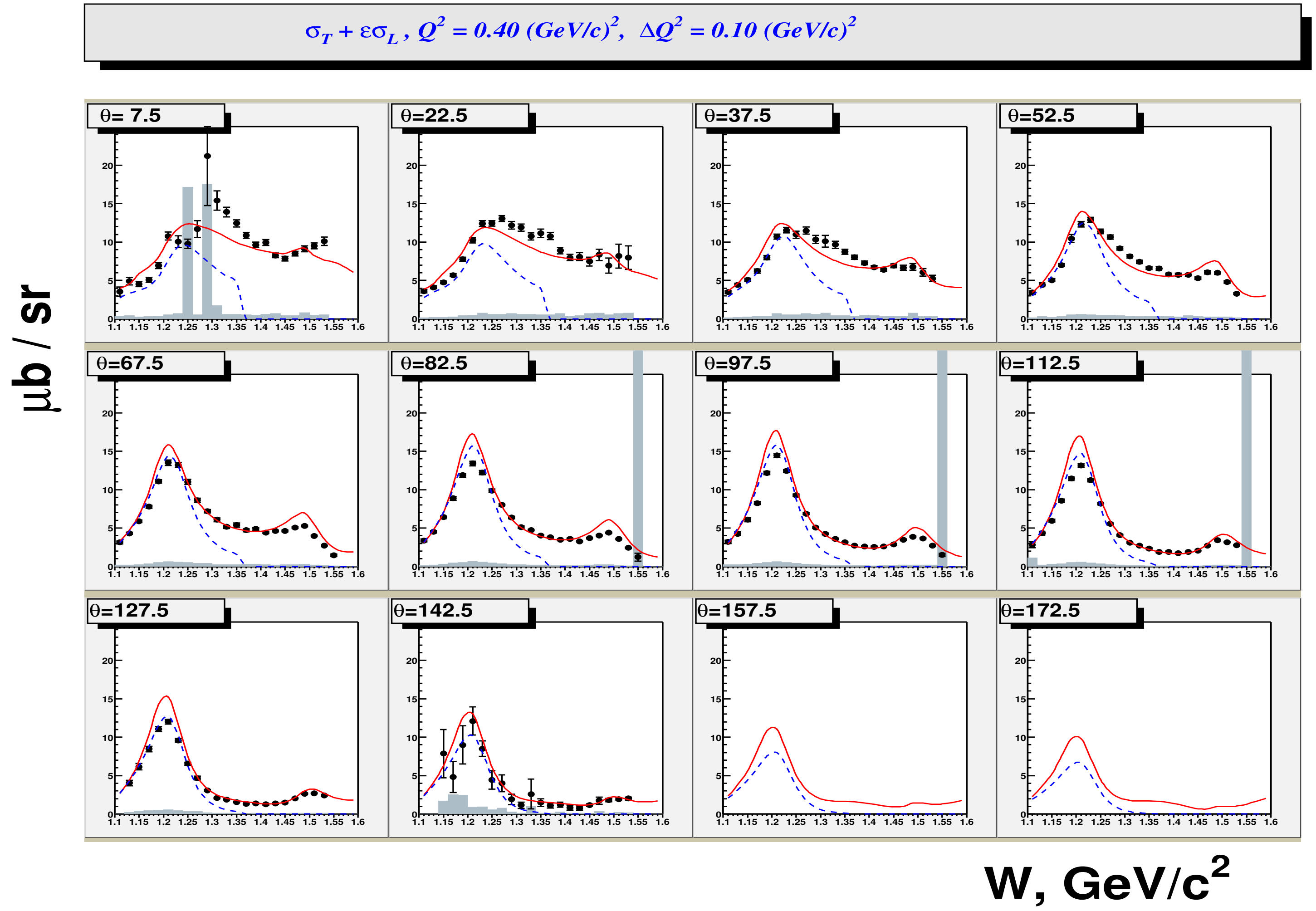

Figure B.4: Dependence of $\sigma_T + \epsilon\sigma_L$ on W at $Q^2 = 0.4$ GeV^2. Red solid curve represents MAID-2000 calculations, while the blue dashed curve shows the predictions of the Sato-Lee model. Shaded areas represent the systematic uncertainties.

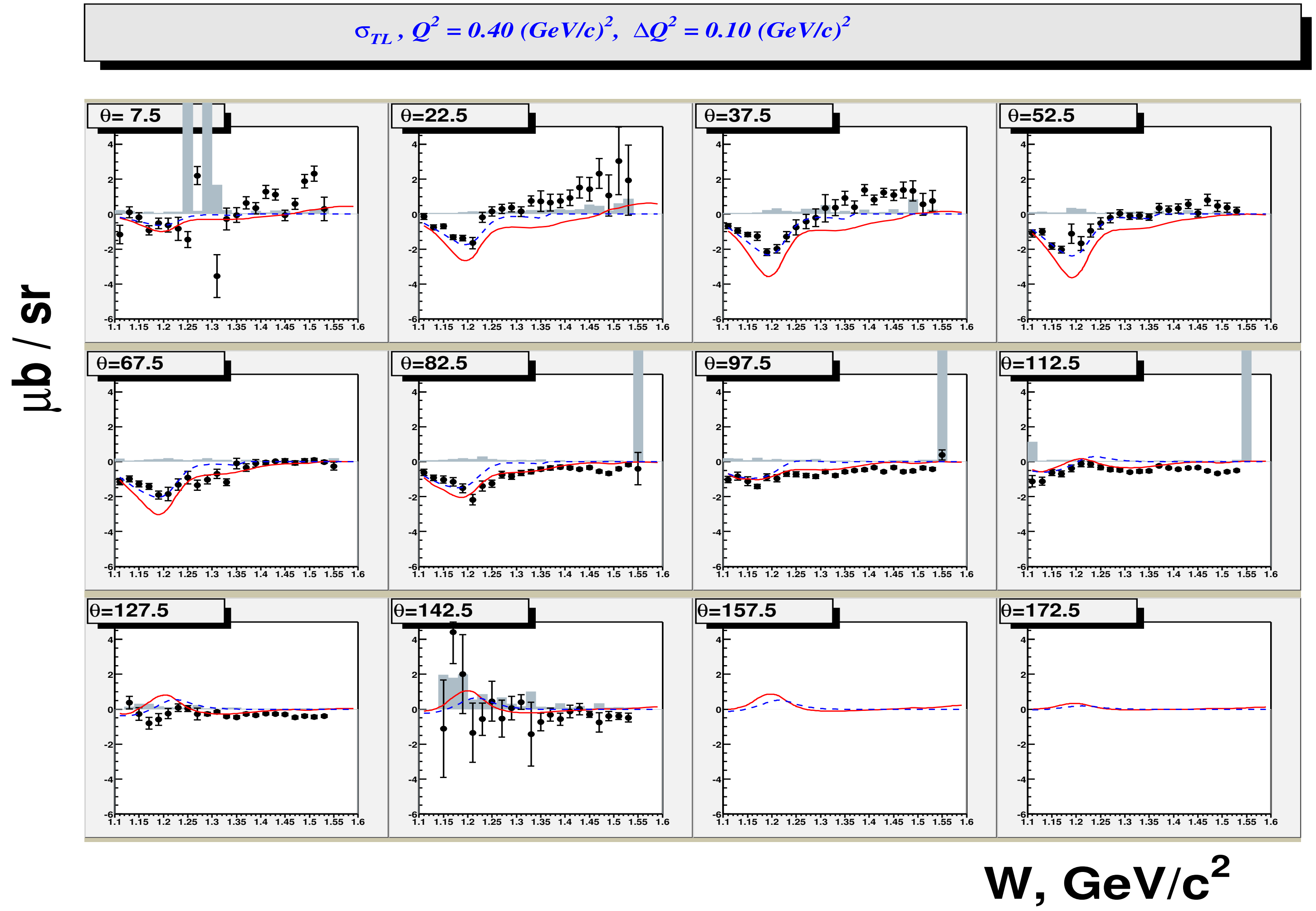

Figure B.5: Dependence of σ_{TL} on W at $Q^2 = 0.4$ GeV^2. Red solid curve represents MAID-2000 calculations, while the blue dashed curve shows the predictions of the Sato-Lee model. Shaded areas represent the systematic uncertainties.

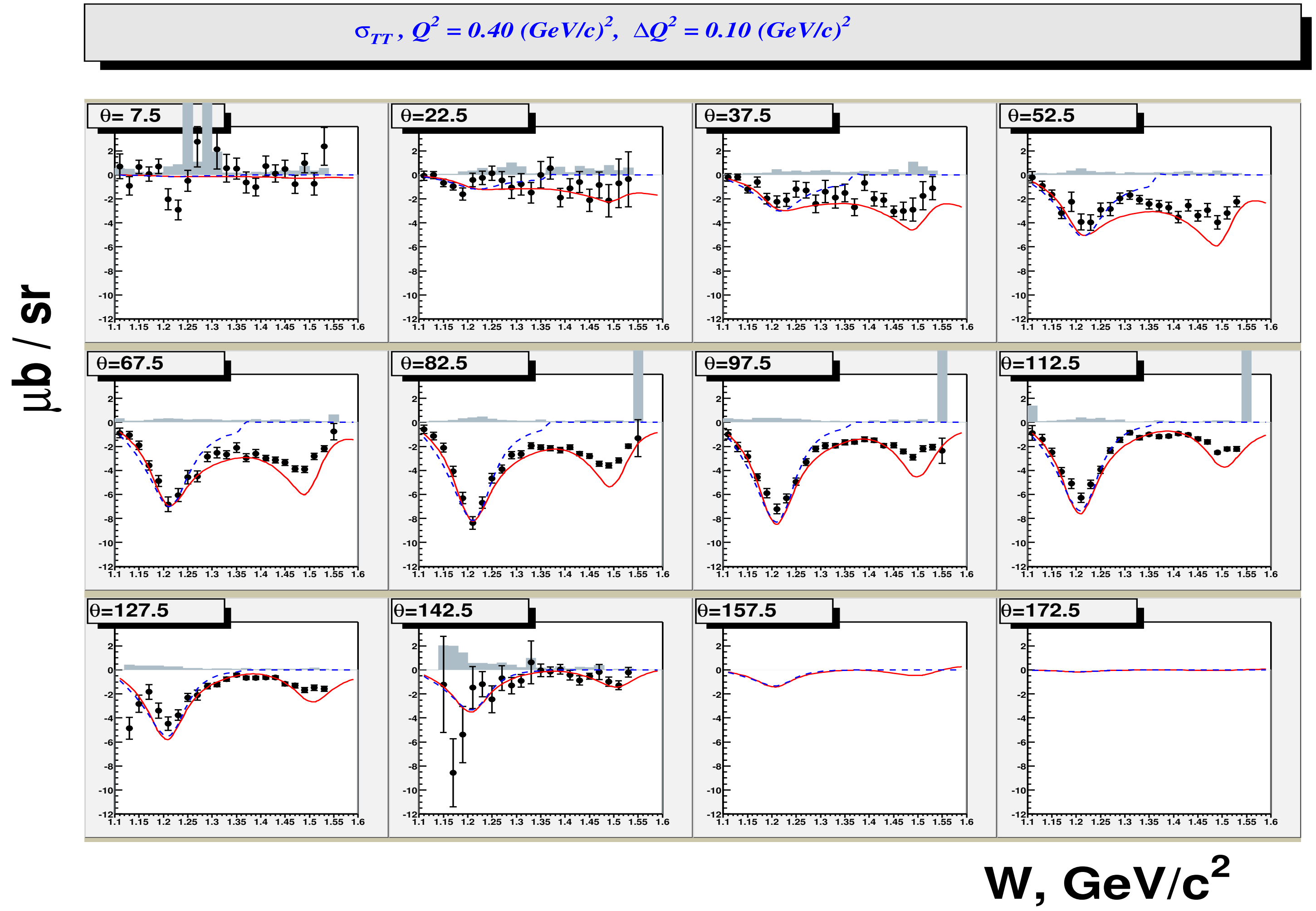

Figure B.6: Dependence of σ_{TT} on W at $Q^2 = 0.4$ GeV^2. Red solid curve represents MAID-2000 calculations, while the blue dashed curve shows the predictions of the Sato-Lee model. Shaded areas represent the systematic uncertainties.

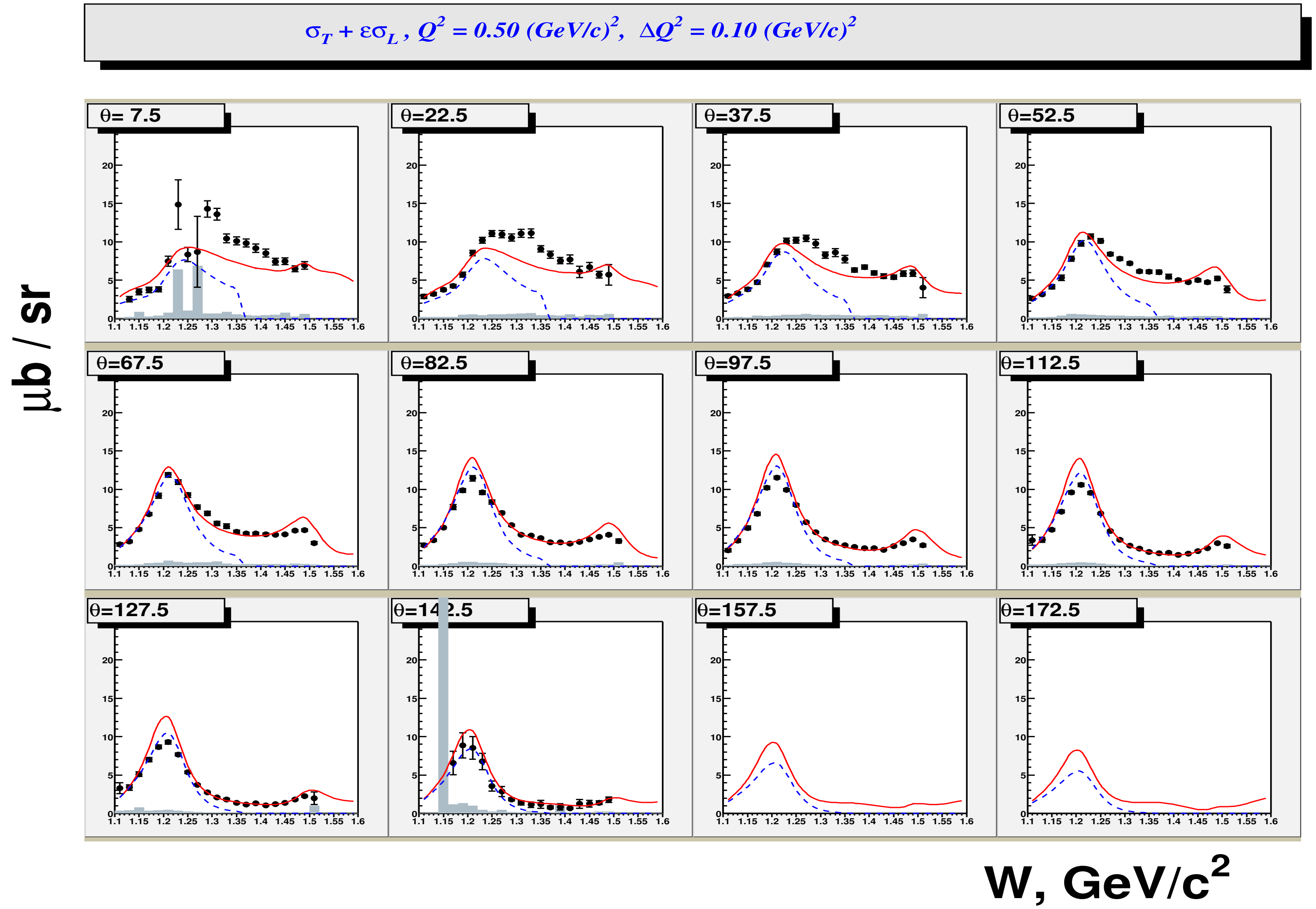

Figure B.7: Dependence of $\sigma_T + \epsilon\sigma_L$ on W at $Q^2 = 0.5$ GeV^2. Red solid curve represents MAID-2000 calculations, while the blue dashed curve shows the predictions of the Sato-Lee model. Shaded areas represent the systematic uncertainties.

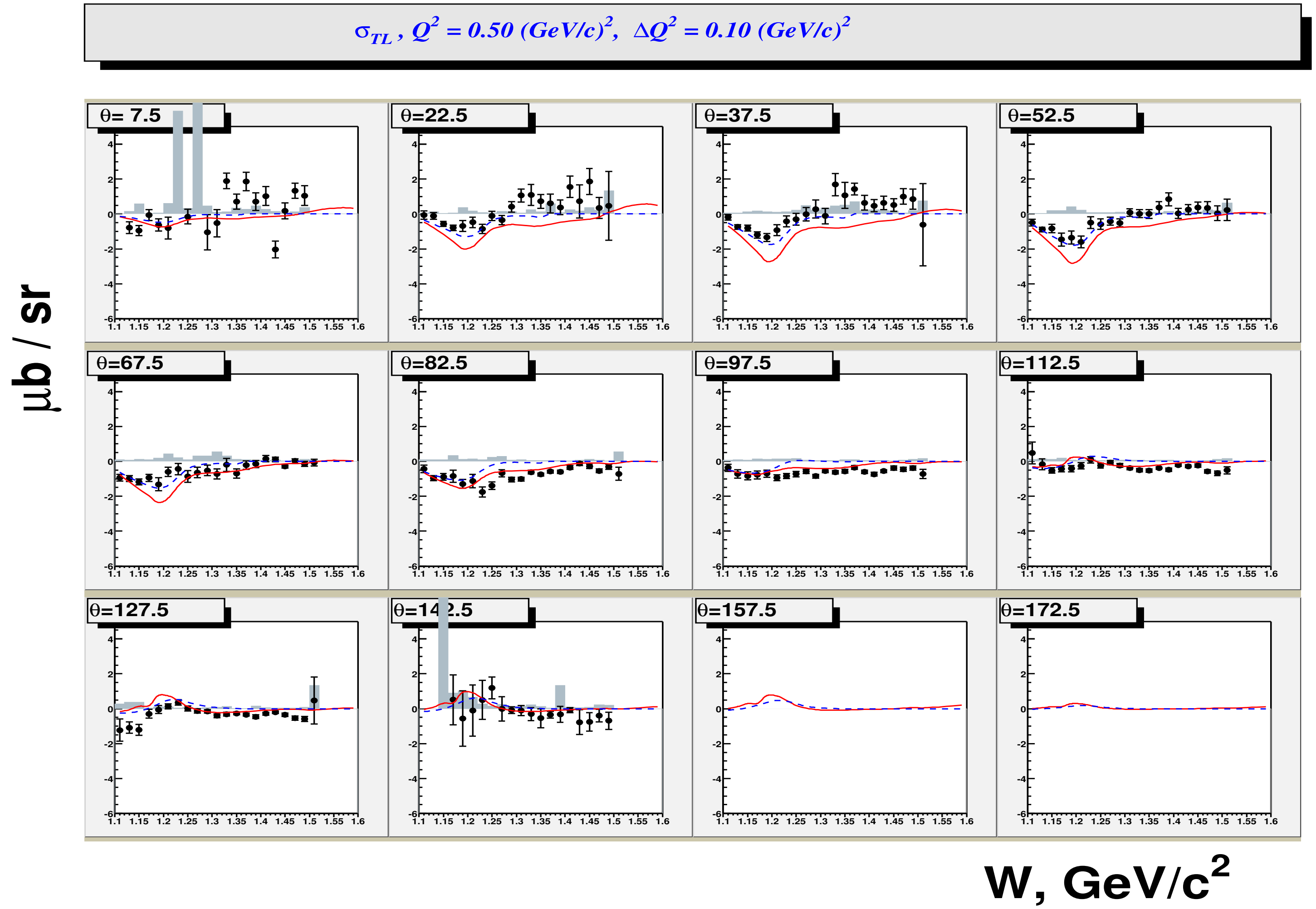

Figure B.8: Dependence of σ_{TL} on W at $Q^2 = 0.5$ GeV^2. Red solid curve represents MAID-2000 calculations, while the blue dashed curve shows the predictions of the Sato-Lee model. Shaded areas represent the systematic uncertainties.

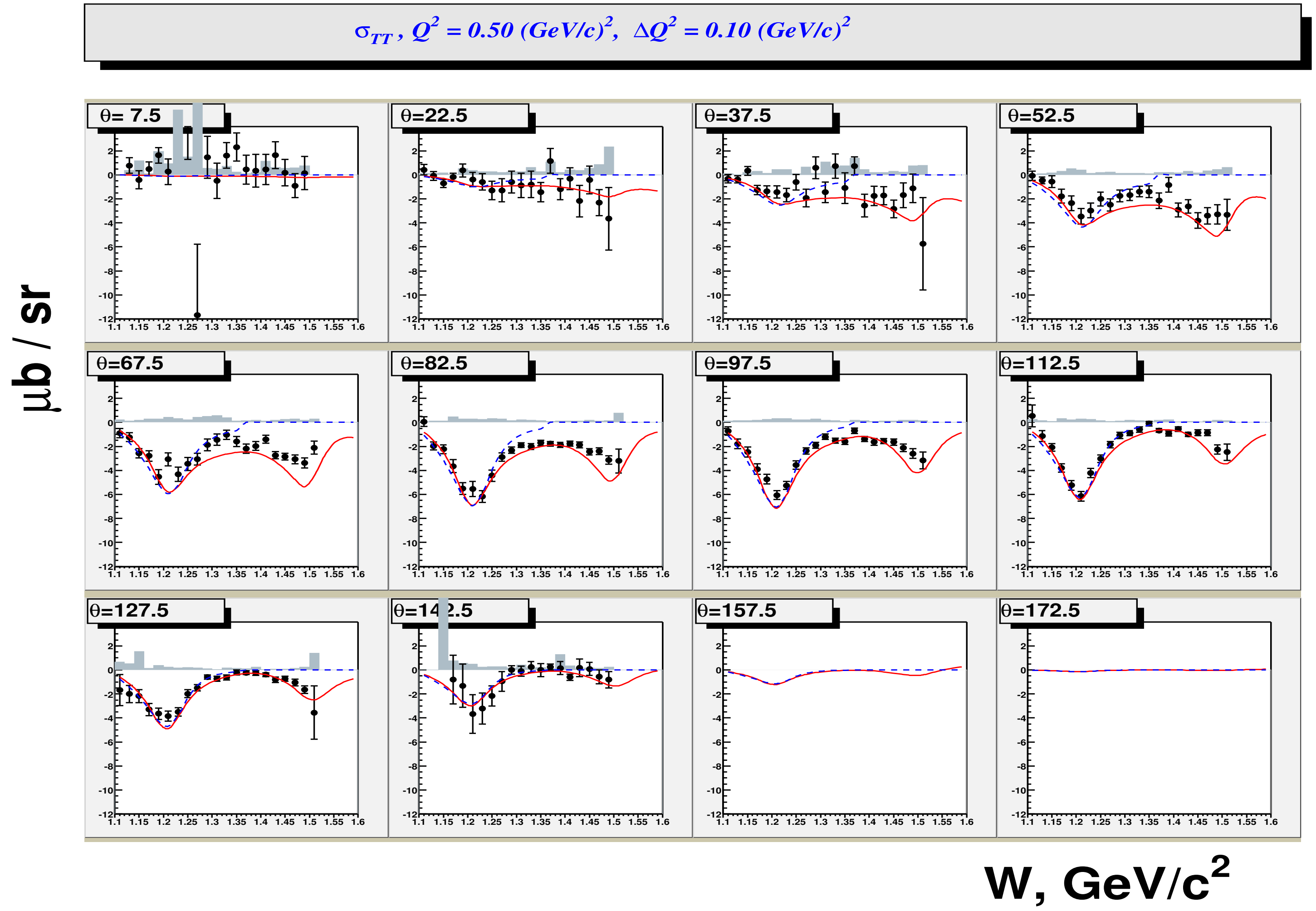

Figure B.9: Dependence of σ_{TT} on W at $Q^2 = 0.5$ GeV^2. Red solid curve represents MAID-2000 calculations, while the blue dashed curve shows the predictions of the Sato-Lee model. Shaded areas represent the systematic uncertainties.

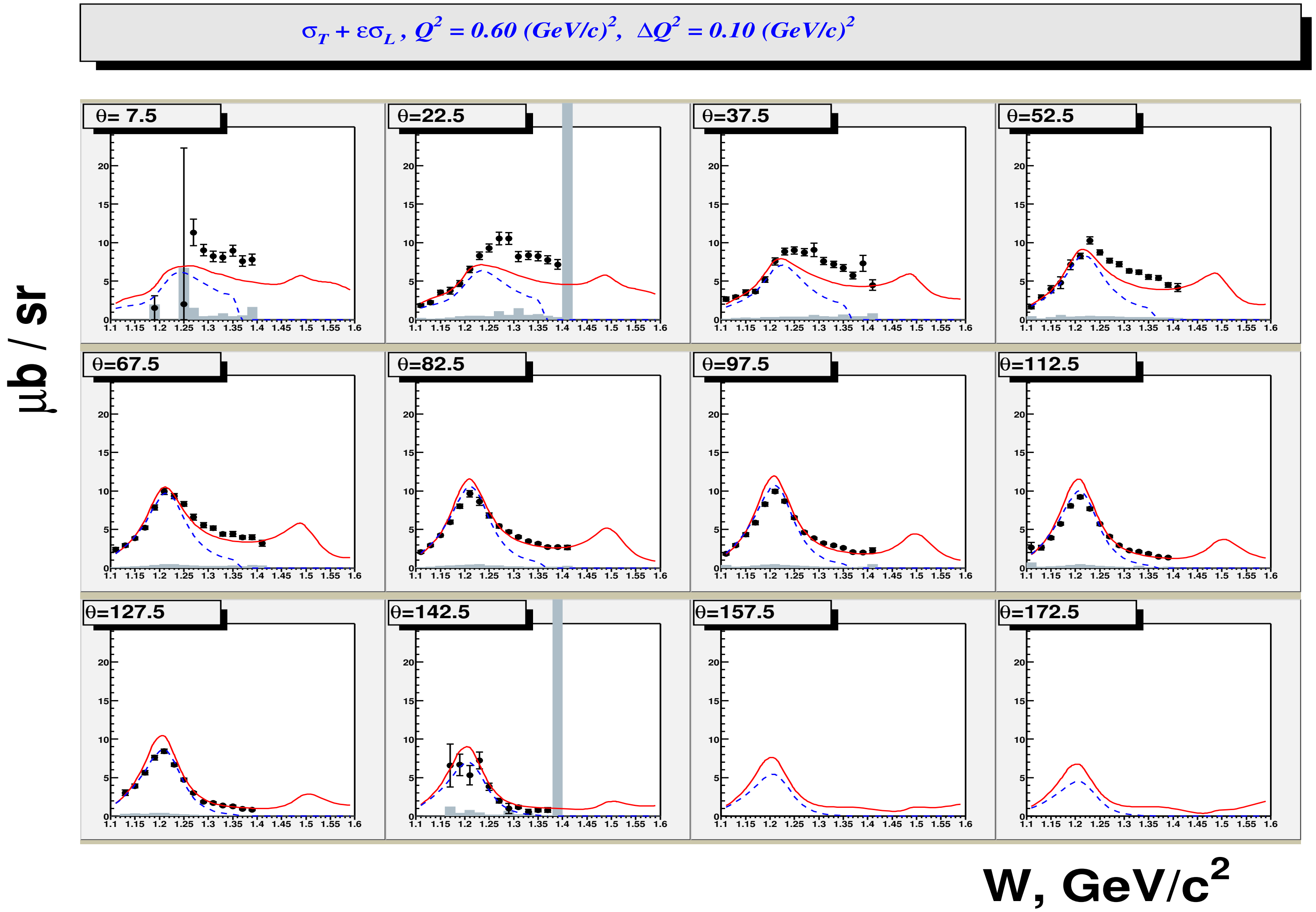

Figure B.10: Dependence of $\sigma_T + \epsilon\sigma_L$ on W at $Q^2 = 0.6$ GeV^2. Red solid curve represents MAID-2000 calculations, while the blue dashed curve shows the predictions of the Sato-Lee model. Shaded areas represent the systematic uncertainties.

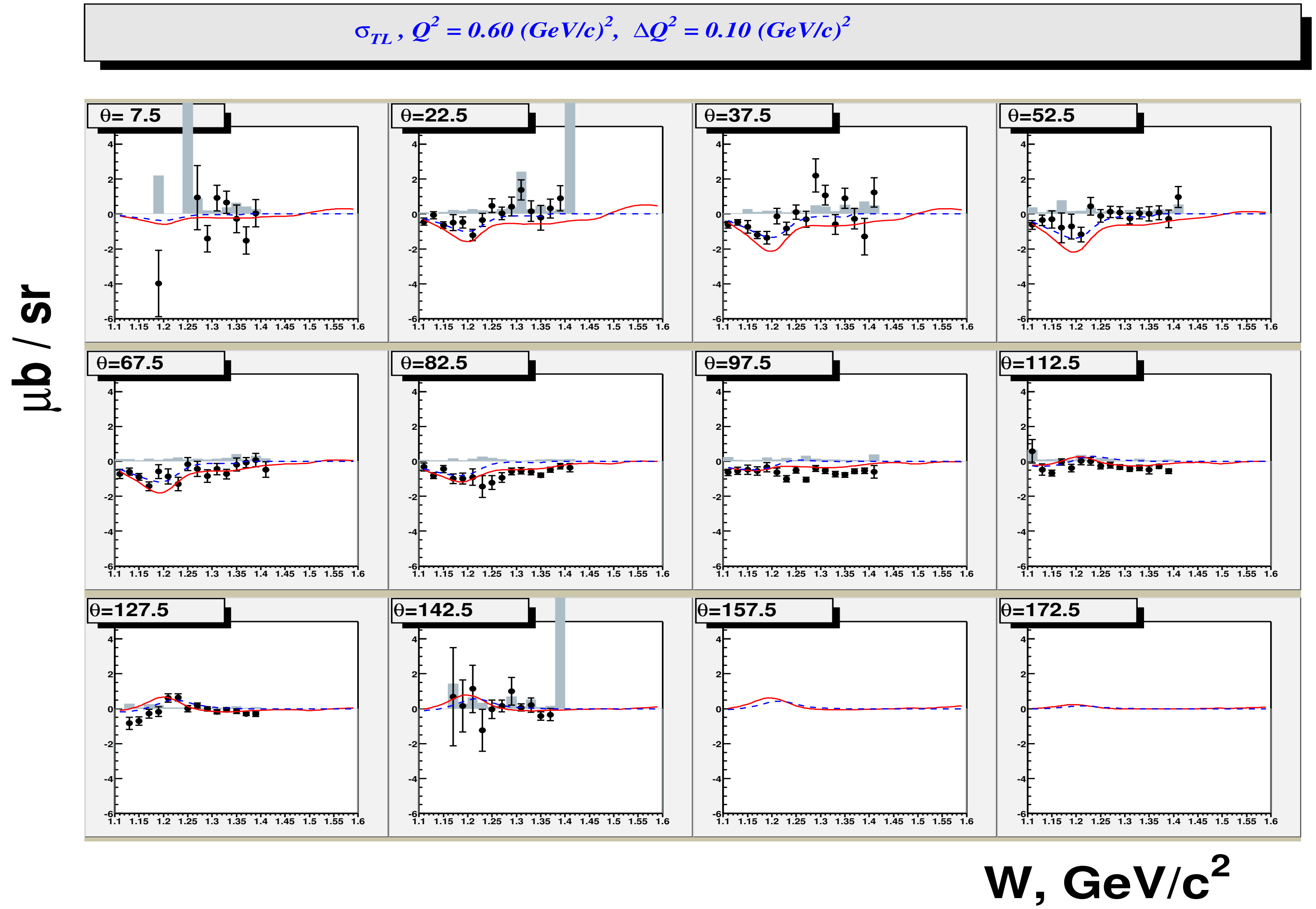

Figure B.11: Dependence of σ_{TL} on W at $Q^2 = 0.6$ GeV^2. Red solid curve represents MAID-2000 calculations, while the blue dashed curve shows the predictions of the Sato-Lee model. Shaded areas represent the systematic uncertainties.

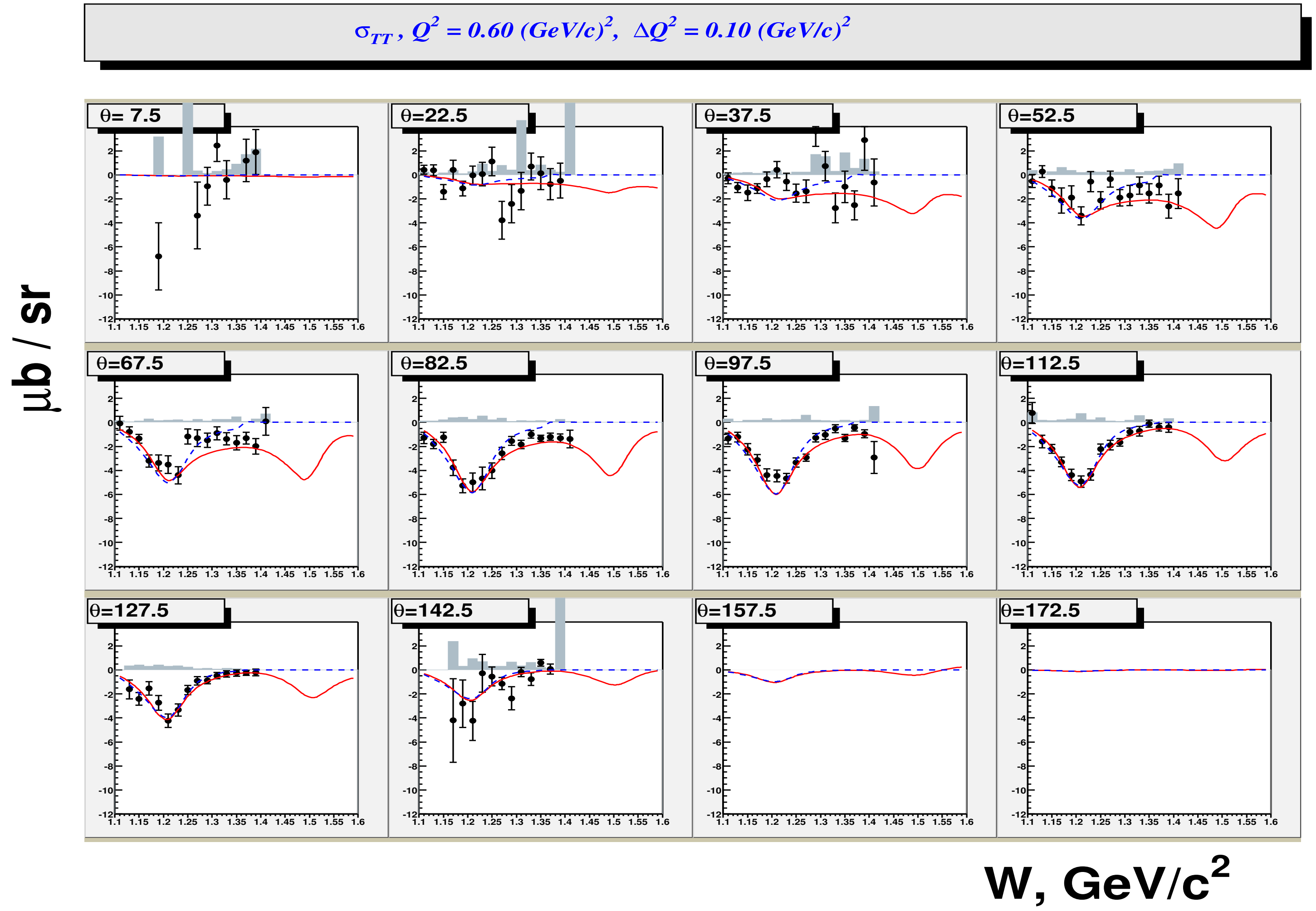

Figure B.12: Dependence of σ_{TT} on W at $Q^2 = 0.6$ GeV^2. Red solid curve represents MAID-2000 calculations, while the blue dashed curve shows the predictions of the Sato-Lee model. Shaded areas represent the systematic uncertainties.

BIBLIOGRAPHY

[1] F. Foster, and G. Hughes, "Electroproduction of nuclear resonances", Rept. Prog. Phys. **46**, 1445, (1983).

[2] I.G. Aznauryan, "How to extract $P_{33}(1232)$ resonance contributions from the amplitudes $M_{1+}^{3/2}$, $E_{1+}^{3/2}$, $S_{1+}^{3/2}$ of pion electroproduction on nucleons", Phys. Rev. D **57**, 2727, (1998).

[3] M. Jacob and G.C. Wick, "On the general theory of collisions for particles with spin", Annals of Physics **7**, 404, (1959).

[4] V. Burkert, "Leptonic Production of Baryon Resonances", Perspective in the Structure of Hadronic Systems, Edited by M.N. Harakeh, *et al.*, Plenum Press, New York, (1994).

[5] D. Drechsel and L. Tiator, "Threshold pion photoproduction on nucleons", J. Phys. **G18**, 449, (1992).

[6] N. Isgur, "Nuclear physics from the quark model with chromodynamics", Acta Austriaca, Suppl. XXVII, 177, (1985).

[7] N. Isgur, J. Paton, "Flux-tube model for hadrons in QCD", Phys. Rev. D **31**, 2910, (1985).

[8] C.E. Carlson, "Electromagnetic $N - \Delta$ transitions at high Q^2", Phys. Rev. D **34**, 2704, (1986).

[9] Zh. Li, V. Burkert, Zh. Li, "Electroproduction of the Roper resonance as a hybrid state", Phys. Rev. D **46**, 70, (1992).

[10] S.S. Kamalov and Shin Nan Yang, "Pion Cloud and the Q^2 dependence of $\gamma^* N \to \Delta$ Transition Form Factors", Phys. Rev. Lett. **83**, 4494, (1999).

[11] R.L. Walker, "Phenomenological Analysis of Single Pion Photoproduction", Phys. Rev. **182**, 1729, (1969).

[12] V. D. Burkert, L. Elouadrhiri, "E_{1+}/M_{1+} and S_{1+}/M_{1+} from an Analysis of $p(e,e'p)\pi^0$ in the Region of the $\Delta(1232)$ Resonance at $Q^2 = 3.2$ (GeV/c)^2" , Phys. Rev. Lett. **75**, 3614, (1995).

[13] J.D. Walecka and P.A. Zucker, "Relativistic Model for Electroproduction of Nucleon resonances", Phys. Rev. **187**, 1479, (1968).

[14] I.G. Aznauryan, S.G. Stepanyan, "P_{33} resonance contribution to the amplitudes $M_{1+}^{3/2}$, $E_{1+}^{3/2}$, $S_{1+}^{3/2}$ from an analysis of the $p(e,e'p)\pi^0$ data at $Q^2 = 2.8$, 3.2 and 4 (Gev/c)^2 within the dispersion relations approach", Phys. Rev. D **59**, 1, (1999); Ch. Gerhardt, "A resonance Analysis of Electroproduction Data", Z. Phys. **C4**, 311, (1980); O. Hanstein, D. Drechsel, L. Tiator, "The Position and the Residues of the Delta Resonance Pole in Pion Photoproduction", Phys. Lett. **B385**, 45, (1996).

[15] Kenneth M. Watson, "Some General Relations between the Photoproduction and scattering of π Mesons", Phys. Rev. **95**, 228, (1954).

[16] T. Feuster, U. Mosel, "Unitary model for meson nucleon scattering", Phys. Rev. C **58**, 457; R.M. Davidson, N.C. Mukhopadyay, "Model-independent determination of K-matrix poles and residues in the $\Delta(1232)$ region from the multipole data for pion photoproduction", Phys. Rev. D **42**, 20, (1990).

[17] M.G. Olsson, E.T. Osypowsky, "Vector-meson-exchange and unitarity effects in low-energy photoproduction", Phys. Rev. D **17**, 174, (1979); R. M. Davidson, N.C. Mukhopadyay, R.S. Wittman, "Effective-Lagrangian approach to the theory of pion photoproduction in the $\Delta(1232)$ region", Phys. Rev. D **43**, 71, (1991); J.M. Laget, "On the Longitudinal Electromagnetic Coupling of the Delta", Nucl. Phys. **A481**, 765, (1988).

[18] R. Beck, *et al.*, "Measurement of the E2/M1 Ratio in the N $\rightarrow$ Delta Transition Using the Reaction P(Gamma(Pol.),P)Pi0", Phys. Rev. Lett. **78**, 606, (1997); R. Beck, at al., "Determination of the E2/M1 Ratio in the Gamma N $\rightarrow$ Delta(1232) Transition from a Simultaneous Measurement of P(Polarized Gamma, P) Pi0 and P(Polarized Gamma, Pi+)N", Phys. Rev. C **61**, 035204, (2000).

[19] G. Blanpied, *et al.*, "N $\rightarrow$ Delta Transition from Simultaneous Measurements of p(gamma $\rightarrow$, pi) and p(gamma $\rightarrow$, gamma)", Phys. Rev. Lett. **79**, 4337, (1997).

[20] C. Mertz, *et al.*, "Search for Quadrupole Strength in the Electroexcitation of the Delta+(1232)", Phys. Rev. Lett. **86**, 2963, (2001).

[21] V. V. Frolov, *et al.*, "Electroproduction of the Delta(1232) Resonance at High Momentum Transfer", Phys. Rev. Lett. **82**, 45, (1999).

[22] Th. Pospeschil, *et al.*, "Measurement of the Recoil Polarization in the $p(\vec{e}, e'\vec{p})\pi^0$ Reaction at the Delta(1232) Resonance", Phys. Rev. Lett. **86**, 2959, (2001).

[23] F. Kalleicher, *et al.*, "The determination of sigmaLT/sigmaTT in electro-pion-production in the Delta-resonance region", Z. Phys. **A359**, 201, (1997).

[24] H. Schmieden, "Double Polarization Experiments at Intermediate-Energy", Nucl. Phys. **A663**, 21, (2000).

[25] C. Mistretta, *et al.*, "Coincidence Measurements of Single-Pion Electroproduction near the Delta(1236) Resonance", Phy. Rev. **184**, 1487, (1969).

[26] S. Galster, *et al.*, "Coincidence Experiment on Inelastic Electron-Proton Scattering in the Region of the Delta(1236) at $q^2 = -0.35$ and -1.0 (GeV/c)^2", Phys. Rev. D **5**, 519, (1972).

[27] R. D. Hellings, *et al.*, "Coincidence π^0 electroproduction experiments in the first resonance region at momentum transfers of 0.3, 0.45, 0.60, 0.76 (GeV/c)^2", Nucl. Phys. **B35**, 93, (1971).

[28] W. Albrecht, *et al.*, "π^0 electroproduction at $\Delta(1232)$ and four-momentum transfer of 15 fm^{-2}", Nucl. Phys. **B25**, 1, (1970); W. Albrecht, *et al.*, "Electroproduction of $\Delta(1232)$ in the π^0 channel at four momentum transfer of 25 fm^{-2}", Nucl. Phys. **B27**, 615, (1971).

[29] J.C. Alder, *et al.*, "π^0 Electroproduction at the First Resonance at Momentum Transfer $Q^2 = 0.6$, 1.0 and 1.56 GeV^2", Nucl. Phys. **B46**, 573, (1972).

[30] K. Baetzner, *et al.*, "π^0 Electroproduction at the $\Delta(1232)$ Resonance at a Four-Momentum Transfer of $Q^2 = 0.3$ GeV^2", Nucl. Phys. **B76**, 1, (1974).

[31] A. Latham, *et al.*, Nucl. Phys. **B156**, 58, (1979).

[32] A. Latham, *et al.*, "Electroproduction of π^0 mesons in the resonance region at $Q^2 = 1$ (GeV/c)^2", Nucl. Phys. **B189**, 1, (1981).

[33] R. Siddle, *et al.*, " Coincidence π^0 Electroproduction Experiments in the First Resonance Region at Momentum Transfers of 0.3, 0.45, 0.60, 0.76 (GeV/c)^2", Nucl. Phys. **B35**, 93, (1971).

[34] F.E. Close and Z.P. Lee, "Photoproduction and Electroproduction of N* in a Quark Model with QCD", Phys. Rev. D **42**, 2194, (1990).

[35] Gavela, *et al.*, "Standard solution to Roper-resonance puzzles", Phys. Rev. D **21**, 182, (1980).

[36] S. Capstick and G. Karl, "E1+/M1+ and S1+/M1+ and their Q^2 dependence in gamma upsilon N → Delta with relativized quark-model wave functions", Phys. Rev. D **41**, 2767, (1990); S. Capstic, "Photo- and electroproduction of non-strange baryon resonances in the relativized quark model", Phys. Rev. D **46**, 2864, (1992).

[37] B. Boden and G. Krossen, Research Program at CEBAF, Proceedings of the Conference, Report of the 1986 Summer Study Group, edited by V. Burkert *et al.*, CEBAF, (1986).

[38] Ch. Gerhardt, "A Resonance Analysis of Electroproduction Data", Z. Phys. **C4**, 311, (1980).

[39] W. Konen, and H.J. Weber, "Electromagnetic $N \rightarrow N^*(1535)$ transition in the relativistic constituent-quark model", Phys. Rev. D **41**, 2201, (1990).

[40] B. Krusche, *et al.*, "Near Threshold Photoproduction of *eta* Mesons off the Proton", Phys. Rev. Lett. **74**, 3736, (1995).

[41] F.W. Brasse, *et al.*, "Separations of Sigma-L and Sigma-T in eta electroproduction at the resonance $S_{11}(1535)$", Nucl. Phys. **B139**, 37, (1978); F.W. Brasse, *et al.*, "Electroproduction of eta mesons in the region of the resonance $S_{11}(1535)$ at momentum transfers of 2 GeV^2 and 3 GeV^2", Z. Phys. **C22**, 33 (1984).

[42] U. Beck, *et al.*, "Electroproduction of eta-mesons at the $S_{11}(1535)$ Resonance", Phys. Lett. **B51**, 103, (1974).

[43] H. Breuker, *et al.*, "Determination of R = Sigma-L / Sigma-T from eta electroproduction at the $S_{11}(1535)$ Resonance", Phys. Lett. **B74**, 409, (1978).

[44] C.S. Armstrong, *et al.*, "Electroproduction of the $S_{11}(1535)$ resonance at high momentum transfer", Phys. Rev. D **60**, 052004, (1999).

[45] R. Thompson, *et al.*, "The $ep \rightarrow e'p\eta$ Reaction at and above the $S_{11}(1535)$ Baryon Resonance", Phys. Rev. Lett. **86**, 1702, (2001).

[46] E. Evangelides, *et al.*, "Electroproduction of π^+ mesons in the second and third resonance regions", Nucl. Phys. **B71**, 381, (1974).

[47] H. Breuker, *et al.*, "Forward π^+ electroproduction in the first resonance region at four momentum transfers $q^2 = -0.15$ and -0.3 GeV^2/c^2", Nucl. Phys. **B146**, 285, (1978).

[48] H. Breuker, *et al.*, "Electroproduction of π^+ Mesons at forward and backward directions in the region of $D_{13}(1520)$ and $F_{15}(1688)$ Resonances", Z. Phys. **C13**, 113, (1982).

[49] M.D. Mestayer et. al., "The CLAS Drift Chamber System", Nucl. Inst. and Meth. **A449**, 81, (2000).

[50] M. Amarian, et. al., "Characteristics of scintillators and light readout system of CLAS forward electromagnetic calorimeter", CLAS-NOTE 1999-009, JLAB.

[51] M. Amarian, *et al.*, "The CLAS Forward Electromagnetic Calorimeter", Nucl. Inst. and Meth. **A460**, 239, (2001).

[52] Yuri Sharabian, Private comminucations.

[53] K.S. Egiyan, "Determination of Electron Energy Cut Due to CLAS EC Threshold", CLAS-NOTE 1999-007, JLAB.

[54] E.S. Smith, *et al*, "The Time-Of-Flight System for CLAS", Nucl. Ints. and Meth. **A432**, 265, (1999).

[55] L. Elouadrhiri, V. Burkert, S. Stepanyan, H. Egiyan, "Charged Particle Identification in CLAS", CLAS-NOTE 1998-004, JLAB.

[56] E.S. Smith *et al.*, "Calibration of the CLAS TOF system", CLAS-NOTE 1999-011, JLAB.

[57] Simon Taylor, Ph.D. Thesis, Rice University, (2000) (unpublished).

[58] G. Adams, *et al.*, "The CLAS Cherenkov Detector", Nucl. Inst. and Meth. **A465**, 414, (2001).

[59] Stepan Stepanyan, “Simple Event Builder in the Framework of RECSIS”, JLab; Private communications.

[60] V. Blobel and CLAS software group, “The BOS system for CLAS software”, November 25 1995.

[61] J. J. Manak, E.S. Smith, S. McAleer, S. Barrow, “e1, g1, g6 Data Processing Procedures”, CLAS-NOTE 1999-016, JLAB.

[62] Alexander Vlassov, Private Communications.

[63] CLAS GEANT Simulation, http://improv.unh.edu/Maurik/gsim_info.shtml .

[64] G.S. Mutchler, S. Taylor, E. Smith “CLAS TOF scintillator positions”, CLAS-NOTE 1998-008, JLAB.

[65] R. Feuerbach, *et al.*, “Drift Chamber Alignment”, CLAS-NONE 98-002, JLAB.

[66] Will Brooks, Private Communications.

[67] A. Afanasev, I. Akushevich, V. Burkert, K. Joo, “QED radiative corrections in processes of exclusive pion electroproduction”, to be published.

[68] L.W. Mo, Y.S. Tsai, “Radiative corrections to Elastic and Inelastic ep and νp scattering”, Rev. Mod. Phys. **41**, 205, (1969).

[69] R. Minehart, C. Smith, AAO_RAD program; Private communications.

[70] P. E. Bosted, “Empirical fit to the nucleon electromagnetic form factors”, Phys. Rev. C **51**, 409, (1995).

[71] D. Drechsel, O. Hanstein, S.S. Kamalov, L. Tiator , “A unitary isobar model for pion photo- and electroproduction on the proton up to 1 GeV”, Nucl. Phys. **A645**, 145, (1999).

[72] T. Sato and T.-S.H. Lee, “Meson exchange model for πN scattering and $\gamma N \to \pi N$ reaction”, Phys. Rev. C **54**, 2660, (1996).

[73] M. Warns *et al.*, “A relativized quark model for radiative baryon transitions”, Z. Phys. **C45**, 613, (1990).

[74] M. Warns, *et al.*, ”Calculations of electromagnetic nucleon form factors and electroexcitation amplitudes of isobars”, Z. Phys. **C45**, 627, (1990).

[75] A. Silva, *et al.*, “E2/M1 and C2/M1 for the Electroproduction of the Delta(1232) in the Chiral Quark-Soliton model”, Prog. Part. Nucl. Phys. **44**, 211, (2000).

[76] Chr.V. Christov, *et al.*, “Baryons as non-topological chiral solitons”, Prog. Part. Nucl. Phys. **37**, 91, (1996).

[77] I.G. Aznauryan, “Relativistic effects, QCD mixing angles and $N \to N\gamma$ and $\Delta \to N\gamma$ transition form factors”, Z. Phys. **A346**, 297, (1993).

[78] I.G. Aznauryan, V. Burkert, S.G. Stepanyan, “JLab Analysis of Nucleon Resonances”; Private communications.

[79] I.G. Aznaurian, Private Communications.

[80] M. Aiello *et al.*, “Electromagnetic transition form factors of negative parity nucleon resonances”, J. Phys. **G24**, 753, (1998); M. Ferraris, M.M. Giannini, M. Pizzo, E. Santopinto and L. Tiator, “A Three Body Force Model for the Baryon Spectrum”, Phys. Lett. **B364**, 231, (1995).

[81] E. Santopinto *et al.*, “Nucleon form factors in a simple three-body quark model”, Eur. Phys. J. **A1**, 307, (1998); E. Santopinto, F. Iachello and M.M. Giannini, “Exactly solvable models of baryons spectroscopy”, Nucl. Phys. **A623**, 100c, (1997).

[82] R. A. Arndt, I.I. Strakovski and R.L. Workman, “Updated Resonance Photodecay Amplitudes To 2-GeV”, Phys. Rev. C **53**, 430, (1996).

[83] Particle Data Group, “Review of Particle Physics”, Eur. Phys. J. **C15**, 1, (2000).

[84] F. James , “MINUIT : Function Minimization and Error Analysis”, CERN Program Library, entry D506, (1994).

VITA

Hovanes Egiyan

Hovanes Egiyan was born in Yerevan, Armenia on 17 January 1972, was graduated from #122 High School in Yerevan in June 1988, and received a Bachelor of Science degree in physics from Yerevan State University in 1993. He studied at the graduate school of the Yerevan Physics Institute, then entered the physics graduate program at the College of William and Mary in 1995 and received a Master of Science degree in May 1997. This dissertation was defended on 10 September 2001 at the College of William and Mary in Virginia.